

Phase Transformations in 18-Carat Gold Alloys Studied by Mechanical Spectroscopy

THÈSE N° 4635 (2010)

PRÉSENTÉE LE 12 MARS 2010

À LA FACULTÉ SCIENCES DE BASE
INSTITUT DE PHYSIQUE DE LA MATIÈRE CONDENSÉE
PROGRAMME DOCTORAL EN PHYSIQUE

ÉCOLE POLYTECHNIQUE FÉDÉRALE DE LAUSANNE

POUR L'OBTENTION DU GRADE DE DOCTEUR ÈS SCIENCES

PAR

John HENNIG

acceptée sur proposition du jury:

Prof. O. Schneider, président du jury
Prof. R. Schaller, Dr D. Mari, directeurs de thèse
Prof. G. Fantozzi, rapporteur
Dr A. Munier, rapporteur
Prof. M. Rappaz, rapporteur



ÉCOLE POLYTECHNIQUE
FÉDÉRALE DE LAUSANNE

Suisse
2010

Abstract

This work is motivated by an industrial interest in gaining a better understanding of the phase transformations that govern the mechanical properties of 18-carat gold alloys commonly used in jewelry applications and luxury watchmaking. These alloys fall in one of two categories: yellow gold based on the gold-copper-silver system and white gold based on gold-copper-palladium, but may contain further alloying elements that improve color, castability, strength, and wear resistance.

In this thesis, selected alloys from the two series are studied, primarily by mechanical spectroscopy. The analysis and interpretation of the experimental data identifies three important anelastic relaxations (internal dissipation processes), which dominate the mechanical loss spectrum of each of these materials above room temperature.

A Zener relaxation, due to directional ordering of atoms in the substitutional solid solution, occurs at intermediate temperatures, between 550 K and 700 K depending on the alloy. Near an order-disorder transition, the Zener relaxation increases markedly in strength when approaching the transition temperature from above, and breaks down when the materials forms the long-range ordered phase below it. In a preliminary study on a Au-Cu alloy (close to the equiatomic composition), this behavior is, for the first time, directly documented by measurements of the mechanical loss in isothermal conditions. It is demonstrated that this experimental method provides a precise value of the transition temperature as well as useful data of the transformation kinetics. The Zener relaxation in yellow gold alloys (of sufficiently high copper content) exhibits the same characteristics. These materials harden because they form an ordered phase of tetragonal symmetry like AuCu. Compared to Au-Cu, the addition of silver reduces the transition temperature. Furthermore, it is concluded that no atomic ordering occurs in the white gold alloys.

Above 700 K, the mechanical loss spectrum of 18-carat gold features an anelastic relaxation peak that is shown to be caused by the sliding of grain boundaries. The analysis of this part of the spectrum exposes the age-hardening mechanism acting in some of the white gold alloys. Their composition is such that they form a second phase that precipitates as fine particles. Particles segregating on grain boundaries block the sliding and the grain boundary relaxation peak subsides, leaving only the high-temperature background. The background is created by vibration of bulk dislocations. Precipitates forming inside the grains pin these dislocations, which explains the increased resistance to plastic deformation in the age-hardened state.

Keywords: 18-carat, gold, mechanical spectroscopy, anelasticity, internal friction, Zener relaxation, stress-induced ordering, directional ordering, atomic ordering, order-disorder, grain boundary sliding, precipitation hardening

Résumé

Ce travail est motivé par un intérêt industriel de mieux comprendre les transformations de phase qui regissent les propriétés mécaniques des alliages d'or 18 carats couramment utilisé en joaillerie et horlogerie de luxe. Ces alliages se divisent en deux catégories : l'or jaune basé sur le système or-cuivre-argent et l'or gris basé sur or-cuivre-palladium, mais peuvent contenir des éléments d'alliage supplémentaires permettant d'améliorer la couleur, de faciliter la coulée ou encore d'augmenter la résistance à l'usure.

Dans cette thèse, des alliages de ces deux séries sont étudiés, principalement par spectroscopie mécanique. Grâce à l'analyse et l'interprétation des données expérimentales, trois phénomènes de relaxation anélastique (processus de dissipation interne), qui dominent les spectres de pertes mécaniques au-dessus de la température ambiante, sont identifiés comme importants pour les propriétés mécaniques de ces matériaux.

Un pic de relaxation de Zener, dû à la mise en ordre directionnel d'atomes dans la solution solide, apparaît à température intermédiaire, entre 550 K et 700 K en fonction de l'alliage. Au-dessus de la température critique d'une transition ordre-désordre, l'intensité de la relaxation de Zener augmente de manière accrue. Par contre, la relaxation disparaît quand la phase ordonnée se forme. Dans une étude préliminaire d'un alliage Au-Cu (proche de la composition équiatomique), ce comportement est observé, pour la première fois, de manière directe grâce à des mesures des pertes mécaniques en conditions isothermes. Il est montré que cette méthode expérimentale fournit une valeur précise de la température de transition ainsi que des informations sur la cinétique de la transformation. La relaxation de Zener dans l'or jaune (à condition que l'alliage en question contienne suffisamment de cuivre) montre les mêmes caractéristiques. Ces matériaux durcissent parce qu'ils forment une phase ordonnée de symétrie tétragonale tel que AuCu. Par rapport à Au-Cu, l'addition d'argent réduit la température de transition. En outre, on conclut qu'il n'y a pas de mise en ordre atomique dans les alliages d'or gris.

Au-dessus de 700 K, le spectre de pertes mécaniques d'or 18 carats présente un pic de relaxation interprété par le glissement aux joints de grains. L'analyse de cette partie du spectre révèle le mécanisme de durcissement qui agit dans certains alliages d'or gris. Leur composition est telle qu'ils forment une phase secondaire qui précipite en particules fines. Les particules qui naissent aux joints de grains bloquent le glissement de ceux-ci, ce qui fait que le pic de relaxation décroît, ne laissant que le fond haute température. Ce fond est créé par la vibration de dislocations. Des précipités qui se développent à l'intérieur des grains ancrent ces dislocations, ce qui explique la résistance élevée à la déformation plastique dans l'état durci.

Mots-clés : 18 carats, or, spectroscopie mécanique, anélasticité, frottement intérieur, relaxation de Zener, ordre directionnel, ordre atomique, ordre-désordre, joints de grains, précipitation

Zusammenfassung

Die vorliegende Arbeit bezieht ihre Motivation aus dem industrieseitigen Interesse an einem besseren Verständnis der Phasentransformationen, die maßgeblich die mechanischen Eigenschaften jener 18-Karat-Goldlegierungen bestimmen, welche üblicherweise im Schmuckgewerbe und der Luxusuhrmacherei Verwendung finden. Die Legierungen unterteilen sich in zwei Kategorien: Gelbgold, das auf Gold-Kupfer-Silber aufbaut, sowie Weißgold, das auf Gold-Kupfer-Palladium basiert, können aber weitere Legierungselemente enthalten, die dem Zweck dienen, Farbe, Gießbarkeit, Festigkeit und Abnutzungsresistenz zu verbessern.

In dieser Dissertation werden ausgewählte Legierungen beider Serien untersucht, in erster Linie per mechanischer Spektroskopie. Durch Analyse und Interpretation der experimentellen Daten werden drei wichtige anelastische Relaxationsarten (interne Dissipationsprozesse) unterschieden, die in all diesen Materialien das mechanische Spektrum, ab Zimmertemperatur aufwärts, dominieren.

Eine Zener-Relaxation, verursacht durch directionale Ordnung von Atomen innerhalb der substitutionellen festen Lösung, tritt bei mittleren Temperaturen auf, zwischen 550 K and 700 K je nach Legierung. In unmittelbarer Umgebung eines Ordnungs-Unordnungs-Übergangs nimmt die Relaxation rasch an Intensität zu, solange man sich der kritischen Temperatur von oben her nähert. Unterhalb jedoch, wenn sich die atomare Ordnung einstellt, bricht die Relaxation ein. In einer vorbereitenden Studie an einer Au-Cu-Legierung (unweit der äquiatomaren Zusammensetzung) wird dieses Verhalten zum ersten Mal durch direkte Beobachtung dokumentiert, dank Messungen der mechanischen Verluste unter isothermen Bedingungen. Es wird gezeigt, dass diese experimentelle Methode dazu dienen kann, präzise die Übergangstemperatur zu bestimmen, und darüberhinaus Informationen über die Kinetik der Phasentransformation liefert. Die Zener-Relaxation in Gelbgold weist die gleichen Charakteristika auf, vorausgesetzt der Kupferanteil ist ausreichend hoch. Diese Materialien härten deshalb, weil sie eine geordnete Phase mit einer Übergitterstruktur tetragonaler Symmetrie wie in AuCu ausbilden. Im Vergleich zu Au-Cu senkt der Silberanteil die Übergangstemperatur.

Oberhalb von 700 K weist das mechanische Spektrum von 18-karätigem Gold einen Relaxationspeak auf, der vom Gleiten entlang der Korngrenzen herrührt. Die Analyse dieses Teils des Spektrums deckt den Härtungsmechanismus auf, der in einigen der Weißgoldlegierungen zum Tragen kommt. Ihre Zusammensetzung muss dafür derart beschaffen sein, dass sich eine zweite Phase bildet und sich in Form feiner Partikel abscheidet. Ausscheidungen, die an Korngrenzen anlagern, blockieren den Gleitprozess und die Relaxation kommt zum Stillstand. Nur der Hintergrund bleibt zurück, der durch die Vibration von Versetzungen verursacht wird. Ausscheidungen, die sich innerhalb der Körner absetzen, behindern die Bewegung der Versetzungen, was den erhöhten Widerstand gegenüber plastischer Verformung im gehärteten Zustand erklärt.

Contents

Introduction	1
1 Materials	5
1.1 Color	5
1.2 Yellow Gold	7
1.3 Order-hardening in AuCu	12
1.4 White Gold	15
1.5 Outlook	19
2 Experiments	21
2.1 Mechanical spectroscopy	21
2.2 Forced torsion pendulum	26
2.3 Hardness tests	31
2.4 X-ray diffraction	31
2.5 Growth of single crystals	32
3 Anelastic Relaxations in 18-carat Gold	35
3.1 Yellow Gold	35
3.2 White Gold	40
4 Zener Relaxation near Order-Disorder Transitions	49
4.1 Theory of the Zener relaxation	49
4.2 Zener peak in Au–Cu	58
4.3 Kinetics of atomic ordering	61
4.4 Order hardening in yellow gold	64
4.5 Zener peak in white gold	71
5 Grain Boundary Sliding blocked by Precipitates	75
5.1 Grain boundary sliding in metals	76
5.2 Grain boundary peak in 18-carat gold	83
5.3 Precipitates blocking grain boundary sliding	92
5.4 Precipitation hardening in white gold	99
Conclusions	105
Bibliography	107

Introduction

Since the dawn of human civilization, gold has been one of the most appealing and sought-after elements of the periodic system. With its high corrosion resistance — the defining quality of *noble* metals — it suggested itself as the base material or protective coating of works and ornaments created to stand the test of time. Its distinctive color stands out against the grayish monotony displayed by most metals (the only other exceptions being copper and caesium). These properties combined with its rarity qualifies gold as a *precious* metal — a perception that, to the casual observer, is further reinforced by its high specific weight. Historically, gold has therefore become a standard for monetary exchange and reserve assets in many parts of the world.

In the industrial age, gold found many a new application: in electronics for its good conductivity and chemical passivity; in optics for its excellent reflectivity of infrared light; and, more recently, in organic chemistry for the catalytic properties of gold nanoparticles. However, to this day the lion share of gold has been and is being used for jewelry production. It accounted for 58% (2137.5 tonnes) of global gold demands in 2008, and even 68% during the two preceding years. The jewelry demand is roughly matched by the annual output of today's gold mines worldwide.^[GD08]

Pure gold, with a Vickers hardness of only 20 to 30 HV^[Co01] (depending on purity), is too soft for almost all jewelry purposes as the final product would easily deform and show poor resistance to wear. It must thus be alloyed to achieve reasonable hardness values, ideally 300 HV or more in the finished product. To reassure customers, these gold alloys are hallmarked with their fineness (mass of gold per thousand) or caratage (24 carat equaling 100 weight-percent). In many countries legislation restricts tradable gold alloys to certain compositions. Most high-quality jewelry is therefore made of 18-carat gold, an international standard caratage combining high value with good resistance to tarnish, corrosion, and wear.^[Dr92]

18-carat gold alloys exhibit a variety of colors, from the pale yellow gold–silver to the rose-colored gold–copper or even the purple gold–aluminum.^[Cr99, Ca98] In jewelry and watch-making the most widely used alloys fall in either of two (simplified) categories: the group termed *yellow gold* (also, and more aptly, named: colored gold) refers to any gold–copper–silver alloy, while *white gold* comprises

alloys that have been bleached in order to display a regular metallic, grayish color like platinum or even steel.

Yellow gold alloys have a long tradition in jewelry and watch-making. Most “golden” rings or watches are made from the 18-carat alloy containing 12.5 weight-% of each copper and silver, which imitates the color of pure gold. The phase diagram of Au–Cu–Ag has been studied for almost 100 years.^[Pro6] It is a ternary alloy system of particular interest as it inherits the immiscibility gap from the binary silver–copper alloys as well as the tendency to form ordered phases from gold–copper. Both mechanisms, phase separation (into a silver-rich and a copper-rich phase) and atomic ordering (within the copper-rich phase), may lend the alloy a much desired property: age-hardenability.^[Ra90] An age-hardenable material offers the advantage that the jeweler can work or machine the product in a soft and ductile state (the annealed and quenched solid solution), and eventually finish the product by means of a simple heat treatment rendering the material hard and resistant. However, even in the finished product the material must meet certain requirements as to its ductility. If it is too brittle, certain elements, like clockwork springs or watchstrap pins, may not withstand the stresses they are subject to in everyday situations, and break or crack. It is therefore important to control the phase transformation process for any given alloy, which requires knowledge of transition temperature and transition times.

White gold, when developed in the 1920’s, was initially designed to offer a cheaper alternative to platinum for high-quality jewelry.^[No92] Traditionally, two elements, nickel and palladium, have been used almost exclusively to bleach out the characteristic color that gold confers its alloys — though alternative bleachers have been tested and reviewed.^[OC78] Since the 1980’s nickel-containing alloys have largely fallen into disuse — and legislation banning them from jewelry production was introduced in many countries — as more and more costumers became sensitized to nickel and experienced highly discomforting allergic skin reactions upon contact.^[Ru00,Ro99] With palladium trading at prices comparable to gold (fluctuating between as low as 20% to up to 300% of the gold price over the past ten years), Pd-based white gold alloys may nearly miss their declared design goal, but do, however, enjoy great popularity since the end of the 1990’s.^[Ro99] After this shift of demand and surge of the market, further research into the mechanical property of modern white gold seems warranted.

The goal of this thesis is to contribute to a fundamental understanding of modern 18-carat gold alloys by studying the dynamic processes at the microstructural level. The method of choice for this endeavor is mechanical spectroscopy, an experimental technique that probes the mechanical response of a specimen (deformation/strain) to a periodic external excitation (applied stress). Being sensitive to point defect relaxations, grain boundary sliding and dislocation motion, it can yield data on atomic diffusion as well as the mobility of the two mediators of plastic deformation, grain boundaries and dislocations. While the primary objective is to present a comprehensive interpretation of the mechanical spectra, further emphasis will be placed on implications with regard to the mechanical

properties of the alloys, namely the detection of phase transformations (phase separation, atomic ordering, precipitation of second phase particles) that may be exploited to optimize material properties such as hardness and ductility. The yellow golds, as the better known alloy system, will serve as a starting point of this study and as a yardstick for the metallurgy of the white gold alloys.

Research for this thesis was part of a project funded by the Swiss Confederation's Innovation Promotion Agency (CTI/KTI)¹ that promotes knowledge and technology transfer between companies and universities. Our partner is Varinor, a Swiss-based manufacturer that refines and processes gold alloys for the luxury watch and jewelry industry. All 18-carat gold samples studied throughout this work were provided by Varinor and can be considered a fairly representative selection of 18-carat yellow and white gold alloys currently available on the market.

¹Under grant number 7696.3 EPRP-IW.

Chapter 1

Materials

Carat gold has a long-standing tradition, dating back several centuries, as a bulk material for jewelry^[Dr92] and in watchmaking^[Tr04]. As such, it must meet metallurgical demands imposed by the manufacturing process. Finely crafted pieces, common in both domains, require a sufficiently ductile material, not too soft but not too hard either, that can be precisely cut without bending at the edges or fraying out. The finished products, on the other hand, should be as hard as possible so as to offer maximum resistance to wear and surface scratching. Polishing, whenever needed, should produce smooth and shiny metallic surfaces that must not be marred by inclusions or micro-cracks.

Two rather different series of 18-carat¹ gold alloys are the focus of this study: yellow golds and white golds. As the names suggest, their distinguishing mark is the color. Mechanical properties and color are both influenced to a great extent by the alloying elements used besides gold. However, small variations in composition may alter the mechanical properties drastically while the color changes unnoticeably, or at least acceptably. One can therefore try to optimize the mechanical properties while keeping the color intact.

1.1 Color

The color of a gold alloy — or any material for that matter — is the result of its reflectivity as a function of the frequency of incident light, which in turn results directly from its electronic band structure. Photons are absorbed as electrons undergo interband transitions to (unpopulated) or from (populated) states near the Fermi level. For most metals, such transitions require energies in excess of 3 eV so that visible light cannot be absorbed and must be reflected.

In the periodic table, copper, silver and gold can be found in periods 4, 5 and 6, respectively, all in the same group, 11. Obviously, their electronic structures are very similar. Simply put, they have (five) fully occupied, rather flat d-bands below

¹24 carats equal 100 weight percent. In North America, the spelling “karat” has become the norm, in an effort to distinguish it from the homonymic weight unit (equaling 200 mg) for gemstones. Common acronyms are ct, kt, or even just k.

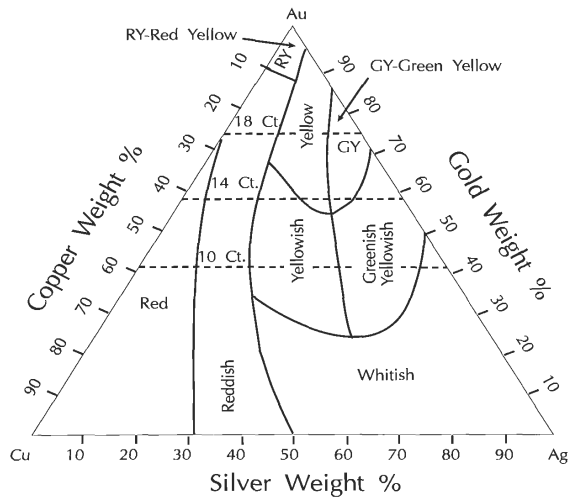


Figure 1.1: Colors exhibited by Au–Cu–Ag (after ref. [Le49](#), reproduced from [Ra90](#)).



Figure 1.2: An 18-carat white gold alloy containing 12.5 weight-% palladium (Au 5125, top) and an 18-carat yellow gold containing 12.5% silver (Au 318, bottom).

a half-filled s-band, the conduction band. Higher bands are far up in energy so that the position of the highest d-band with respect to the Fermi level, which intersects only the s-band, effectively determines the absorption threshold in the spectrum of light.^[AM15] This threshold is lowest in copper (2.0 eV), followed by gold (2.3 eV), then silver (4.0 eV), making copper red (absorbing green to blue), gold yellow (absorbing blue) and silver white (reflecting all).^[Sa77,AM15]

In general, studying the band structure of alloys is a difficult endeavor. Strictly speaking, translational symmetry is lost in a disordered alloy and consequently the Bloch theorem no longer applies. In other words, the Bloch wave vector \vec{k} is not a good quantum number and merely denotes a state of finite lifetime. However, while the eigenstates will depend on the actual atomic configuration, all macroscopic physical observables should remain in the immediate vicinity of the ensemble average. Therefore, a common approach to tackle the problem of non-periodicity is to find an effective medium that yields the same expectation values as the random alloy. This is known as the Coherent Potential Approximation^[So67]. Eigenstates can again be classified in terms of \vec{k} , but new quasi-particles (collective excitations) may emerge.

However, if the band structures of the constituents are as similar as they are in the case of gold, silver and copper^[La87], a good, yet simple approach is the Virtual Crystal Approximation: the new (virtual) eigenstates are superpositions of the corresponding eigenstates in the pure metals, weighted with their respective atomic concentrations. Namely, alloying gold with silver will shift the d-bands down in energy, while copper shifts them up. Just like a painter mixing paints of different colors on a palette, one can thus obtain any shade between the yellow of gold, the red of copper and the white of silver by choosing the appropriate (atomic) percentages of the three constituents. This is illustrated on the ternary diagram² in figure 1.1.

²In a ternary diagram, the content of a given component goes from 100% in the labeled corner to zero all along its opposite edge, with isolevel lines parallel to the edge.

alloy	mass fraction (%)			atom fraction (%)		
	Au	Cu	Ag	Au	Cu	Ag
Au 118	75.0	4.0	21.0	59.6	9.9	30.5
Au 218	75.0	9.0	16.0	56.8	21.1	22.1
Au 318	75.0	12.5	12.5	54.9	28.4	16.7
Au 3418	75.0	15.0	10.0	53.7	33.3	13.1
Au 418	75.0	16.0	9.0	53.2	35.2	11.7
Au 518	75.0	20.5	4.5	51.1	43.3	5.6
Au 5618	75.0	21.5	3.5	50.7	45.0	4.3

Table 1.1: Nominal composition of the yellow gold alloys studied in this work.

Alloying gold with metals from group 10 of the periodic system, the platinum group, such as nickel, palladium and platinum itself, has a whole different effect on the color. These transition metals are one electron short of a complete d-shell. In the pure metals, not only the s-band but also the d-bands extend beyond the Fermi energy.^[AM15] The mixing of the impurities' d-levels with the gold matrix's s-band produces new quasi-particles of finite lifetime: virtually bound states.^[Fr58,Ca63] They correspond to conduction electrons being trapped by an impurity atom's (screened) d-level and scattered back into the conduction band, which all in all lowers their energies, but not enough to bind them permanently. The virtually bound states are at 0.8 eV (infra-red) for Au-Ni^[Sa77] and 1.6 eV (red) for Au-Pd^[Na98] below the Fermi level. Thus, these resonances absorb light that is otherwise reflected by gold, i.e. they whiten gold by flattening the reflectivity's frequency profile. Compared to silver, this bleaching mechanism is far more efficient: at 12.5 weight-% palladium an 18-carat gold alloy is white, see figure 1.2.

1.2 Yellow Gold

18-carat yellow gold alloys are essentially — and within the scope of this work: exclusively — gold-copper-silver alloys with a 75% mass content of gold. In atomic percentages, this corresponds to a gold content ranging from as low as 50% on the copper-rich end to up to 60% on the silver-rich end. Table 1.1 lists the exact compositions of seven alloys on which measurements were performed.

Yellow golds (of any caratage) are often referred to as colored gold alloys since they do, in fact, exhibit various hues and shades other than the one universally associated with gold (cf. figure 1.1). The 18-carat alloys vary from pale yellow (some say: greenish^[Cr99]) on the silver-rich side to rose-colored on the copper-rich side. A color standard has been developed with the German DIN 8238, an extension of an earlier Swiss watch industry standard, that defines color codes 1N through 5N by fixing the Au-Cu-Ag composition.^[Ro78] These are reflected in alloy designations such as “Au 318” in table 1.1, meaning an 18-carat gold alloy

of color 3N. (The designation “3N18” is common as well.) The alloy (named here) Au 3418 has an off-standard composition somewhere between 318 and 418.

In the previous section, the color palette offered by Au–Cu–Ag was attributed to a continuous variation of the band structure upon mixing the three very similar elements. The electronic structure determines yet another aspect of practical importance: the equilibrium phases. Whether an alloy tends to develop superstructures of atomic order, separate in phases of different chemical composition, or retains a random configuration even in the medium and low temperature range, depends largely on its electronic ground state and the stability thereof. Here, however, the similarities end. As the experimental binary phase diagrams in figures 1.3 through 1.5 suggest, all three of these tendencies play a role in the ternary Au–Cu–Ag system.

In fact, silver is perfectly soluble in gold.^[AgAu] No long-range order has been observed in the bulk material.^[Ok83] The ground state should nevertheless be ordered.^[Oz98] This is a consequence of the third law of thermodynamics which requires that the entropy vanish when approaching absolute zero.^[Ab04] However, when the transition temperature is too low, as is the case here, the ground state is kinetically inhibited. The mixing enthalpy per atom is -48 meV for the disordered solid solution at equiatomic composition.^[Oz98]

Copper and silver, on the other hand, have a positive mixing enthalpy, about 104 meV per atom according to theoretical calculations.^[Oz98] That means, these two atom species cannot lower their internal energy in the presence of each other. As illustrated by the phase diagram in figure 1.4, only at very high temperatures, close to the solidus line, does the thermal entropy outweigh the mixing enthalpy enough to dissolve one component in the other to some extent. Other than that, the immiscibility gap spans virtually the entire composition range. Hence, copper and silver repel each other in the solid solution and have a strong tendency to form separate phases.

With -91 meV^[Oz98] the mixing enthalpy of AuCu³ is even lower (greater in absolute value) than that of AuAg, indicating an even stronger drive to form ordered structures. Indeed, as the phase diagram in figure 1.5 shows, order-disorder transitions occur over a wide composition range between 500 K and 700 K, i.e. at temperatures where atomic diffusion remains fast enough to not hinder the formation of long-range order.

Figure 1.6 illustrates the atomic configurations of the most prominent phases appearing on the diagram. At all compositions the high-temperature phase (α phase) is a solid solution where gold and copper atoms are distributed nearly⁴ randomly over the sites of a face-centered cubic lattice (superstructure type: A1). At 75 atomic-% gold or copper, the solid solution may transform into an ordered structure that has the majority atoms sitting on the faces, the minority

³Throughout this work, designations such as Au–Cu (with a dash) will denote alloys of arbitrary composition, while AuCu (just like a chemical formula) refers to the equiatomic alloy.

⁴Short-range order, i.e. non-perfect randomness of like or unlike neighbors, may be present in the solid solution.

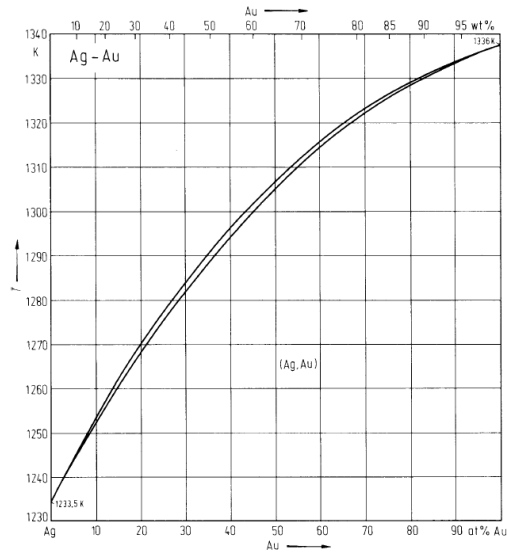


Figure 1.3: Binary phase diagrams of Ag-Au, from reference [AgAu](#).

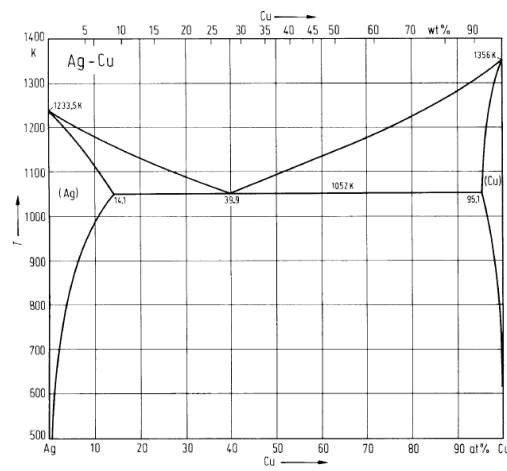


Figure 1.4: Binary phase diagrams of Ag-Cu, from reference [AgCu](#).

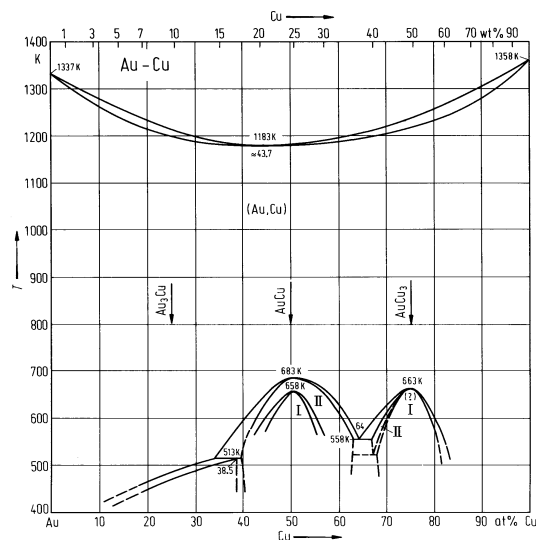


Figure 1.5: Binary phase diagrams of Au-Cu, from reference [AuCu](#).

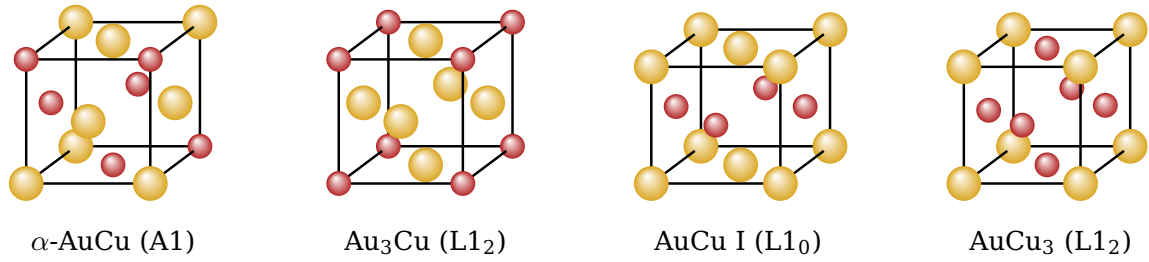


Figure 1.6: Unit cells of the disordered solid solution α -AuCu and three ordered structures of stoichiometric Au-Cu alloys. The superstructure symmetry is noted in parentheses.

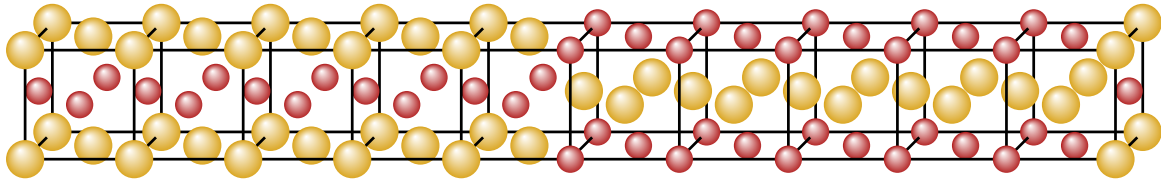


Figure 1.7: Unit cell of the equiatomic AuCu II superstructure.

atoms at the corners of the unit cube (L₁₂ type). In the so-called AuCu I phase of equiatomic composition, gold and copper atoms occupy alternating {001} planes (L₁₀ type). It differs from the previous phases in that it breaks the cubic symmetry and forms a tetragonal unit cell with an axis ratio of $c/a = 0.92$.^[Hi62]

Over the narrow temperature interval between 658 K and 683 K, above the ground state AuCu I and below the high-temperature solid solution α -AuCu, the phase AuCu II is stable. AuCu II is similar to AuCu I as its building blocks are L₁₀ cells, but with periodic anti-phase boundaries in either the [100] or [010] direction. An anti-phase boundary delimits subdomains of same unit cell orientation but with the sequence of Au and Cu planes out of step. The number of unit cells between two successive anti-phase boundaries is generally denoted M . For the AuCu II structure depicted in figure 1.7, $M = 5$ and the length of the orthogonal unit cell is almost exactly $b = 10a$.^[Fe99] In effect, AuCu II is an incommensurate structure and M fluctuates statistically around some average value.^[Fe99] In other words, the regularly spaced anti-phase boundaries are not perfectly plane but have random bumps and dents. The inherent disorder in this otherwise ordered structure explains its intermediate thermodynamic position between the fully ordered AuCu I and the disordered α -AuCu.^[Bo99]

To the left and right of the stoichiometric compositions Au₃Cu, AuCu and AuCu₃, the low-temperature ordered phase, while retaining its basic symmetry, will have to incorporate a certain amount of substitutional disorder, i.e. some copper atoms will populate the gold sublattice or vice versa. As for AuCu II, the anti-phase periodicity M was found to vary continuously from 5 at the equiatomic composition to up to 6.5.^[Fe99]

The phase formation trends of the binary alloys persist in the ternary system. Figure 1.8 shows sections at 350 °C and 300 °C of the experimental Au-Cu-Ag phase diagram.^[Pr06] Au-Cu-Ag clearly inherits the immiscibility gap from Cu-Ag.

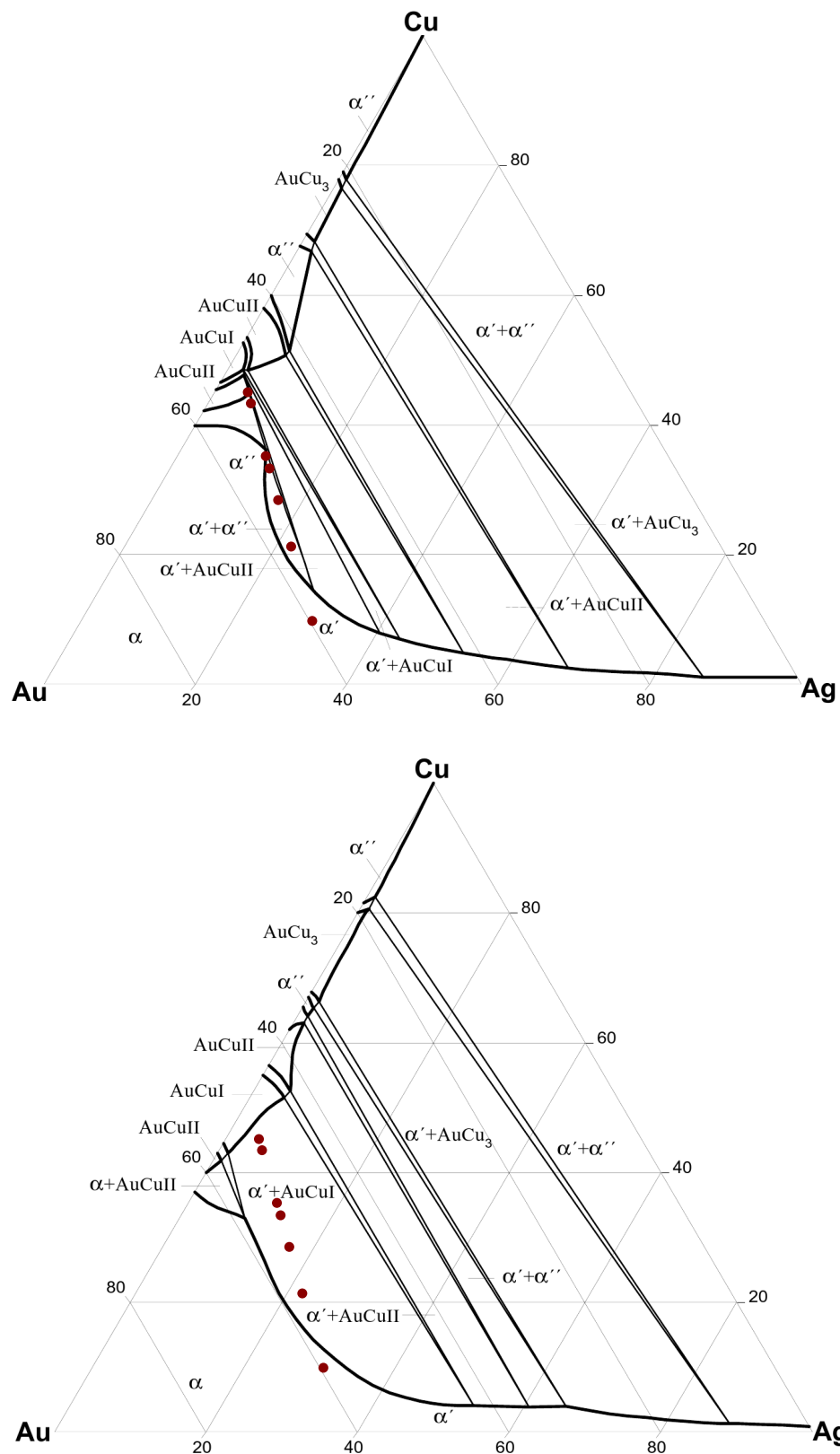


Figure 1.8: Sections of the ternary phase diagram of Au–Cu–Ag at 350 °C (top) and 300 °C (bottom); reproduced from reference [Pr06](#) with markers added to indicate the 18-carat yellow gold alloys listed in table 1.1.

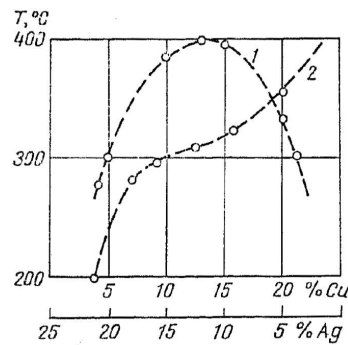


Figure 1.9: Transition temperatures of phase separation (1) and atomic ordering (2) for 18-carat yellow gold alloys (reproduced from reference Ra77).

While on the Au–Ag side of the diagram the silver-rich solid solution (α' phase) shows no sign of ordering, the copper-rich solid solution (α''), though it contains silver to some extent, forms the same superstructures as Au–Cu.

The 18-carat yellow gold alloys are situated near the tip of the immiscibility curve. At 300 °C, only one alloy, Au 118, is outside the zone of phase separation. As the 350 °C section suggests, phase separation and atomic ordering occur within the same temperature range, between 300 °C and 400 °C. Indeed, a separate study dedicated exclusively to 18-carat yellow gold^[Ra77] found that in red gold ordering precedes phase separation (i.e. occurs at higher temperature), while in the other alloys the order is reversed. These findings are reproduced in figure 1.9.

It is worth pointing out that, for a given alloy, the predictions of a phase diagram such as the ternary sections shown in figure 1.8 are of limited reliability. Typically, only a few alloys are prepared, heat-treated, quenched and studied by X-ray and electron diffraction. Phase boundaries are then interpolated. Furthermore, it is difficult to detect the onset of phase separation. It manifests itself as the splitting of a diffraction spot, so it may be obscured by peak broadening. For instance, with regard to alloy Au 418 (16 weight-% copper), another study^[Na88] concluded that phase separation and atomic ordering occur at the exact same temperature, contradicting the result in figure 1.9.

1.3 Order-hardening in AuCu

18-carat yellow gold alloys are age-hardenable, i.e. their hardness increases over the course of a heat treatment at a well-chosen temperature. The more copper the alloy contains, the more pronounced is the hardening effect. Table 1.2 compares the Vickers hardness of solution-treated samples (annealed at high temperature in order to put all elements into solution) to those age-hardened at about 550 K. Hardness values after mechanical hardening by cold deformation are listed for comparison.

alloy	solution-treated	work-hardened	age-hardened
Au 218	135 HV	210 HV	170 HV
Au 318	150 HV	225 HV	230 HV
Au 418	160 HV	240 HV	285 HV
Au 518	165 HV	240 HV	325 HV

Table 1.2: Vickers hardness of Au 218^[AD²¹⁸], Au 318^[AD³¹⁸], Au 418^[AD⁴¹⁸] and Au 518^[AD⁵¹⁸] after three thermo-mechanical treatments: solution-treating (annealing at 550 °C for 30 min, then quenching), work-hardening (cold deformation to 75%) and age-hardening/order-hardening (heat treatment at about 280 °C for 60 min).

It is fair to assume that the hardening of 18-carat yellow gold is brought on by the process of atomic ordering. For two reasons: first, the presence of copper is a prerequisite; and second, order-hardening is known to occur in AuCu.^[Ar₆₇] Moreover, it has been reported that the $\alpha \rightarrow \alpha' + \alpha''$ phase decomposition does not strengthen 18-carat yellow gold.^[Ra₇₇]

During a transformation of α -AuCu into AuCu I, the cubic unit cell expands by 2.3% along the a- and b-axis, while it shrinks by 5.3% along c.^[Ar₆₇] The substantial change of shape produces large misfit strains that have to be accommodated over the course of the ordering process.

X-ray diffraction^[OB₅₉] and transmission electron microscopy^[Hi₆₂, Sy₆₇] have revealed that the process of atomic ordering goes through the following stages: First, coherent plate-like AuCu I nuclei form on $\{110\}_{\text{cub.}}$ planes of the disordered matrix. When the coherency strains become large enough, so-called micro-twinning will occur on $\{101\}_{\text{tet.}}$ planes before growth continues perpendicular to that plane. The result is a needle-shaped line-up of incoherent ordered domains with c-axes alternating between two (out of three possible) orientations, as illustrated in figure 1.10. The size of a single ordered domain is of the order of 1 micron by 1 micron by one tenth of a micron. The domains may contain anti-phase boundaries such as those in the AuCu II structure, but non-periodic. As the needle-shaped twin lamellae grow along a $\langle 101 \rangle_{\text{tet.}}$ direction, misfit strains of longer range are accommodated by other needles that originated from nuclei of different orientation.

Other X-ray studies^[Bo₂₈, Ma₆₉] contend that at lower temperatures (less than 150 °C), instead of the nucleation and growth process described above, ordering takes place homogeneously. It would thus proceed uniformly throughout the crystal, forming ordered domains of random c-axis orientation that gradually lose coherence with their surroundings.

It may be worth of note that the kinetics of the ordering process depends on the temperature of the previous disordering.^[Ku₅₅] This suggests that the presence of short-range order plays an important role for the transformation time of atomic ordering. Interestingly, it was found that the higher the disordering temperature (i.e. the less pre-existing short-range order there is), the faster the ordering process. This can be understood as follows: Atomic ordering involves diffusion

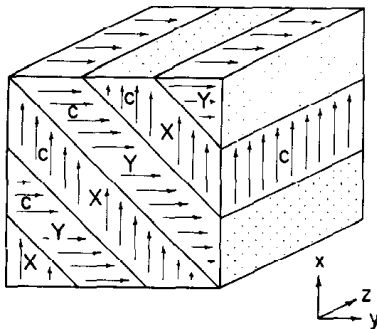


Figure 1.10: Section of a needle-shaped array of twin lamellae in AuCu, formed by a sequence of ordered domains of alternating c-axis orientation (reproduced from reference [Hi62](#)).

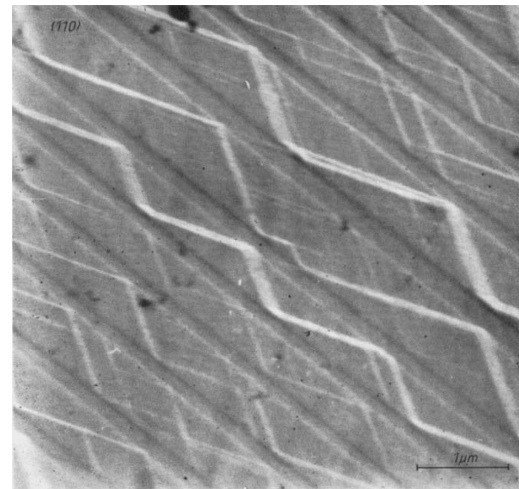


Figure 1.11: Slip bands in AuCu (produced by a 5% plastic deformation), confined exclusively to AuCu I ordered domains, as revealed by scanning electron microscopy after electro-polishing and etching of the surface (reproduced from reference [Sy67](#)).

of gold and copper atoms to distinct $\{001\}$ planes. If the degree of short-range order is high, many atoms will be embedded in a low-energy configuration of nearest neighbors. Instead of moving single atoms in a random matrix, more energy is now required to break up the group of atoms or even move them all together.

At ordering temperatures below about $200\text{ }^{\circ}\text{C}$, the hardness of AuCu increases continuously with ordering time, i.e. with the degree of long-range order. At annealing temperatures above $200\text{ }^{\circ}\text{C}$, hardness isotherms show a marked increase followed by a softening. ^[Ar67] For example, at $340\text{ }^{\circ}\text{C}$ hardness peaks at 300 HV after 30 minutes. On a related note, the Young's modulus exhibits the same behavior during isothermal annealing. ^[Br71] However, there is some contention ^[Ar70,Ra70] as to the veracity of the trend just described with respect to the hardness, contradicted by another study ^[Ch70] showing a steady increase at all temperatures.

At room temperature, the main mode of deformation in the AuCu I phase is slip along the close-packed $\{111\}$ planes. ^[Sy67] Among the six $\langle 110 \rangle$ glide directions in these planes, only two allow single dislocations to move without destroying order, namely those two that also lie in the (001) plane populated by like atoms. Glide in the other four directions is effected by superdislocations. These are pairs of ordinary dislocations separated by a strip of anti-phase domain. Both move simultaneously and thus preserve order after their passage.

Domain boundaries present strong obstacles to dislocation glide, as the change of symmetry reassigns the roles of single and superdislocations and it will require extra energy to reconstruct one type into the other. ^[Sy67] Similar arguments can be made for the passage of dislocations between ordered and disordered regions. ^[Ar67] In fact, as the electron micrograph in figure 1.11 attests, slip bands in

alloy	mass fraction						
	Au	Pd	Cu	Fe	Ag	In	Ga
Au 5125	75.0	12.5	9.5		3.0		
Au 5130	75.0	13.0	10.0			1.5	0.5
Au 5150	75.0	15.0	4.0	6.0			
Au 8150	75.0	15.0	4.0	4.0		1.5	0.5
Au 5210	75.0	21.0				3.5	0.5
alloy	atom fraction						
	Au	Pd	Cu	Fe	Ag	In	Ga
Au 5125	56.4	17.4	22.1		4.1		
Au 5130	56.0	18.0	23.1			1.9	1.1
Au 5150	55.0	20.4	9.1	15.5			
Au 8150	56.2	20.8	9.3	10.6		1.9	1.1
Au 5210	61.8	32.1				5.0	1.2

Table 1.3: Nominal composition of the (main) white gold alloys studied in this work, in weight-% and corresponding atomic-%.

AuCu I are by and large confined to ordered domains; only few slip bands cross domain boundaries or even leave a twin-lamellae needle.^[Sy67] The limiting effect of AuCu I ordered domain boundaries on dislocation mobility explains the resistance to deformation and thus the increase of hardness that comes along with atomic ordering in the L1₀ type superstructure.

1.4 White Gold

The white golds investigated in this work are all palladium-based. Compositions are given in table 1.3. Modifications of these alloys, produced over the course of this study in order to elucidate the role of particular alloying elements, are not listed. Note that the last three digits of the alloys' designations denote the nominal palladium fineness.

With up to six different elements in the mix, the white golds are much more diverse than the yellow golds. Conventional palladium-based white gold, common before the 1990's, were based on the gold–palladium–*silver* system.^[No94] The more modern alloys investigated here are for the most part based on gold–palladium–*copper*.

As explained earlier, the interaction between the electronic structures of palladium and gold is responsible for the strong bleaching effect. Empirically, around 12 weight-%, or about 17 atomic-%, is the minimum amount required in an 18-carat gold to ensure a sufficiently pleasing white color. Most alloys do not exceed 15 weight-% as the palladium content is a major cost factor. Iron has proven effective as a bleaching agent, comparable to nickel but less efficient than pal-

alloy	solution-treated	work-hardened	age-hardenable?
Au 5125	145 HV	235 HV	no
Au 5130	160 HV	280 HV	yes
Au 5150	145 HV	255 HV	no
Au 8150	135 HV	260 HV	yes
Au 5210	120 HV	225 HV	yes

Table 1.4: Vickers hardness of white gold alloys after solution-treating and work-hardening (cold deformation to 75%); data courtesy of Varinor.

adium.^[OC78] In these alloys, iron and, to a lesser extent, silver act as secondary whiteners.

The addition of copper improves the alloys' mechanical properties. Conventional 18-carat Au–Pd–Ag white gold would have a Vickers hardness as low as 70 HV after solution treatment.^[Su80] Ideally, though, hardness in this ductile state should be comprised between 120 and 150 HV.^[OC78] Compared to gold, palladium and silver, copper's atomic radius is 10 to 12% smaller. In the solid solution, copper atoms will therefore cause lattice distortions that may act as pinning centers for dislocations and thus decrease their mobility — a mechanism known as solid-solution hardening. The same argument can be made for iron.

As a matter of fact, table 1.4 shows that the solution-treated Au–Pd–Cu white golds are mostly within the ideal hardness range mentioned above. Furthermore, they are sufficiently ductile, sustaining cold deformation of 75% and more. However, in the work-hardened state most alloys in the series have hardness values well below the target of 300 Vickers. Others age-harden during thermal treatment at a temperature around 800 K, though a peak hardness near 220 HV for Au 5130 (measured in our lab) leaves room for improvement.

The mechanism of age-hardening remains to be investigated. Order-hardening, as it occurs in yellow gold, is one of the candidates. Figure 1.12 shows a section of the ternary Au–Pd–Cu diagram at 350 °C. A number of ordered phases feature in it, most notably one of L1₀ type superstructure, the tetragonal symmetry of which is cut out for increasing hardness as explained in the previous section. A marker indicates the approximate position of Au 5130, neglecting the additions of indium and gallium. It is situated rather far from the L1₀ ordering region, which starts at copper contents of 35 atomic-%. Likewise, Au 5210, containing no copper, is located somewhere between two possible ordering regions of different symmetry on the binary Au–Pd phase diagram, reproduced in figure 1.13.

It is however difficult to predict the phase equilibrium of any of the alloys based on those diagrams alone. Alloying additions such as indium, gallium or even iron change the chemistry of the solid solution. This may promote or hinder the formation of ordered phases. Furthermore, below the 350 °C section depicted in figure 1.12, the ordering regions will expand further. In yellow gold for example, ordering still takes place at temperatures as low as 150 °C, albeit over a couple of days.

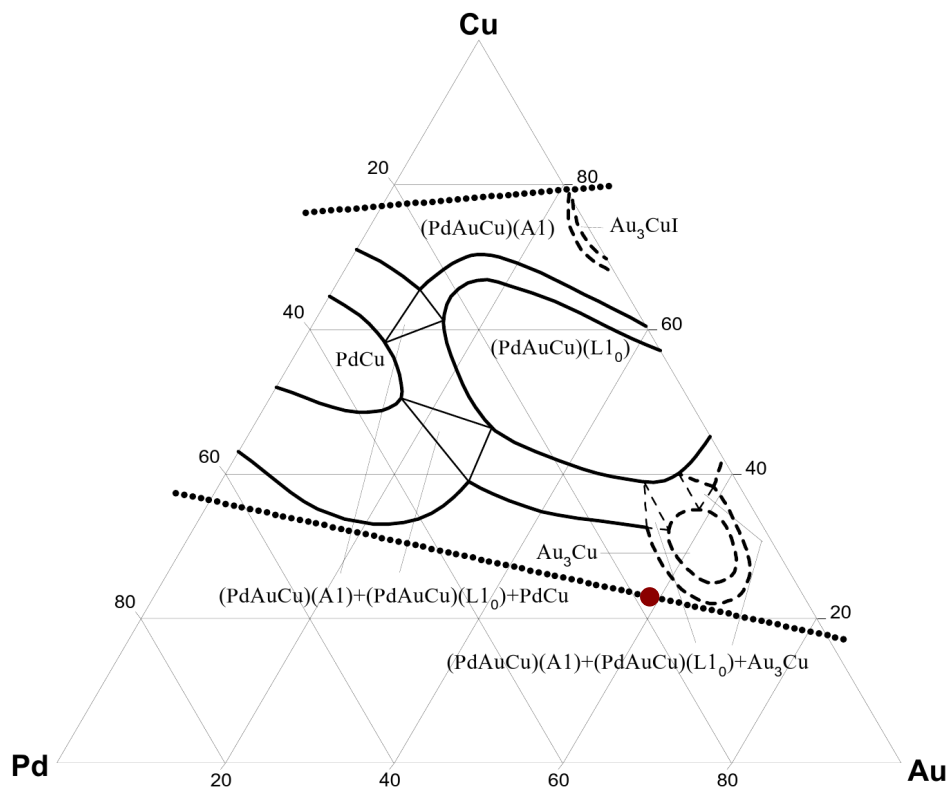


Figure 1.12: Section at 350 °C of the Au–Pd–Cu ternary phase diagram, reproduced from reference [Bo06](#) with an extra marker indicating the position of alloy Au 5130 (neglecting the indium and gallium content).

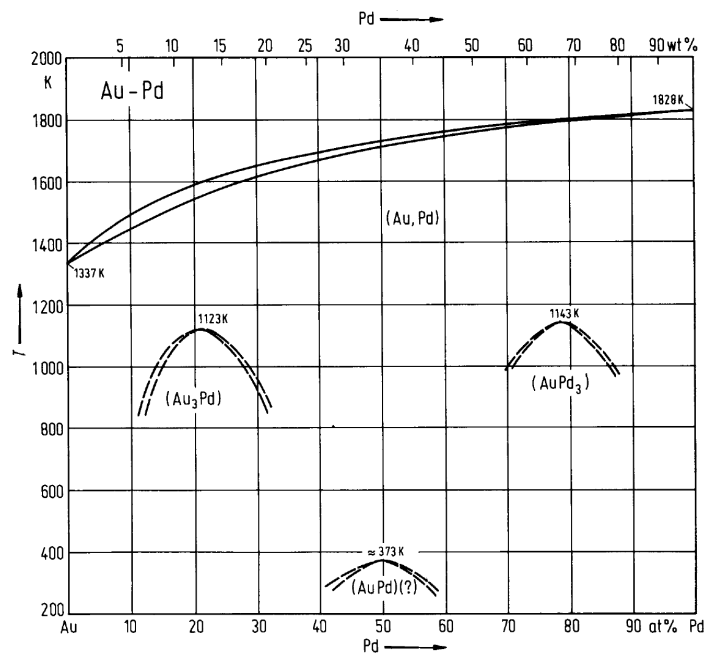


Figure 1.13: Binary phase diagram Au–Pd, from reference [AuPd](#).

Another possible hardening mechanism may be the precipitation of a second phase. In fact, as the Au–In and Au–Ga phase diagrams in figures 1.14 and 1.15 reveal, gold forms a number of intermetallic compounds with either of these two elements. The same is true for Pd–In and Pd–Ga. Whether or not any of the compounds are stable in the Au–Cu–Pd solid solution is as questionable as for the ordered phases. A strong indicator towards this hardening mechanism may be seen in the fact that the age-hardenability of these alloys (table 1.4) correlates with the presence of indium and gallium (table 1.3).

The main intent behind the indium and gallium additions is, however, to offset one major shortcoming of palladium-based white gold: the increased melting temperature, see figure 1.13. As their respective phase diagrams in figures 1.14 and 1.15 indicate, small quantities of indium and, even more so, gallium considerably reduce the liquidus temperature of the solid solution with gold. To make an alloy suitable for conventional manufacturing techniques, a liquidus temperature below 1100 °C is desirable.^[No92]

1.5 Outlook

From the outset, the research goal of this thesis was to conduct a systematic study by mechanical spectroscopy of the two afore-described 18-carat gold alloy series. Mechanical spectroscopy reports the internal friction and dynamic (shear or Young’s) modulus of a specimen as a function of temperature or (excitation) frequency.^[Q⁻¹] Despite their wide commercial availability and importance in their field of application, these materials have never been the subject of such studies. A thorough interpretation of their mechanical loss spectra, which reflect the motion of point defects, dislocations as well as grain boundaries, will advance the understanding of the physics governing their mechanical properties.

Mechanical spectroscopy has been performed on Au–Cu. In the solid solution, a Zener relaxation peak, due to the reorientation of lattice distortions caused by the smaller copper atoms, was found over the entire composition range.^[Mo67,Bo72] The evolution of the Young’s modulus with temperature permits to distinguish between α -AuCu, AuCu I and AuCu II.^[Co74] In AuCu₃, the anisotropy of the Zener relaxation^[Po83,Po84] as well as non-linear effects near the order–disorder transition^[Mi83] have been studied in more detail.

Consequently, in a first step the Zener relaxation in 18-carat gold alloys will be the focus of attention. Chapter 4 will demonstrate a novel way to detect the order–disorder phase transition that, if complemented with a model for the ordering reaction, may even yield a theoretical prediction of transformation times. Furthermore, we will see that while a Zener relaxation also occurs in white gold, signs of atomic ordering are minimal, to the point that the possibility of order-hardening in these alloys can be virtually excluded.

Precipitation of second-phase intermetallic particles was the prime candidate for the hardening mechanism in white gold, as outlined in the previous section. Chapter 5 will prove that such a phenomenon does indeed occur. First, it will be shown that a feature common to the spectra of all 18-carat gold alloys is a relaxation peak due to grain boundary sliding. Second, we will see that second-phase particles impede this relaxation mechanism by blocking grain boundaries as soon as they precipitate. When the particles go back into solution at high temperature, the grain boundary peak reappears. The empirically determined age-hardening treatments performed on these alloys are well accounted for by the temperature of precipitation/dissolution.

Recrystallization of cold-worked material is another phenomenon of practical importance. During various steps of the working process, the material suffers plastic deformation, rendering it harder but also less ductile. In order to restore formability, accumulated dislocations need to be annealed out. During the recrystallization heat treatment, dislocations will disentangle, polygonize and form low-angle subgrain boundaries that will be the nuclei of a new grain structure. The heat treatment has to be well controlled to ensure an optimum structure of fine and equiaxed grains. Mechanical loss spectra presented in chapter 3 will show that the second-phase particles delay the recovery and restoration process.

Chapter 2

Experiments

Mechanical spectroscopy performed by means of a low-frequency inverted torsion pendulum is the main experimental technique used in this study. It will be explained in appropriate detail over the next two sections. Complementary methods, such as hardness testing, X-ray diffraction and the growth of single crystals are described afterwards.

2.1 Mechanical spectroscopy

Ordinarily, the deformation a solid undergoes when subject to an external stress is classified in two categories: elastic and plastic.

Elastic deformation occurs/vanishes instantaneously upon loading/unloading. At any moment t , the stress–strain relationship of a simple mode of deformation, such as uniaxial tension or shear, is then described by Hooke’s law:

$$\sigma(t) = M \epsilon(t), \quad (2.1)$$

where M denotes the elastic (Young’s or shear) modulus.¹ It is useful to rewrite Hooke’s law as

$$\epsilon(t) = J \sigma(t), \quad (2.2)$$

with the elastic compliance $J = M^{-1}$.

Whenever the applied stress exceeds the elastic limit, the solid will no longer recover its initial shape after unloading: plastic deformation has occurred. If that is the case, some of the energy supplied to the solid during the deformation process, i.e.

$$W = \int_0^{\epsilon} \sigma(\epsilon') d\epsilon', \quad (2.3)$$

¹In a torsion pendulum, the relevant mode of deformation is shear. Shear stress/angle/modulus (τ, γ, G) then take the place of σ, ϵ and M . For an arbitrary deformation, the theory presented in this section can be generalized by replacing the scalar quantities with tensors.

is lost, either dissipated as heat or stored in remnant internal strain fields. Only the elastic part of the total strain energy can be retrieved. By using Hooke's law in equation (2.3), it is easily found to equal

$$W_{\text{el}} = \frac{1}{2} M \epsilon^2 = \frac{1}{2} J \sigma^2. \quad (2.4)$$

A third category of deformation can be defined if one relinquishes the criterion of instantaneity, but maintains that of full shape recovery (in the infinite time limit). Such a deformation is known as *anelastic* or *viscoelastic*. Since the strain no longer follows the stress immediately, some energy is dissipated inside the solid via mechanical (anelastic) relaxations, namely the motion of structural defects. *Internal friction*, or *mechanical loss*, defined as

$$F = \frac{1}{2\pi} \frac{\Delta W}{W_0}, \quad (2.5)$$

is a measure of this damping in the case of periodic deformations, relating the energy dissipated during a strain cycle,

$$\Delta W = \oint \sigma(\epsilon) d\epsilon, \quad (2.6)$$

to the maximum elastic energy W_0 stored in the solid at some point of that same cycle. W_0 is essentially W_{el} of equation (2.4), with stress or strain replaced by their respective amplitudes.

In the anelastic regime, the total strain is the sum of two contributions:

$$\epsilon = \epsilon_{\text{el}} + \epsilon_{\text{an}}.$$

The elastic strain is the instantaneous reaction to the current stress field. The anelastic strain, however, being the result of various evolving relaxation processes that began in the past, may depend in a complicated way on the history of loading. A common simplification of problems of this type is to disregard all terms beyond the linear response of the system.^[Ku57] Then:

$$\epsilon(t) = J_u \sigma(t) + \int_{-\infty}^t \chi(t-t') \sigma(t') dt'.$$

Here, the elastic susceptibility $\chi(t-t')$ accounts for the contribution of a unit impulse (δ -peak) of stress at time t' to the anelastic strain at time t . J_u denotes the *unrelaxed* elastic compliance, the same that figures in Hooke's law (2.2). More useful is the Fourier transform of the above equation, as it deconvolutes stress and susceptibility:

$$\epsilon(\omega) = J_u \sigma(\omega) + \chi(\omega) \sigma(\omega).$$

Defining the complex compliance as

$$J(\omega) = J_u + \chi(\omega)$$

along with the complex modulus $M = J^{-1}$, one finds a generalized Hooke's law in Fourier space:

$$\epsilon(\omega) = J(\omega)\sigma(\omega) \quad \text{or} \quad \sigma(\omega) = M(\omega)\epsilon(\omega). \quad (2.7)$$

Now consider the application of a harmonic stress of constant amplitude, $\sigma(t) = \sigma_0 e^{i\omega t}$, i.e. $\sigma(\omega) \propto \sigma_0 \delta(\omega)$. It follows immediately from (2.7) that strain is also harmonic, $\epsilon(t) = \epsilon_0 e^{i(\omega t - \varphi)}$, lagging behind stress by the *loss angle*

$$\varphi(\omega) = \arg M(\omega) = -\arg J(\omega)$$

which is thus equal to the phase of the complex modulus, while the amplitude ratio is given by its absolute value, also known as the *dynamic modulus*:

$$\frac{\sigma_0}{\epsilon_0(\omega)} = |M(\omega)| = \frac{1}{|J(\omega)|}.$$

It is straightforward to show that the *loss tangent* $\tan \varphi$ is equivalent to the mechanical loss defined in equation (2.5). That is, as long as the linear response theory is valid (the strain response varies linearly with the stress excitation's amplitude), we have

$$F(\omega) = \tan \varphi(\omega).$$

Finally, in an experiment of mechanical spectroscopy, the mechanical loss (in the form of the loss tangent) along with the dynamic modulus is reported as a function of either frequency ($f = \frac{\omega}{2\pi}$) or, as we will see further down, temperature.

A model for a large number of mechanical relaxation processes — particularly those driven by atomic diffusion — is the standard anelastic solid, sketched in figure 2.1. The spring in series, of compliance J_u , accounts for the instant elastic response of the solid. The dashpot simulates a viscous friction mechanism, with its piston moving in a liquid of viscosity η . The stress σ' applied to the dashpot is proportional to its strain rate: $\sigma' = \eta \dot{\epsilon}'$. As the dashpot relaxes, the spring in parallel gradually contributes the extra compliance δJ . One readily finds the standard anelastic solid's equation of motion to be^[NB³]

$$J_r \sigma + \tau_\sigma J_u \dot{\sigma} = \epsilon + \tau_\sigma \dot{\epsilon}, \quad (2.8)$$

where $J_r = J_u + \delta J$ denotes the *relaxed* compliance (total compliance at infinite time) and $\tau_\sigma = \eta \delta J$ the time constant of relaxation at constant stress. We also note, still from equation (2.8), that the relaxation time at constant strain ($\dot{\epsilon} = 0$) is $\tau_\epsilon = \tau_\sigma \frac{J_u}{J_r}$.

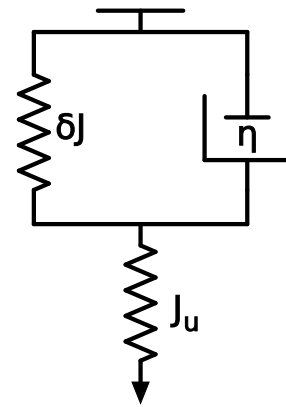


Figure 2.1: Rheological model of the standard anelastic solid.

Solving the equation of motion is once more facilitated by a Fourier transform, as it turns all time derivatives into simple multiplications by $i\omega$. For the complex compliance one easily finds:

$$J(\omega) = \frac{\epsilon(\omega)}{\sigma(\omega)} = \frac{J_r + i\omega\tau_\sigma J_u}{1 + i\omega\tau_\sigma}.$$

Calculating the tangent of $-\arg J(\omega)$ yields the mechanical loss. After introducing the relaxation strength

$$\Delta = \frac{\epsilon_{\text{an}}(t \rightarrow \infty)}{\epsilon_{\text{el}}} = \frac{\delta J}{J_u} \quad (2.9)$$

as well as the average relaxation time

$$\tau = \sqrt{\tau_\sigma \tau_\epsilon},$$

one can express the result as follows:

$$F(\omega) = F_0 \frac{2\omega\tau}{1 + \omega^2\tau^2}. \quad (2.10)$$

$F(\omega)$ describes a Debye peak, thus named after Dutch physicist Peter Debye who first derived it for the case of dielectric relaxations.^[NB³] The peak reaches its maximum F_0 at $\omega = 1/\tau$. The peak height is related to the relaxation strength as per

$$F_0 = \frac{1}{2} \frac{\Delta}{\sqrt{1 + \Delta}} \approx \frac{\Delta}{2} \quad \text{for } \Delta \ll 1. \quad (2.11)$$

Conversely, and of more practical importance, one retrieves the relaxation strength from the peak height according to

$$\Delta = 2F_0 \left(F_0 + \sqrt{1 + F_0^2} \right) \approx 2F_0 \quad \text{for } F_0 \ll 1. \quad (2.12)$$

Mechanical loss frequency spectra are usually plotted versus a logarithmic scale, as it confers the Debye peak a symmetric shape:

$$F(\ln \omega) = \frac{F_0}{\cosh(\ln \omega + \ln \tau)}. \quad (2.13)$$

For a deca-logarithmic scale, this is illustrated in figure 2.2. The Debye peak spans roughly four decades and is 1.144 ($= 2\log_{10}(2 + \sqrt{3})$) decades wide at half its height.

Many anelastic relaxations, since they take place at the atomic level, are diffusion-controlled. Therefore, the relaxation time τ generally follows an Arrhenius equation:

$$\tau = \tau_0 \exp\left(\frac{H_{\text{act}}}{kT}\right). \quad (2.14)$$

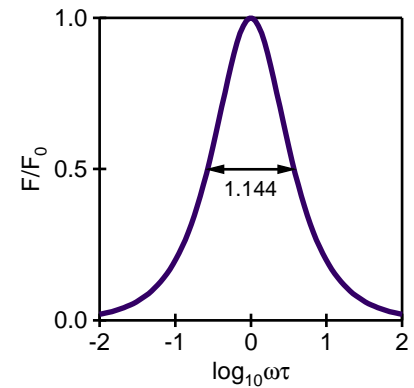


Figure 2.2: Debye peak over four logarithmic decades of the angular frequency spectrum.

H_{act} denotes the activation enthalpy², τ_0 the limit relaxation time. The equation describes a thermally activated system trying time and again, at an attempt frequency ν_0 , to overcome an energy barrier. At infinite temperature T the effect of the barrier becomes insignificant and $\tau_0 = 1/\nu_0$.

An Arrhenius plot reports $\ln \tau$, as obtained directly from the peak's position, versus the temperature at which the frequency spectrum was recorded. Slope and intercept of the regression line then yield H_{act} and τ_0 . If, due to experimental restrictions, only a flank of the peak appears in the spectrum, the shift with temperature of a point of constant mechanical loss will at least yield the activation enthalpy. This often comes in handy when a thermally activated background needs to be subtracted.

It shall be noted that the entropy change of the activated state (with respect to initial and final state) was neglected in this consideration, as is customarily done. The actual energy barrier of the process is given by the variation of the Gibb's free enthalpy,

$$\Delta G = \Delta H - T\Delta S, \quad (2.15)$$

and not just $H_{\text{act}} = \Delta H$. While the term $T\Delta S$ does not change the slope of the exponential (the temperature factor cancels out in the Arrhenius equation), it does alter the pre-exponential factor τ_0 . If the system is at thermal equilibrium, the entropy change during thermal activation must be positive. Therefore, should the entropy term play a role, one would measure an activation enthalpy apparently too high and a smaller limit relaxation time.

During the anelastic evolution of the rather complex microstructure of most materials, more than one relaxation process will come into play. If each of those can be described by a standard anelastic solid, the full mechanical loss spectrum will be a superposition of Debye peaks with corresponding relaxation strengths and relaxation times.

If thermal activation is involved, the mechanical loss of the standard anelastic solid, described by the Debye equation (2.10), has an indirect temperature dependence via the relaxation time (2.14). Since τ varies exponentially with T , one can explore larger parts of the full spectrum, possibly containing peaks with relaxation times of different orders of magnitude, by plotting the mechanical loss versus temperature instead of frequency.

More often than not, one will find that, for a given relaxation, the relaxation time is not a well-defined entity, but rather varies continuously over a certain interval. This results in a broadening of the corresponding peak in the mechanical loss spectrum. Since it is difficult to know exactly how the relaxation times are distributed, one usually assumes that they scatter around some mean value τ_m according to a lognormal distribution:

$$\psi(z) = \frac{1}{\sqrt{\pi} \beta} \exp\left(-\frac{z^2}{\beta^2}\right) \quad \text{with } z = \ln \frac{\tau}{\tau_m}. \quad (2.16)$$

²The terms activation enthalpy and activation energy are often used interchangeably.

It is a Gaussian distribution of $\ln \tau$ around $\ln \tau_m$, which in the sense of the Arrhenius equation (2.14) corresponds to a Gaussian distribution of the activation energy barrier around some mean value (provided the attempt frequency ν_0 remains the same).

The distribution parameter β is a measure of the distribution's width. Assuming furthermore that the relaxation strength Δ is the same for all values of τ , β can be obtained from a fitting procedure wherein a broadened Debye peak

$$F^\beta(\ln \omega) = \int_{-\infty}^{+\infty} F(\ln \omega + z) \psi(z) dz \quad (2.17)$$

is compared to the experimental data. Numerically, an integration cut-off at $\pm 3\beta$ is largely sufficient. Note that, as the peak F^β becomes broader, its height decreases. The relaxation strength Δ must still be calculated from the height of the pure Debye peak, F_0 , which appears in (2.17) via $F(\ln \omega)$ from equation (2.13). As F_0 is a priori unknown, it must be fitted along with β .

The next section will explain how the two output variables of mechanical spectroscopy — loss tangent and dynamic modulus — are measured by means of a forced torsion pendulum.

2.2 Forced torsion pendulum

In an inverted torsion pendulum, drawn schematically in figure 2.3, a harmonically varying torque T twists the specimen such that the top surface rotates while the bottom remains fixed. The torsion angle θ is measured by detecting a laser's reflection off a mirror attached to the rod. Temperature is controlled via a furnace surrounding the specimen. The following will show how the signals $T(t)$ and $\theta(t)$ are acquired, and how they relate to shear stress τ , shear strain γ and shear modulus G .

The torque T is applied to the specimen's top by means of a magnetic excitation system: two magnetic coils driven by a harmonic current I , attracting or repelling permanent magnets mounted at the end of levers which are connected to the upper part of the rod, as depicted on the photo in figure 2.4.

The magnitude of the torque T is a priori unknown. It is due to the force the magnetic field exerts on the two permanent magnets attached to the pendulum's rod. With μ the magnetic moment of one such permanent magnet, its potential magnetic energy (in first-order approximation with respect to spatial variations of B) is given by

$$V(\vec{r}) = -\vec{\mu} \cdot \vec{B}(\vec{r}).$$

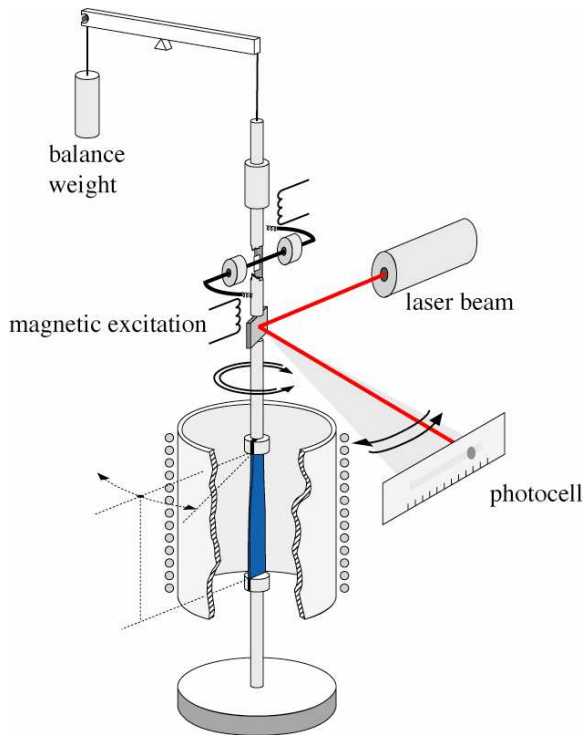


Figure 2.3: Schematic drawing of a low-frequency inverted forced torsion pendulum.

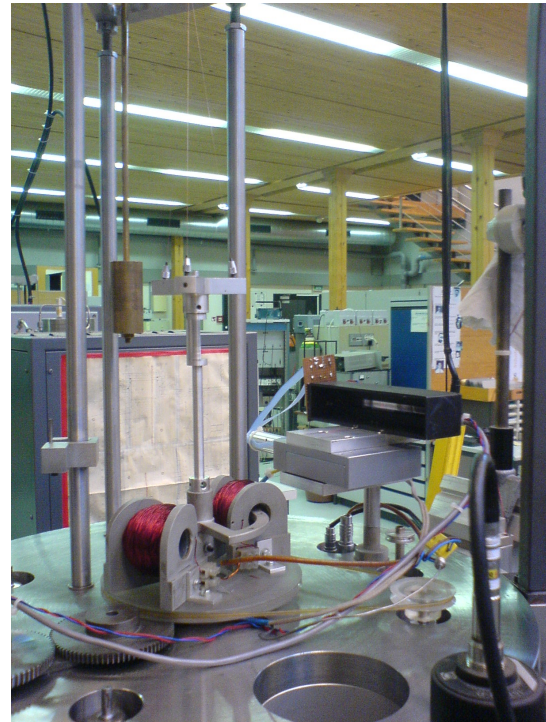


Figure 2.4: Inner workings: magnetic excitation, photocell and upper rod hanging from a three-wire suspension.

Since the permanent magnet is aligned with the coil's axis, $\vec{\mu}$ and \vec{B} are parallel. Hence there will only be a force if the intensity of the magnetic field B produced by the coil varies along its axis. Let z be the coordinate along that axis, then:

$$\vec{F} = -\text{grad } V(\vec{r}) = \mu_z \frac{dB_z}{dz} \vec{e}_z.$$

A straightforward application of the Biot-Savart law

$$\vec{B}(\vec{r}) = \frac{\mu_0 I}{4\pi} \oint \frac{d\vec{l} \times \vec{r}}{r^3}$$

to the geometry of the coil will yield B_z and its gradient. The result is plotted in figure 2.5. For thin coils, the gradient of B_z is maximum at $z \approx \frac{l}{2}$. Therefore the permanent magnets should be positioned right outside the coils, where the coupling is strong and, more importantly, the force hardly varies when the pendulum moves, so as to not distort the harmonic signal. According to the Biot-Savart law the force — and thereby the torque — is then proportional to the current I driving the coils.

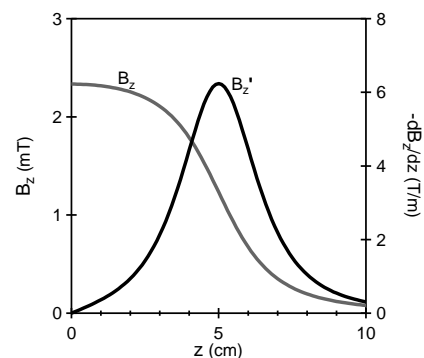


Figure 2.5: Magnetic field component B_z and its gradient created by a coil of 200 turns, 10 cm long, 2 cm in radius, at 1 A driving current as a function of the distance z from the coil's center.

We can thus write

$$T(t) = c V_e(t) \quad (2.18)$$

where V_e denotes the excitation voltage input signal that controls the (linear) current amplifier supplying the coils. The torque factor c is the product of the current amplifier's gain and the magnetic coupling resulting from the geometry. However, since the mounting/unmounting of samples may change the position of the permanent magnets, one is best advised to determine c at the start of each measurement from a calibration procedure such as the one outlined at the end of this section.

The torsion angle θ is retrieved from the second input signal, the photocell's response. Note that θ is well defined regardless of the specimen's geometry, being the angle between any vector within the top surface at torque T and the same vector at zero torque. The response signal

$$V_r(t) = g p D(t)$$

is proportional to the distance D of the laser's spot from the photocell's center. g denotes the post-amplifier's gain, p the photocell sensitivity, a calibration constant converting distance to voltage.

Taking into account that the angle of deviation by the mirror is twice the torsion angle, one finds

$$\theta(t) = \frac{\Delta D(t)}{2L} = \frac{\Delta V_r(t)}{2gpL}. \quad (2.19)$$

ΔD denotes the displacement of the laser's reflexion, i.e. its variation with respect to the zero-stress position. The latter is not necessarily at the photocell's center, meaning that the DC offset of the input signal V_r should be ignored. L designates the horizontal distance separating the mirror from the photocell.

The torsion of the specimen corresponds to a shear of individual volume elements. This shear is not uniform. It will vary throughout the specimen's section, being zero at the center and maximum at some point on the outer edge. The expressions relating torque T and shear stress τ on the one hand, and torsion angle θ and shear angle (shear strain) γ on the other, will thus depend on the specimen's geometry.

Consider first a cylindrical specimen of radius r and length l . From the schematic drawing in figure 2.6 one concludes that for any volume element of coordinates ρ ($0 \leq \rho \leq r$), φ ($0 \leq \varphi \leq 2\pi$), and λ ($0 \leq \lambda \leq l$), the shear angle is related to the torsion angle as

$$\gamma(\rho) = \frac{\rho}{l} \theta.$$

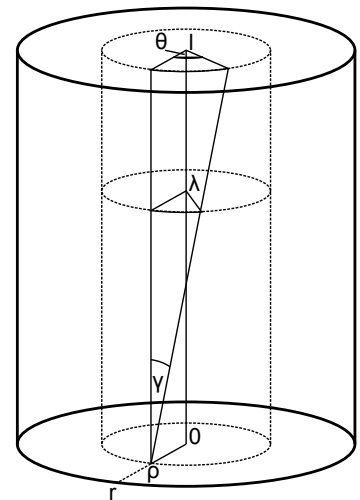


Figure 2.6: Cylinder in torsion.

As for shear stress and torque, we now apply (the generalized) Hooke's law (for the shearing mode of deformation):

$$\tau(\rho) = G\gamma(\rho) = G \frac{\rho}{l} \theta.$$

The shear force acting on an element dS of the specimen's top surface is $\tau(\rho)dS$. The sum of the corresponding moments of force must equalize the applied torque T . Thus

$$T = \int_S \rho \tau(\rho) dS = 2\pi \int_0^r \rho \frac{G \rho \theta}{l} \rho d\rho =: k(G) \theta,$$

where we have introduced the force constant

$$k(G) = \frac{\pi}{2} \frac{r^4}{l} G$$

relating twist angle θ and applied torque T . It is the same k that appears in the equation of motion of the (free or forced) torsion pendulum, as it describes the restoring moment the specimen produces in response to the deformation. The relation can be used to eliminate θ in the expression for τ to obtain

$$\tau(\rho) = \frac{2}{\pi} \frac{\rho}{r^4} T.$$

As indicated above, we find that shear stress and strain vary along the radial coordinate ρ . Experimental data from mechanical spectroscopy typically reports the maximum stress and strain states present in the specimen. In the case of a cylinder, they occur all over the lateral surface, i.e. at $\rho = r$. The volume average differs from it by a factor of $\frac{2}{3}$. Of course, the shear modulus, being given by the ratio of τ and γ , is independent of ρ .

Thus, for a cylinder of length l and radius r , we have found:

$$\tau(T) = \frac{2}{\pi} \frac{T}{r^3} \quad \text{(maximum) shear stress} \quad (2.20)$$

$$\gamma(\theta) = \frac{r}{l} \theta \quad \text{(maximum) shear strain} \quad (2.21)$$

$$G(T, \theta) = \frac{2}{\pi} \frac{l}{r^4} \frac{T}{\theta} \quad \text{shear modulus} \quad (2.22)$$

For a rectangular bar of length l , width w ($w \leq l$) and thickness t ($t \leq w$), the implicit symmetry argument used for finding $\gamma(\rho)$ from figure 2.6 no longer applies. For details of the derivation, the reader is referred to literature:^[Tim]

$$\tau(T) = C_\tau \frac{T}{w t^2} \quad \text{(maximum) shear stress} \quad (2.23)$$

$$\gamma(\theta) = C_\gamma \frac{t}{l} \theta \quad \text{(maximum) shear strain} \quad (2.24)$$

$$G(T, \theta) = C_G \frac{l}{w t^3} \frac{T}{\theta} \quad \text{shear modulus} \quad (2.25)$$

where

$$C_\tau = \frac{C_1}{C_2}, \quad C_\gamma = C_1, \quad C_G = \frac{1}{C_2}$$

with³

$$C_1 = 1 - \frac{8}{\pi^2} \sum_{k=0}^{\infty} \frac{1}{(2k+1)^2 \cosh\left(\frac{\pi}{2}(2k+1)\frac{w}{t}\right)}$$

and

$$C_2 = \frac{1}{3} - \frac{64}{\pi^5} \frac{t}{w} \sum_{k=0}^{\infty} \frac{\tanh\left(\frac{\pi}{2}(2k+1)\frac{w}{t}\right)}{(2k+1)^5}.$$

So far, we have tacitly assumed that, at any moment t , the specimen is in mechanical equilibrium, i.e. the restoring moment provided by the specimen compensates the external torque applied by the magnetic excitation. This quasi-static treatment of a dynamic measurement requires justification, as the system is obviously *in motion* during the experiment. In fact, the forced torsion pendulum's equation of motion,

$$J \ddot{\theta} + k(G(\omega)) \theta = T_0 e^{i\omega t},$$

naturally contains the acceleration term involving the pendulum's moment of inertia J . This will, in principle, shift the measured phase lag δ between the two signals T and θ away from the phase lag φ between τ and γ , i.e. the actual loss angle, and will also affect the amplitude ratio T_0/θ_0 that, via equations (2.22) or (2.25), yields the dynamic modulus $|G(\omega)|$. These problems can only be avoided if measurements are made in subresonant mode, at $\omega \ll \omega_r$, where the two phase shifts are approximately equal. More precisely, one can show that^[Iw82]

$$\tan \varphi(\omega) = \left(1 - \frac{\omega}{\omega_r}\right) \tan \delta(\omega),$$

where ω_r is the resonant frequency of the pendulum–specimen system.

The resonant frequency is close to the pendulum's eigenfrequency in free mode,

$$\omega_e = \sqrt{\frac{k(G(\omega_e))}{J}},$$

for as long as the friction coefficient is relatively low. The eigenfrequency on the other hand, which can be easily measured after turning off the excitation signal, contains another interesting information: it can be used to calibrate the imprecisely known torque factor c (equation (2.18)) at the start of an experiment, after

³Note that the result for C_1 reported in reference [Rek](#) (and cited in a previous thesis prepared in our group^[Fi02]) differs slightly (sinh instead of cosh), which, upon closer inspection, is clearly a misprint. Also, the two power series converge quickly and can be readily calculated in real-time during measurements.

mounting the specimen. With the pendulum's inertia J determined once and for all, and $k(G) = \frac{T}{\theta}$ given by equation (2.22) for the cylinder or equation (2.25) for the rectangular bar, ω_e provides an independent measurement of the dynamic shear modulus. It can be compared to the result obtained in forced mode from the amplitude ratio. The procedure must be performed at a temperature where the variation of the dynamic modulus between the two frequencies ω and ω_e is negligible.

This calibration feature was introduced in the data acquisition program controlling the pendulum more than halfway through the work for this thesis. Therefore, earlier results report the shear modulus in arbitrary units, as the shear stress amplitude was unknown.

2.3 Hardness tests

The hardness of a metal is perceived as the resistance it offers to local plastic deformation. A common and simple method to measure it is provided by the Vickers hardness test: an indenter with a diamond tip in the shape of a square-based pyramid is pressed onto the specimen's surface at a specified load. The resulting indentation is observed in an optical microscope where its size can be measured. Generally, hardness (not just Vickers hardness) is defined as the ratio of applied force to area of indentation and traditionally given in kilogram-force per square millimeter.^[Ta70] Owing to the geometry of the tip, the Vickers hardness is therefore:

$$H_V = 2 \sin(68^\circ) \frac{m}{d^2},$$

where d denotes the indentation pyramid's diagonal and m the load mass. Alternatively, hardness values may be given in GPa by an obvious conversion.

Vickers hardness was measured using the Leitz hardness tester depicted in figure 2.7 at a load of $m = 0.3$ kg.



Figure 2.7: Leitz hardness tester.

2.4 X-ray diffraction

X-ray θ - 2θ powder diffraction was performed on some specimens to confirm the presence or absence of atomic ordering in the bulk. As the quantitative evaluation of peak intensities was not an issue, polycrystalline samples were measured as they were, i.e. no actual powder was ground.

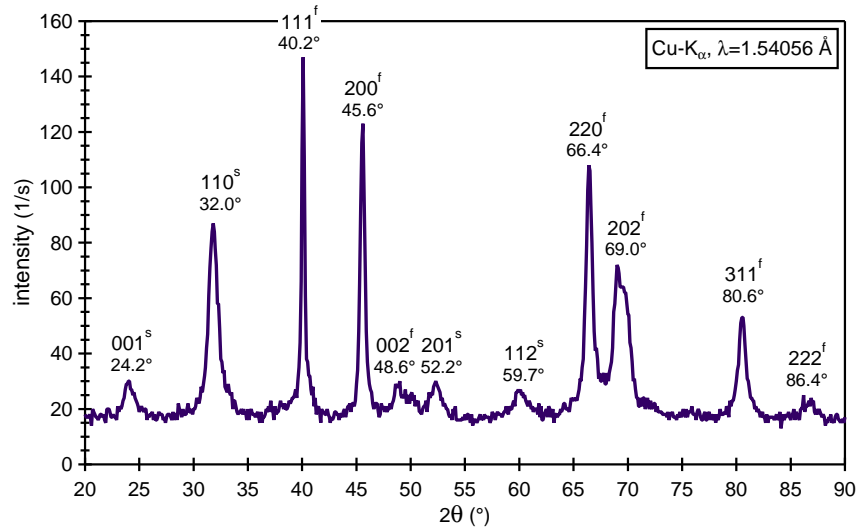


Figure 2.8: X-ray θ - 2θ diffraction spectrum of a slow-cooled, polycrystalline Au 518 sample, showing fundamental (f) reflections of the f.c.c. crystal lattice and superstructure (s) reflections from the AuCu I type ordered phase.

Compared to the disordered solid solution, atomic ordering always manifests itself in the X-ray spectrum by the appearance of extra reflections, particularly at the low-angle end. Say, for example, the Bragg diffraction condition

$$n \frac{\lambda}{2d} = \sin \theta$$

in first order ($n = 1$) is fulfilled for a family of lattice planes of inter-planar spacing d that are crystallographically equivalent in the solid solution. If, within the same family of planes in the ordered phase, alternating planes are populated by atoms of different scattering power, some of the intensity will shift to a peak corresponding to twice the inter-planar spacing, $2d$, i.e. at (very roughly) half the diffraction angle θ .

For the AuCu I phase, this is true for planes such as (110) and (001), see figure 1.6 on page 10 for illustration. Figure 2.8 shows the X-ray spectrum of Au 518; the peaks corresponding to the AuCu I type superstructure feature prominently.

2.5 Growth of single crystals

In an effort to understand the role of grain boundaries in the mechanical loss spectra, monocrystals were produced by means of the vertical Bridgman method.

To that end, as illustrated in figure 2.9, the polycrystalline source material is introduced into a graphite crucible and sealed with a quartz tube under vacuum. Powered by a high-frequency generator, an induction furnace heats the crucible above the material's melting temperature, which would be verified with a pyrometer. Through a small orifice at the crucible's bottom end, some of the

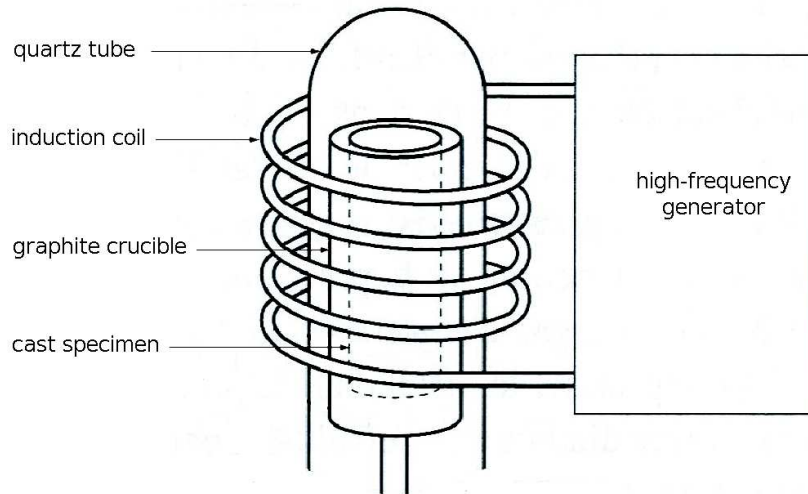


Figure 2.9: Growth of a single crystal from melt heated inside a graphite crucible by an induction furnace.

melt escapes. As the entire crucible is being slowly retracted from the furnace's center (at less than 1 mm/min), the lowest part of the melt solidifies in a polycrystalline state, but the one grain reaching through the small hole in the crucible will serve as a seed for a single crystal (of arbitrary orientation) growing from the rest of the melt.

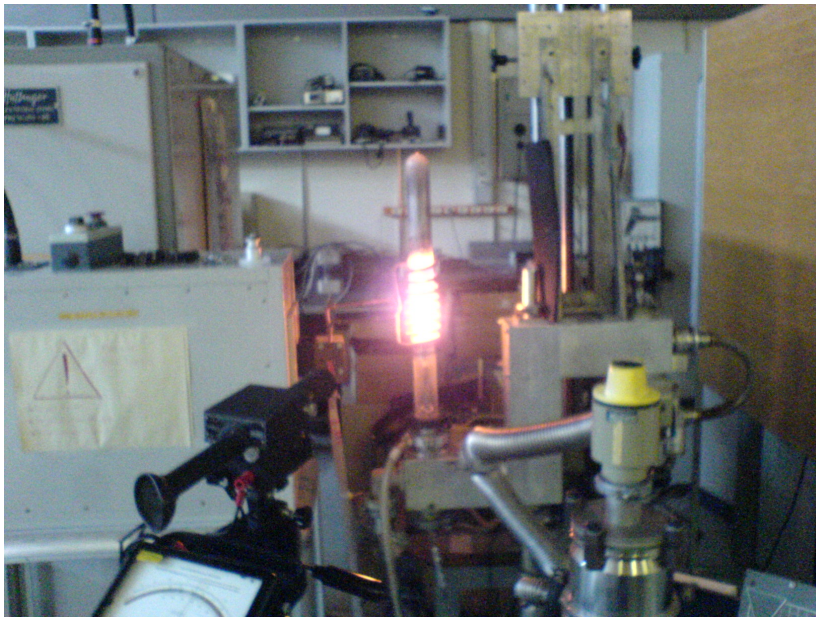


Figure 2.10: Heated graphite crucible inside quartz tube (center), high-frequency generator (to its left), pyrometer (front left), and vacuum pump (front right).

Chapter 3

Anelastic Relaxations in 18-carat Gold

This chapter provides a phenomenological overview of mechanical relaxations occurring in 18-carat gold alloys between room temperature and melting point. The alloys' mechanical loss spectra measured as a function of temperature will be presented and explained, differences and similarities throughout the two alloy series pointed out. The two chapters following this one will each focus on a single feature, first the Zener relaxation, then grain boundary sliding, and lay out in detail if and how theory accounts for these results.

3.1 Yellow Gold

The mechanical loss spectra of the yellow gold alloys all show the same characteristic features. Results for alloys Au 118 and Au 518 are presented in figures 3.1 and 3.2 as examples. Below 500 K the spectrum is flat. This is due to the limited sensitivity of the forced pendulum, which (as opposed to free vibration techniques) cannot resolve mechanical loss levels much below 10^{-3} . At around 600 K a first peak appears, followed by a second peak at about 720 K. At high temperature, there is a noticeable increase of the background.

The first peak is associated with a Zener relaxation. The theoretical basis for this relaxation phenomenon as well as an in-depth analysis of the peak will follow in chapter 4.

Owing to the presence of atoms of varying sizes, the crystal lattice of most disordered substitutional alloys is distorted. For AuCu for example, this has been concluded from x-ray absorption fine structure (XAFS) studies backed up by computer simulations; the result is illustrated in figure 3.3.^[Fr00] The distorted lattice represents an incommensurate state, i.e. the bond angle variations are random.

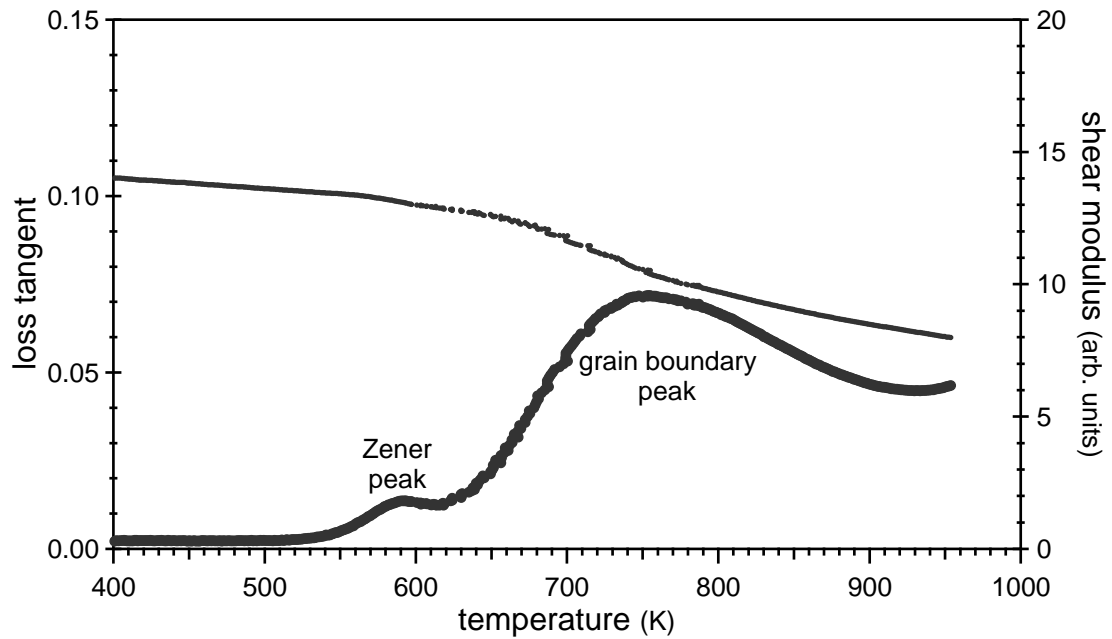


Figure 3.1: Mechanical loss temperature spectrum of Au 118 (Au-Cu_{10%}-Ag_{30%}) at 0.5 Hz excitation frequency and 1 K/min cooling rate.

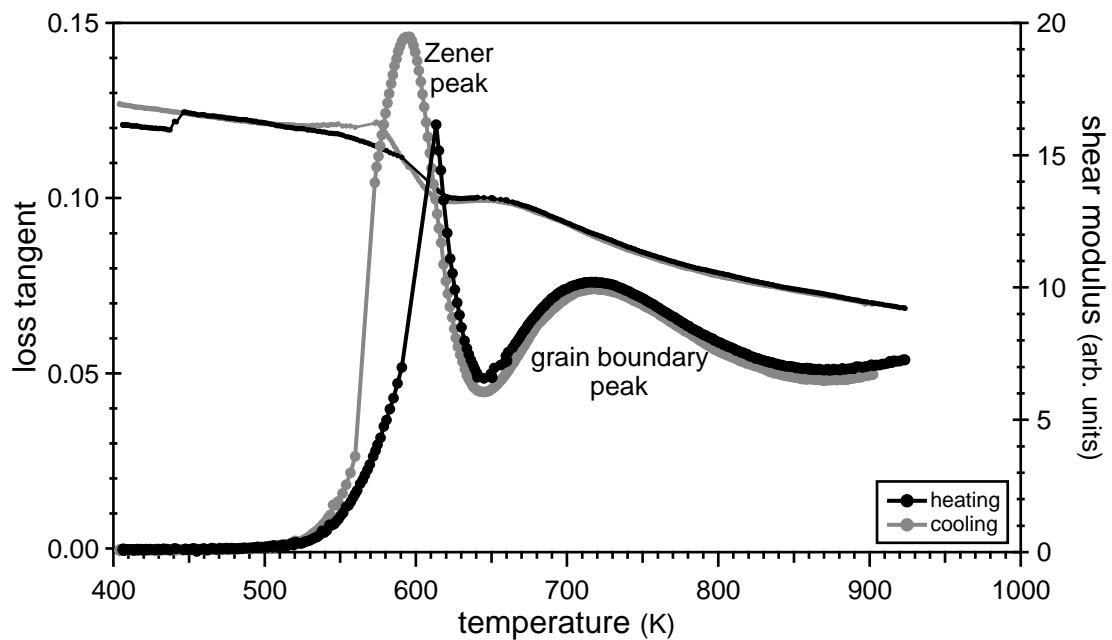


Figure 3.2: Mechanical loss temperature spectrum of Au 518 (Au-Cu_{43%}-Ag_{6%}) at 0.5 Hz excitation frequency and 1 K/min heating/cooling rate.

In Au–Cu–Ag, the copper atoms are undersized compared to gold and silver. The Zener peak in Au–Cu–Ag can then be understood as changes in the local arrangement of copper atoms. They accommodate an applied stress by reorienting short bonds towards directions in compression, long bonds towards those in tension.

Consequently, the Zener relaxation is driven by diffusion of single atoms to neighboring sites. Again, since copper is the smallest atom species, there is good reason to believe it is the also fastest diffuser. Therefore, the relaxation time corresponding to the Zener peak is a measure of the diffusion coefficient of copper atoms embedded in a Au–Cu–Ag matrix. The activation enthalpy was found to increase with copper content, from 1.6 eV in Au 118 to 2.6 eV in Au 518 (see chapter 4). Therefore the peak tends to shift to higher temperatures throughout the series Au 118 to Au 518.

The height of the Zener peak, and thus its relaxation strength, also varies greatly with copper content. The Zener peaks as they appear in the corresponding temperature spectra, but after background subtraction, are shown in figure 3.4. The dependence of the peak height on the copper concentration, as revealed in figure 3.5, is not a simple linear or quadratic function. The more sophisticated analysis in chapter 4 will address this issue.

More importantly, the Zener peak is affected by atomic ordering. As one may observe on Au 518’s temperature spectrum in figure 3.2, there is an abrupt change in the mechanical loss on the Zener peak’s low-temperature flank in cooling. In

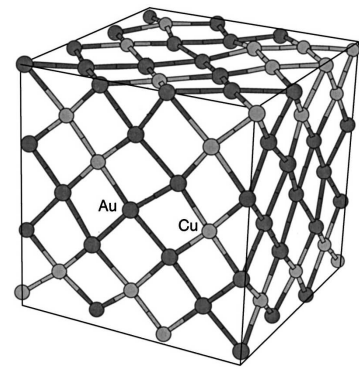


Figure 3.3: Distorted lattice of α -AuCu according to XAFS measurements and computer simulations from reference Fr00.

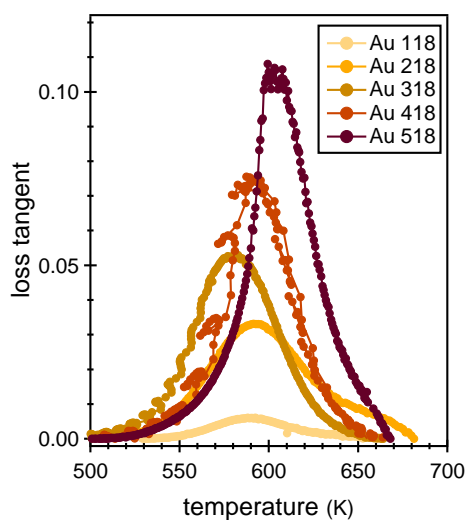


Figure 3.4: Zener peaks of the yellow gold alloys (after background subtraction, in heating).

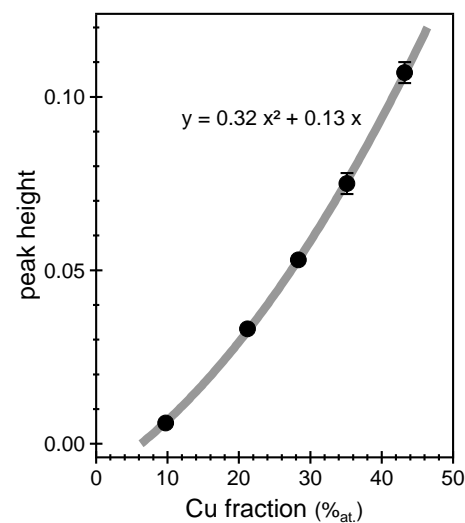


Figure 3.5: Height of the Zener peak in the various temperature spectra as a function of the copper atom fraction.

heating, the Zener peak's maximum is suppressed and only the high-temperature side appears in the spectrum. The sharp drop-off in cooling and the retarded increase in heating both result from the fact that the excitation frequency of 0.5 Hz was chosen such that the Zener relaxation occurs in the same temperature range as the order–disorder phase transition.

Ordered phases do not contribute (or contribute very little) to a Zener relaxation process. In a perfectly ordered (i.e. stoichiometric) structure, local lattice distortions, as they occur in the solid solution, are eliminated as a consequence of the higher symmetry. Even if atoms do change sublattices in order to accommodate stress, they would incur too high a penalty in internal energy to offset the release of strain energy. However, in off-stoichiometric alloys, substitutional disorder exists in the ordered phase, so to some extent a relaxation remains possible. The same is true for thermal disorder. Even if the order–disorder phase transition is of first order, the equilibrium long-range order parameter right below the transition temperature is less than unity, so some atoms stay on the opposite sublattice as this increases the entropy term of the free energy.

Thus, the accelerated decrease of the Zener peak in cooling occurs when ordering sets in. The volume fraction of ordered phase increases, and only contributions from the disordered domains (e.g. the silver-rich phase) as well as thermal disorder within the ordered domains remain. In heating, the process is reversed. However, the critical temperature at which the disordering process begins, appears to be higher than the ordering temperature in cooling. This hysteresis indicates a first-order phase transition. All these conclusions, and more, can be drawn from the frequency spectra of mechanical loss measured in isothermal conditions, which will be the main focus of chapter 4.

As point defects, i.e. single atoms, become mobile at the temperature of the Zener relaxation, one would expect the next peak in the spectrum to be caused by the collective motion of groups of atoms forming *linear* defects, such as dislocations. As it turns out, that is not the case. Chapter 5 will demonstrate that the second peak in the temperature spectrum, only about 120 K higher than the Zener peak, must be attributed to grain boundary sliding.

One of the main arguments for this assertion are comparative studies of monocrystals and polycrystals of identical composition. Figure 3.6 shows the spectra of monocrystalline and polycrystalline Au 518 plotted on the same graph. One striking difference is the absence of the high-temperature peak in the single crystal's spectrum, while the high-temperature background remains virtually unchanged. The background, as will be discussed at the end of chapter 5, is due to dislocations and increases with dislocation density.

On a side note, the reduced height of the Zener peak in the monocrystal may be attributed to the anisotropy of the Zener relaxation. In fact, the Zener relaxation strength depends strongly on the crystal's orientation.^[Po94] In a polycrystalline material, however, the contributions of the various grains average out.

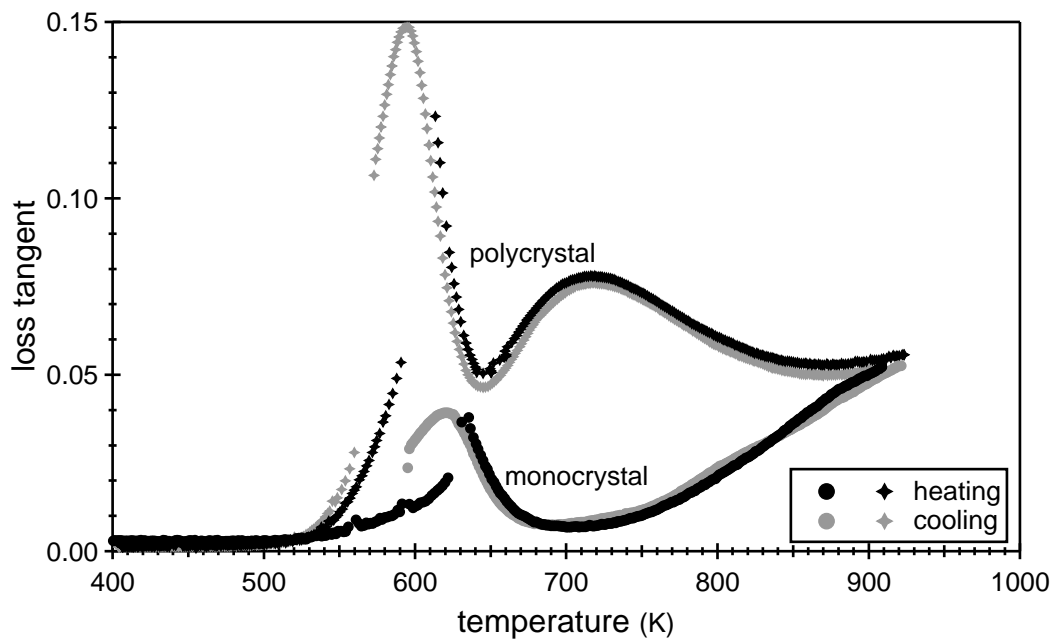


Figure 3.6: Temperature spectrum in heating and cooling (at 1 K/min and 0.5 Hz) of a monocrystalline Au 518 specimen, compared to the spectrum of a Au 518 polycrystal.

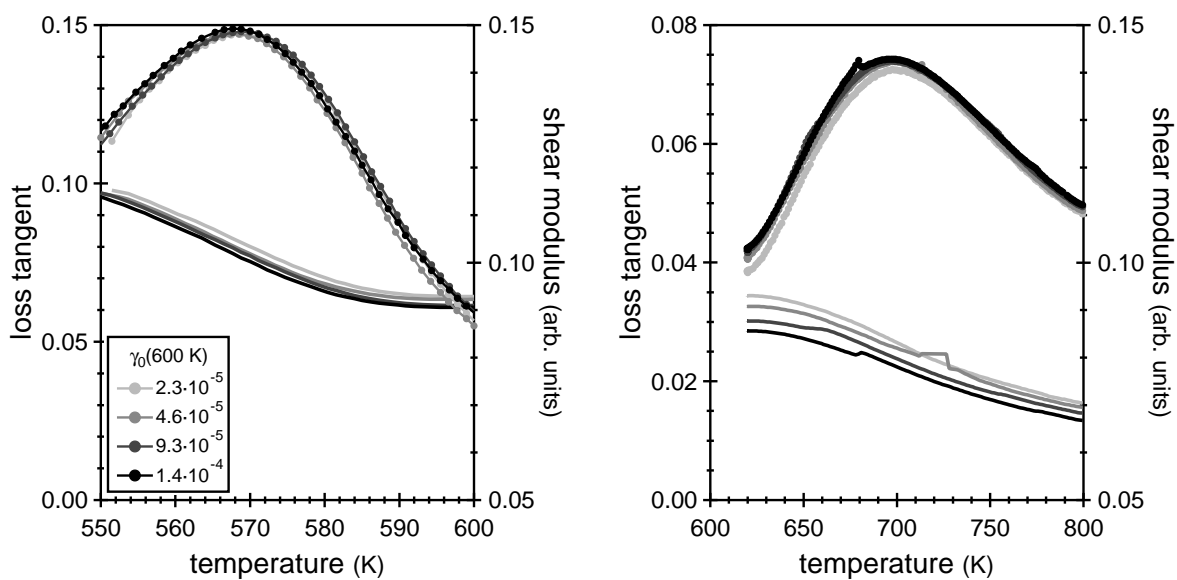


Figure 3.7: Strain amplitude dependence of the Zener peak (left) and the grain boundary peak (right) in Au 518.

Both, Zener and grain boundary relaxation, show little to no amplitude dependence, as evidenced by figure 3.7. Accordingly, they can be described within the scope of the linear response theory laid out in chapter 2, more precisely the viscous friction mechanism corresponding to a standard anelastic solid. Only the grain boundary peak decreases slightly at small amplitude. This indicates that some break-away mechanism (requiring a threshold stress) is at work, which would explain the non-linearity. However, this mechanism is not necessarily related to the peak itself — it may be due to the background, which increases with temperature.

The grain boundary peak hardly changes with alloy composition. In all spectra it appears at roughly the same temperature, between 700 K and 750 K. The peak's height is never less than 0.7 and never more than 0.8 (including the background). The peak is very broad, with β ranging from 3 in some alloys to 5 in others. Note that the Zener peak, with $\beta = 1.5$ for Au 518 (from fits to the spectra in figure 3.7), is not a perfect ($\beta = 0$) Debye peak either.

3.2 White Gold

At a fugitive first glance, the spectra of the white gold alloys, depicted in figures 3.8 through 3.12, do not resemble each other much. This comes as no surprise given their diversity in composition. Only a closer look reveals the recurring features.

Figure 3.8 shows the spectrum of Au 5125. It looks remarkably similar to the spectrum of Au 118 (figure 3.1), but shifted to higher temperatures. As it turns out, the same relaxation mechanisms as in yellow gold are at work.

The Zener peak now appears at roughly 700 K instead of 600 K. At 0.03, its height is virtually the same as in Au 218. With 21% compared to 22%, Au 218 and Au 5125 contain almost the same amount of copper. These observations indicate that copper atoms may again be responsible for the Zener relaxation, but their diffusion slows down in the presence of palladium.

However, this conclusion is somewhat contradicted, or rather weakened, by the fact that a Zener peak of similar height appears in the spectra of Au 5150 (figure 3.10), Au 8150 (figure 3.11) and Au 5210 (figure 3.12). The first two alloys contain little copper (9%), but in turn more than 10% iron which, being of similar atomic size, might have a comparable effect. Au 5210 contains no copper at all, though data from isothermal measurements presented in chapter 4 suggests that the relaxation is indeed of the Zener type, which would then stem from the Au–Pd alloy system. Unfortunately, no mechanical spectroscopy data for Au–Pd is available to this date. In any event, it seems safe to assert that, as opposed to yellow gold, the Zener relaxation in white gold cannot be understood as being due to the rearrangement of copper atoms alone.

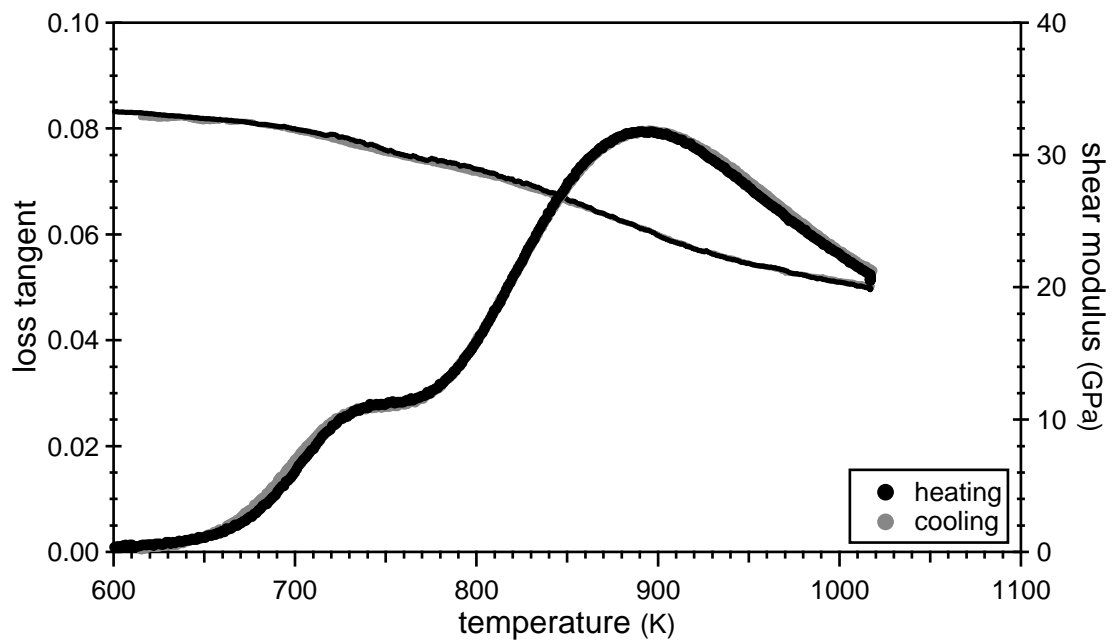


Figure 3.8: Mechanical loss spectrum of Au 5125 at 1 Hz excitation frequency and 2 K/min heating/cooling rate.

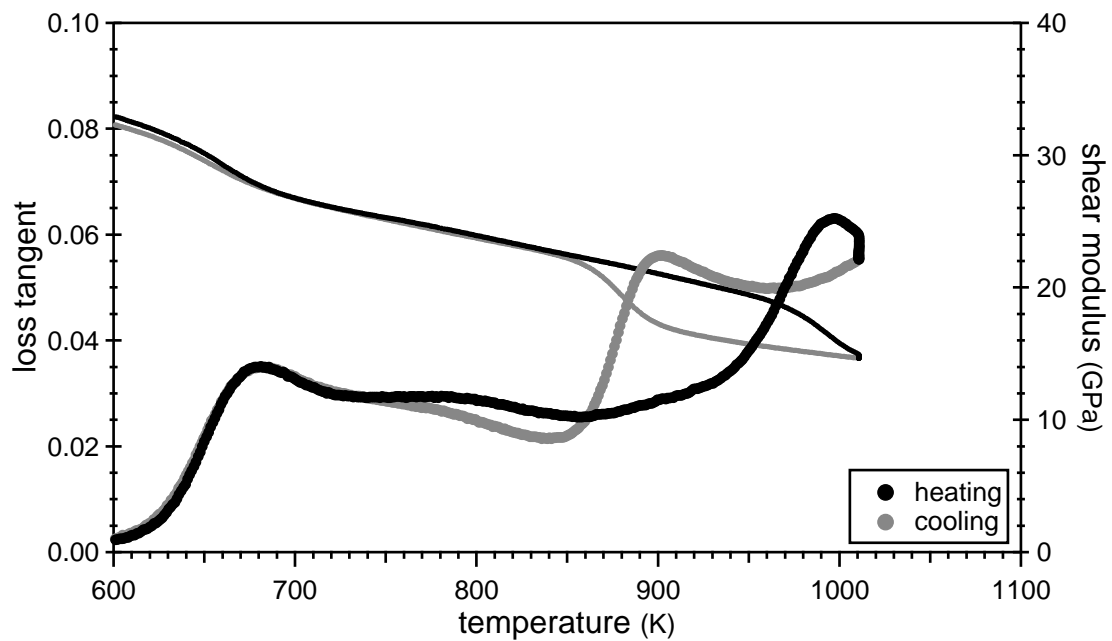


Figure 3.9: Mechanical loss spectrum of Au 5130 at 1 Hz excitation frequency and 2 K/min heating/cooling rate.

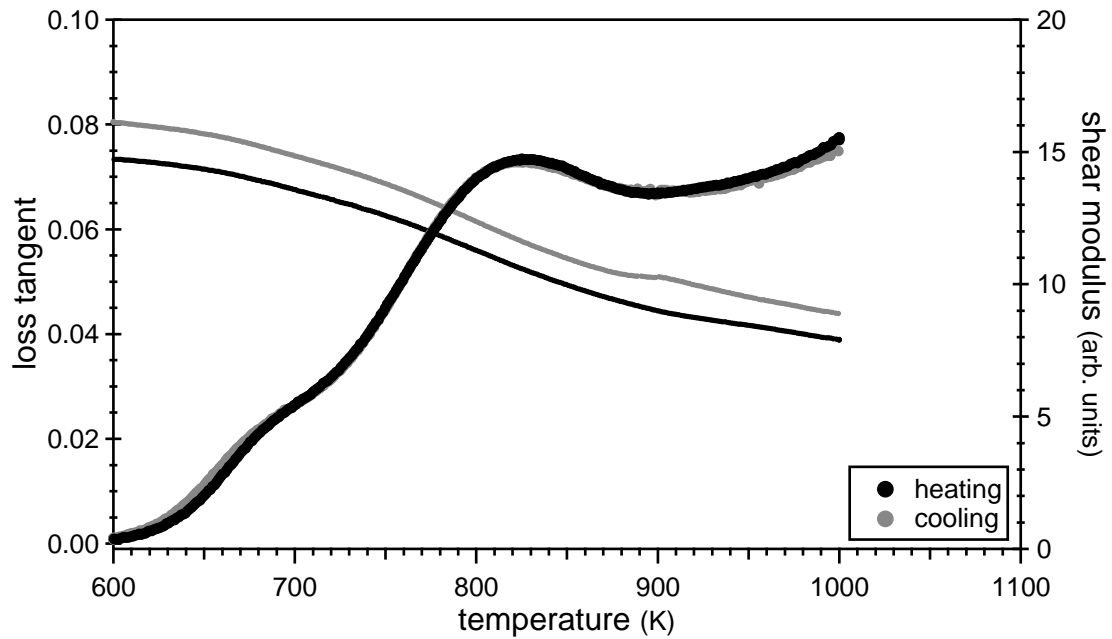


Figure 3.10: Mechanical loss spectrum of Au 5150 at 0.5 Hz excitation frequency and 1 K/min heating/cooling rate.

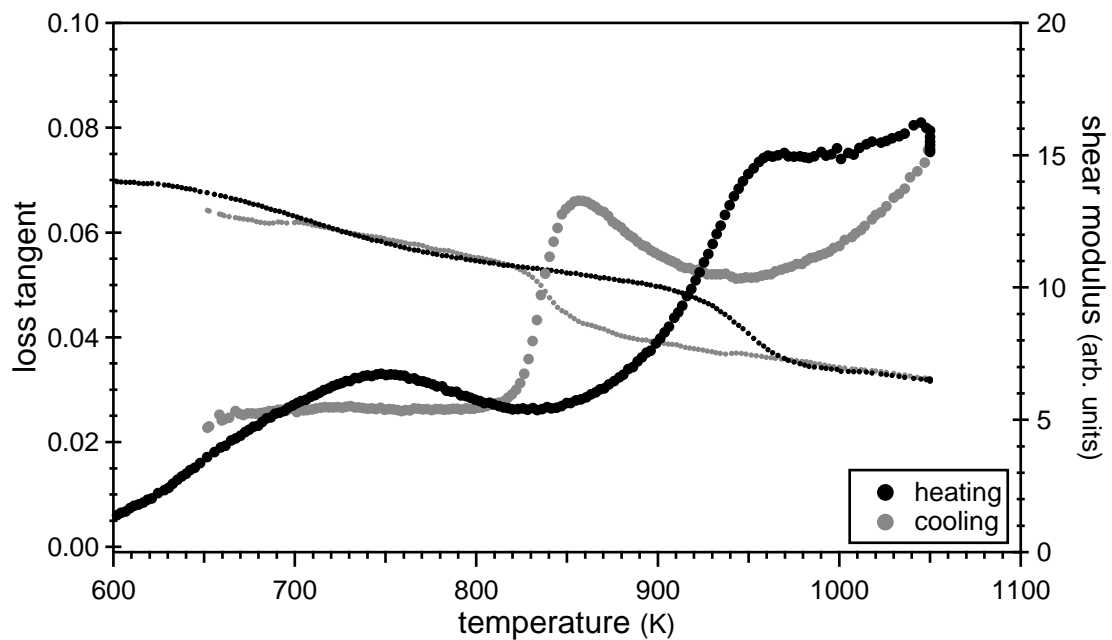


Figure 3.11: Mechanical loss spectrum of Au 8150 at 0.5 Hz excitation frequency and 2 K/min heating/cooling rate.

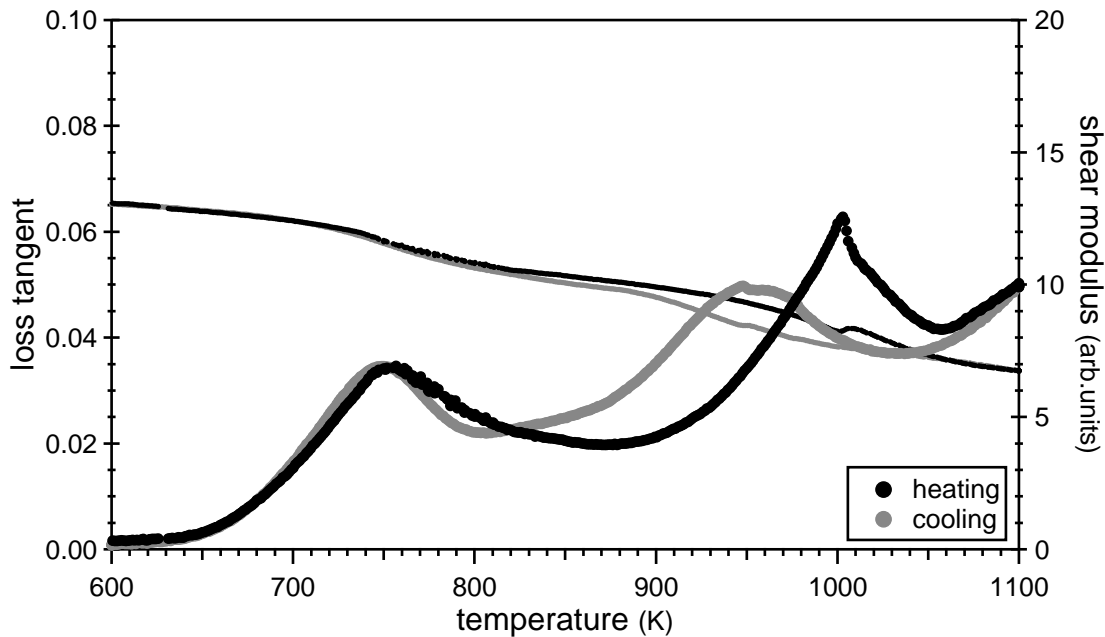


Figure 3.12: Mechanical loss spectrum of Au 5210 at 0.5 Hz excitation frequency and 2 K/min heating/cooling rate.

The Zener peak is again followed by the grain boundary peak, of comparable height ($F_0 = 0.08$ including the background) and broadening ($\beta \geq 3$) as in yellow gold. Hence, the different chemistry seems to have little influence on the strength of this relaxation. As the white gold's Zener peak tends to be situated higher in temperature, both peaks are often found closer to each other compared to yellow gold, such as in the spectrum of Au 5150 in figure 3.10. However, the position of the grain boundary peak does depend on a given sample's grain size, shifting to higher temperature for larger grains, as will be detailed in chapter 5.

Compared to Au 5125 and Au 5150, the spectra of Au 5130, Au 8150 and Au 5210 differ in one important aspect: the high-temperature regions all exhibit a strong hysteresis between heating and cooling. Incidentally, these and only these alloys contain indium and gallium additives. Chapter 5 will present convincing evidence that the following scenario occurs: As the alloy is cooled down from the solid solution, a second phase containing indium or gallium or both becomes thermodynamically stable and precipitates in the form of small particles. These particles pin the grain boundaries so that the grain boundary peak is cut off in cooling, when the particles precipitate, and mostly suppressed in heating until they are dissolved. The hysteresis observed between heating and cooling marks again a first-order phase transformation, associated this time with the precipitation and dissolution of the second phase.

Further proof for this interpretation is provided in figure 3.13. It shows the spectrum of Au 5130-1, a modification of Au 5130 that differs in that neither indium nor gallium were added to the melt.¹ The full grain boundary peak is now

¹This implies that the mass fractions of the remaining components increased slightly, elevating

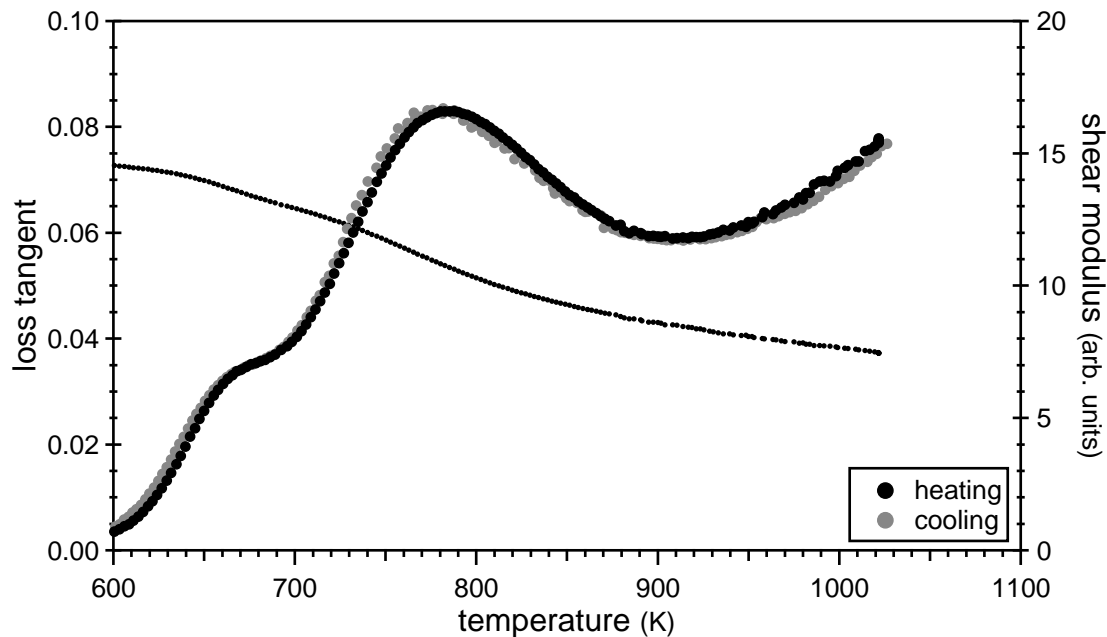


Figure 3.13: Mechanical loss spectrum at 0.5 Hz excitation frequency and 2 K/min heating/cooling rate of Au 5130-1, a modification of Au 5130 containing neither indium nor gallium.

observed, just like in Au 5125 (figure 3.8), and no hysteresis whatsoever.

In order to elucidate the role played by gallium on the one hand and indium on the other, two more modifications of Au 5130 and one modification of Au 5210 were produced: Au 5130-2 and Au 5210-2 only contain the indium part, Au 5130-3 only gallium. Results are shown in figures 3.14 and 3.15.

In Au 5130, precipitates form whenever either one of the two additives is present. However, in the gallium-free alloy Au 5130-2, the precipitation temperature is distinctly lower compared to Au 5130 and Au 5130-3, which both contain gallium. This could either indicate that the temperature of second-phase stability is extremely sensitive to the presence of gallium, or, much more likely, that two different types of particles form in the material. The formation of indium-rich particles, occurring at lower temperatures, would then be masked by the earlier precipitation of a gallium-rich phase.

In Au 5210-2, the characteristic hysteresis, due to the blocking of grain boundaries, is not observed. Hence, there is no evidence of a second phase. As Au 5210-2 (just like Au 5210) does not contain copper, one is thus lead to suspect that the indium-rich particles forming in the other white gold alloys must also be rich in copper, whereas the gallium-rich particles appear to be stable even without copper present.

The absence of the grain boundary peak in the single crystal's spectrum was verified for several white gold alloys. Figures 3.16, 3.17 and 3.18 show the results for Au 5130, Au 5130-1 and Au5210-2, respectively.

the caratage a little above 18.

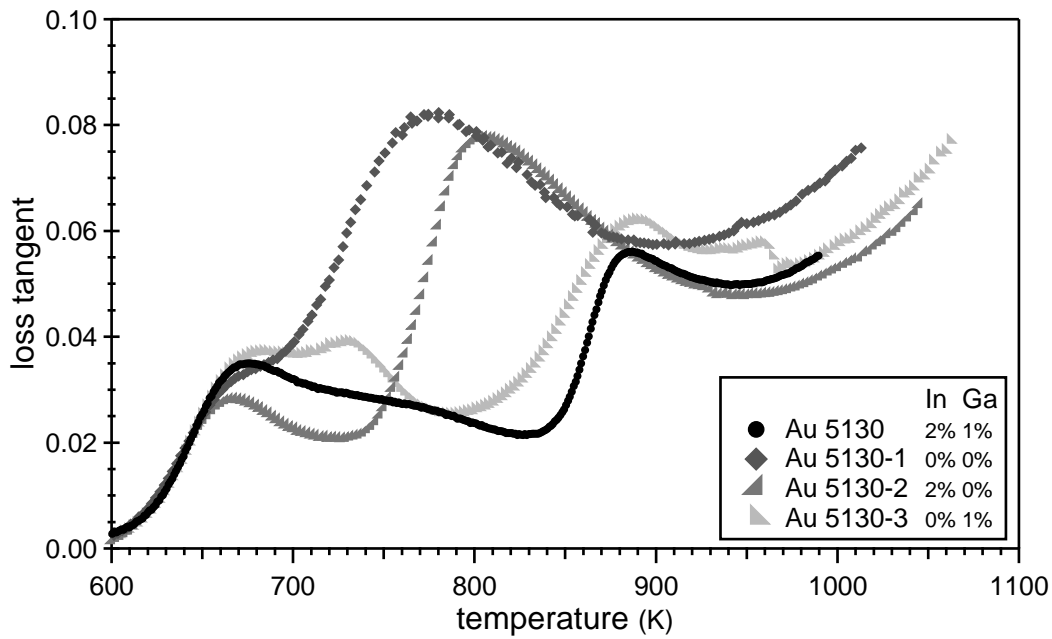


Figure 3.14: Mechanical loss spectra in cooling (at 2 K/min) of Au 5130 and its modifications (containing either no additives, or only indium, or only gallium) at 0.5 Hz (Au 5130-1, 5130-2, 5130-3) or 1 Hz (Au 5130) excitation frequency. To correct for the difference in excitation frequency as well as inaccuracies of the temperature calibration, the spectra were shifted in temperature until the Zener peaks' low-temperature flanks would overlap.

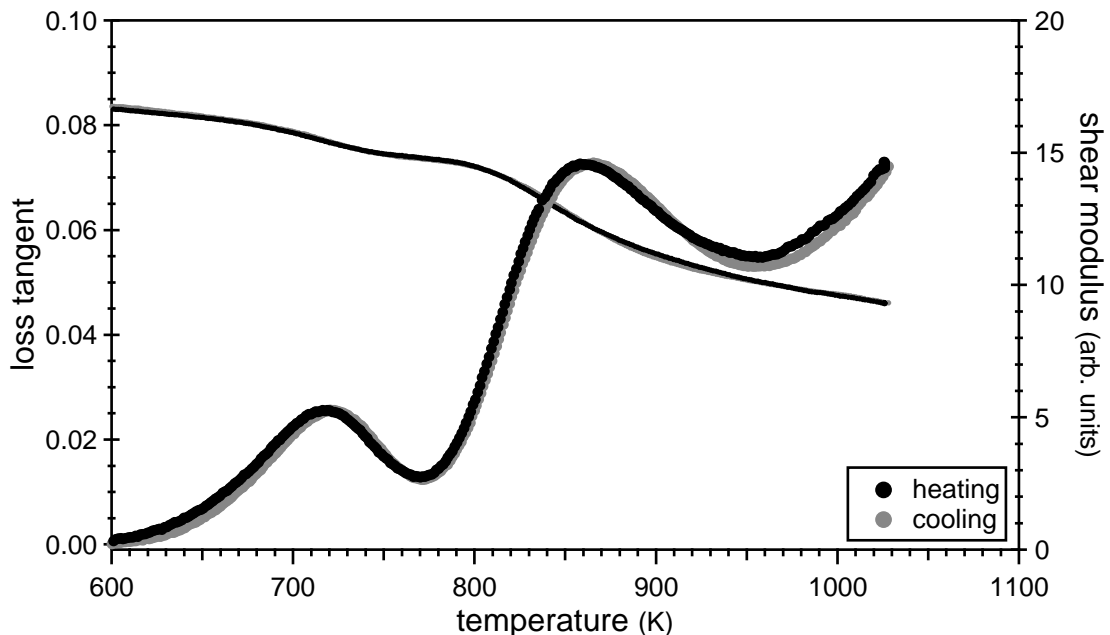


Figure 3.15: Mechanical loss spectrum (at 0.5 Hz excitation frequency and 1 K/min heating/cooling rate) of Au 5210-2, a modification of Au 5210 containing only indium, no gallium.

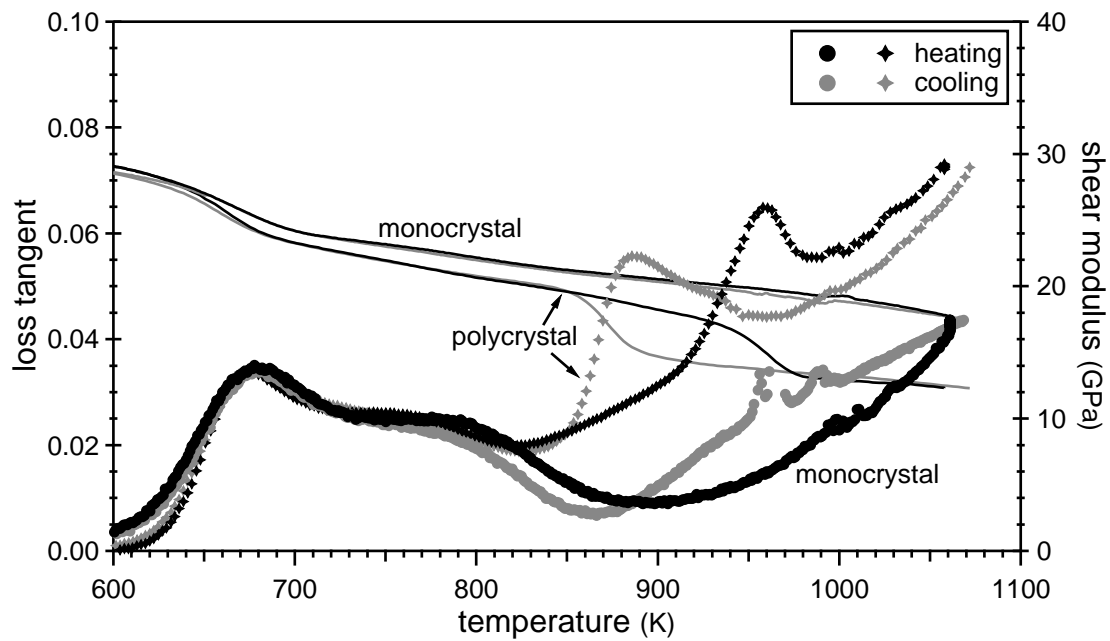


Figure 3.16: Mechanical loss spectra in heating and cooling (at 2 K/min and 0.5 Hz) of monocrystalline and polycrystalline Au 5130.

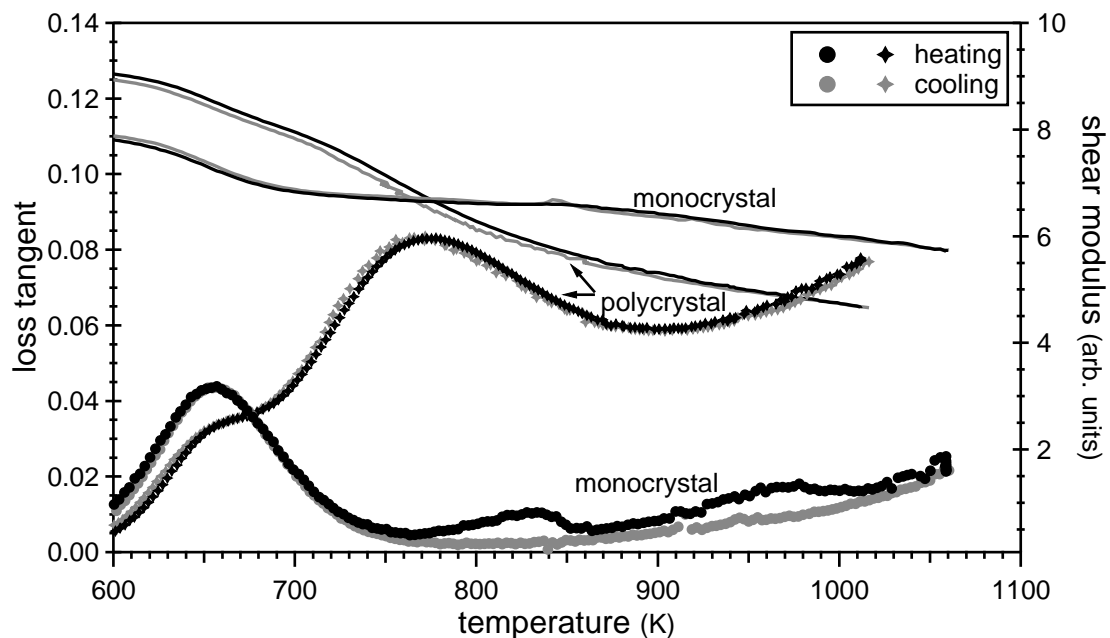


Figure 3.17: Mechanical loss spectra in heating and cooling (at 2 K/min and 0.5 Hz) of monocrystalline and polycrystalline Au 5130-1.

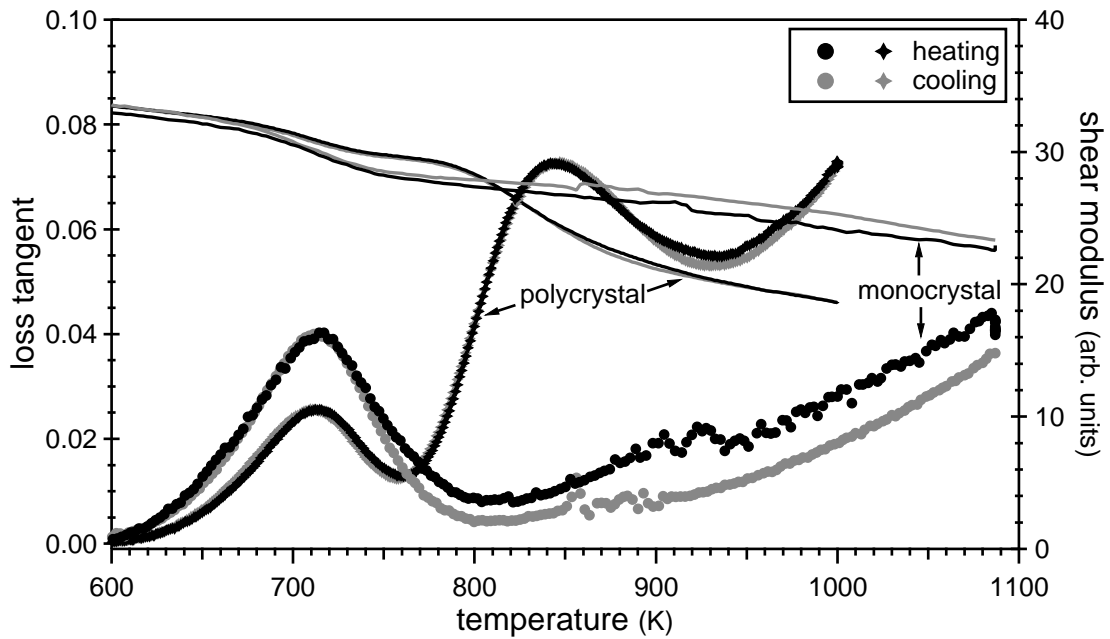


Figure 3.18: Mechanical loss spectra in heating and cooling (at 0.5 Hz excitation frequency) of monocrystalline and polycrystalline Au 5210-2.

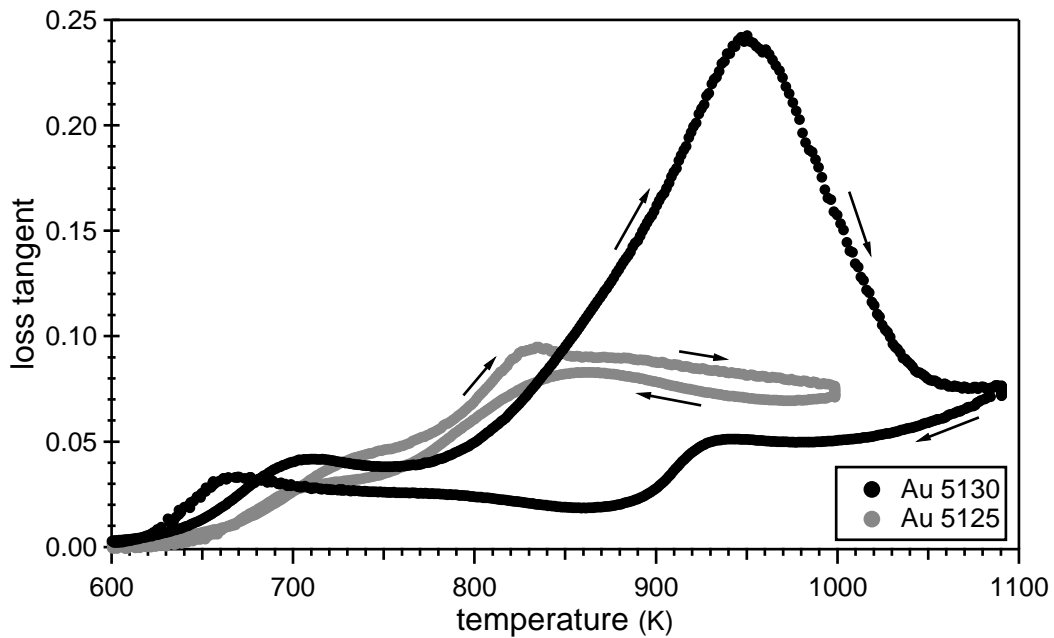


Figure 3.19: Mechanical loss spectra in heating and cooling (at 1 K/min and 0.5 Hz) of heavily cold-worked specimens (drawn to 75% deformation) of Au 5130 and Au 5125.

The optimal hardening temperatures of the hardenable white golds, as determined empirically, roughly coincide with the precipitation temperature. It is therefore fair to assume that the precipitates are also responsible for the age-hardening of these alloys. However, since hardness is measured at room temperature, the blocking of grain boundaries does not enter into account. The age-hardenability must be attributed to precipitates forming inside the grains as well, pinning dislocations and thereby increasing the alloy's yield stress.

In chapter 5 it will be argued that the high-temperature background appearing in all spectra is created by the motion of dislocations. Regarding this relaxation process, we can make another observation in figures 3.9 and 3.11: during annealing at the high-temperature end of the spectrum, the background decreases. All specimens showed such a behavior when exposed to sufficiently high temperature over extended periods of time. The background decrease is attributed to the mutual annihilation of dislocations of opposite sign, reducing the dislocation density.

The motion of dislocation also plays an important role during the recrystallization of heavily deformed material. Here, too, significant differences have been observed between white golds forming precipitates and those that do not. Figure 3.19 compares the spectra of heavily cold-worked specimens of Au 5125 (which contains no additives) and Au 5130. Both recrystallize during heating. The cooling curves correspond to the respective mechanical loss spectra presented earlier. The transient damping, which occurs during the recovery phase of the recrystallization process and therefore adds to the mechanical loss during heating, is much more pronounced in Au 5130 and subsides at higher temperatures. The alloy does not fully recrystallize until all precipitates are dissolved.

In Au 5130, and only in this alloy, a third peak is observed at medium temperature, above the Zener peak but below the grain boundary peak cut-off by precipitation (figure 3.9). Since it is an isolated feature, only little attention has been dedicated to this phenomenon. The peak is about as high as the Zener peak, but much broader ($\beta = 3.5$). Its origin is not clear so far. While it was tempting to think of it as the remnant grain boundary peak (after the precipitates have appeared, reduced its height and shifted its position to lower temperature), this possibility can be ruled out: the peak appears as well in the spectrum of monocrystalline Au 5130, where the grain boundary peak is absent (figure 3.16). The relaxation seems to require the presence of gallium, as it was not observed in any modification of Au 5130 produced without this additive. It is possible that it originates from the interaction of dislocations and precipitates.

Chapter 4

Zener Relaxation near Order-Disorder Transitions

This chapter will focus on the interplay of two rather different ordering phenomena occurring in yellow gold: stress-induced directional ordering, which causes the Zener relaxation, and long-range atomic ordering.

First, an analytic expression for the Zener relaxation strength is derived that accounts for the peak's breakdown upon atomic ordering in binary alloys. Then, frequency spectra (measured in isothermal conditions) of the binary Au–Cu alloy are analyzed in view of the model predictions. Experimental data of the ternary yellow gold are presented afterwards. Their spectra exhibiting the same characteristic features as the binary Au–Cu suggests these are due to ordering in the copper-rich phase. Disorder-to-order transition temperatures, marked by the breakdown of the Zener peak, are reported on a phase diagram. Furthermore, it will be demonstrated how the kinetics of the ordering process can be studied by mechanical spectroscopy in order to obtain predictions of the transformation times as a function of temperature. The chapter concludes with a discussion of the Zener relaxation in white gold.

4.1 Theory of the Zener relaxation

Several theories exist describing stress-induced ordering either as a reorientation of elastic dipoles formed by solute pairs^[Zen,No63], as directional order of (nearest-neighbor) bonds^[Le54], as variations in short-range order beyond nearest neighbors^[We67], or by a lattice gas model^[Wi96]. Experimentally, the primary interest lies in the fact that the Zener relaxation time is of the same order of magnitude as the time between atomic jumps, but can be measured at temperatures far below those accessible to radio-tracer diffusion experiments.^[No52]

In the previous chapter, it was argued that the size mismatch between alloying elements causes lattice distortions in the solid solution, such as those observed in Au–Cu by XAFS, and thus gives rise to a relaxation mechanism: stress-induced directional ordering of bonds. Historically, Clarence Zener first put forward such

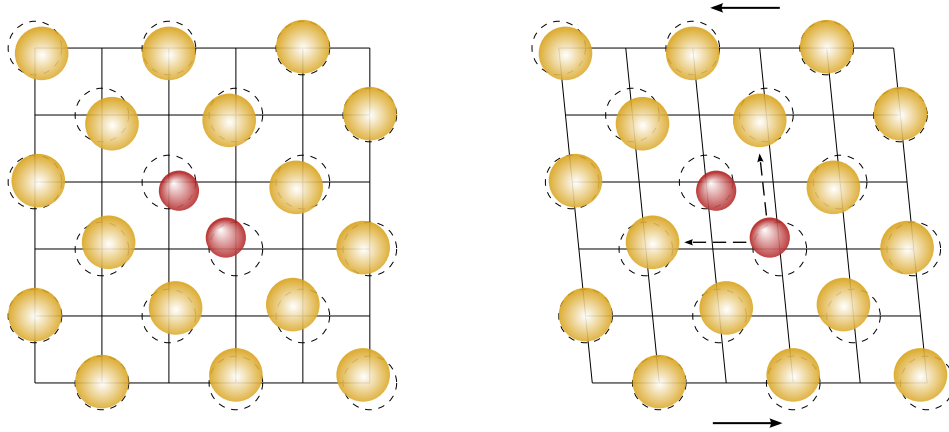


Figure 4.1: Schematic illustration of the Zener relaxation in dilute alloys: when a pair of undersized atoms in a $\{100\}$ plane locally distorts the f.c.c. lattice (left), an external stress will favor some sites over others (right).

reasoning to explain a mechanical loss peak he observed in an α -brass single crystal in 1942. Five years later, the same author proposed a theoretical model, attributing the effect to the reorientation of atomic pairs.^[Ze47] Since then, the phenomenon is known as Zener relaxation.

Zener's pair reorientation theory is valid for small concentrations of one of the two alloying elements. In the solid solution, a pair of solute atoms locally deforms the lattice of the surrounding solvent matrix and can therefore be thought of as a structural defect. Figure 4.1 illustrates the case of an undersized atomic pair in a $\{100\}$ plane of an f.c.c. lattice. The so-called λ -tensor, of components $\lambda_{ij}^{(p)}$ for a defect of orientation p , describes the *extra* local strain field the defect produces with respect to the matrix. For the atom pair in figure 4.1, the λ -tensor's principal axes are along $[\bar{1}10]$, $[110]$ and $[001]$. Generally, its three principal values are mutually different, $\lambda_1 \neq \lambda_2 \neq \lambda_3$, reflecting the defect's orthorhombic symmetry. There are six crystallographically equivalent orientations of the pair axis, two in each $\{100\}$ plane, so p runs from 1 to 6.

At zero stress, the pair orientation is random. But this symmetry is broken as soon as an external stress field comes into play. It will lower the free energy level of those orientations $\lambda^{(p)}$ that would relax the elastic strain, i.e. further increase it while the stress remains constant. Diffusion of one of the atoms forming the pair to a neighboring lattice site changes the orientation. Consequently, the relaxation time τ will be of the order of $\frac{a^2}{D}$, where a is the lattice parameter and D the diffusion coefficient.^[NB10]

Zener's pair reorientation model yields a relaxation strength proportional to $1/kT$.^[Ze47] The singularity at zero temperature is readily understood: At $T = 0$ the configurational entropy no longer plays a role and all dipoles would want to align at even infinitesimally small stresses to minimize energy. The relaxation strength, defined in equation (2.9) as the ratio of anelastic strain (which is finite) and elastic strain (infinitesimal), must therefore go to infinity.

Le Claire and Lomer, in 1954, criticized Zener's theory on several grounds.^[Le54] Most notably, they pointed out that it is not obvious how the reorientation illustrated in figure 4.1 produces a relaxation. In fact, as the pair rotates, if one counts the atomic bonds the pair forms in the $\{100\}$ plane, there are one like bond (B–B, the one between the two solute atoms) and two unlike bonds (A–B) in the crystal direction $[\bar{1}10]$ parallel to the pair, and four unlike bonds in the $[110]$ direction perpendicular to it. I.e., the net difference in total bond numbers (of the entire crystal) between the two orientations is two A–B bonds versus one B–B bond. The same is true for a rotation of the pair into one of the other (out-of-plane) orientations. Now, if the average bond length of the solid solution followed Vegard's law,

$$a_{A-B} = c_A a_A + c_B a_B, \quad (4.1)$$

there would be no dimensional change of the crystal as the pair rotates. In other words, the elastic dipole created by the pair, while *per se* orthorhombic in symmetry, would have degenerate principal values if Vegard's law was strictly obeyed.

Experimentally, Vegard's law was found true only for some ionic salts, but rarely for metallic systems.^[CH] However, we learn from the above remarks that the atom size mismatch in the solid solution, despite the intuitive appeal of imagining atoms as hard spheres of different atomic radii, does not by itself explain the Zener relaxation. It is rather the varying compressibility of the different kinds of bonds, and thus the deviation from Vegard's law, that accounts for the anisotropy of the elastic dipole.

In fact, a Zener relaxation peak has also been observed in Au–Ag,^[Tu60] though gold with 4.078 Å and silver with 4.086 Å have very similar lattice parameters. Furthermore, XAFS studies of Au–Ag could not reveal any significant deviations from a regular crystal lattice.^[Fr00] Nevertheless, the solid solution disobeys Vegard's law.^[AgAu] Hence, it may be argued that local lattice distortions are a sufficient, but not a necessary condition for stress-induced ordering.

Another major point of concern with Zener's theory is that the notion of an atomic pair representing an isolated structural defect loses all meaning if the solute concentration becomes significant. Particularly because the phenomenon is most often observed in concentrated solid solutions.^[NB10] Instead of atomic pairs, one is better advised to recur to bond numbers for the choice of the internal thermodynamic variable.

Long-range ordered alloys are not (or are a lot less) susceptible to stress-induced diffusion. Not only are they free of static lattice distortions if the order is perfect, but any bond reorientation would then incur the same energy penalty that stabilized the ordered structure in the first place. Stress-induced bond relaxation can only occur as long as some disorder is present, be it substitutional or thermal. Thus, in a stoichiometric alloy the Zener relaxation strength should go to zero

as the long-range order parameter reaches unity. At off-stoichiometric compositions the peak height may remain finite, but should drop off markedly compared to the solid solution.

Experimentally, this behavior was verified early on in a number of alloy systems, such as Mg–Cd that forms an ordered structure at composition MgCd_3 .^[Lu56] However, contemporary experimental methods, *temperature*-dependent mechanical loss measurements, made it difficult to study the Zener relaxation in conjunction with the order–disorder phase transition, and therefore never went beyond establishing the existence or absence of the peak for a given alloy composition. The evolution of the relaxation strength during the transition could never be followed first-hand. The next section of this chapter will present the first direct observation of the peak’s breakdown, in isothermal conditions, that is, in *frequency*-dependent mechanical loss spectra.

In a concentrated solid solution, long-range ordering may be regarded as being the result of a spontaneous self-alignment of bonds of the same kind. While, conceptually, this reasoning is certainly an oversimplification, the idea behind it is to point out the analogy to ferromagnetic materials, where the spontaneous alignment of permanent magnetic moments results in the formation of the ferromagnetic (ordered) phase. Moreover, in the (disordered) paramagnetic phase, the magnetization produced by an external magnetic field, i.e. the *partial* alignment of all spins, becomes increasingly stronger as one approaches the Curie temperature T_c . For many ferromagnets, the magnetic susceptibility has a singularity exactly at T_c , a fact expressed by the Curie–Weiss law:

$$\chi_m = \frac{C}{T - T_c}.$$

Strictly speaking, the term “law” is a misnomer. There are a number of ferromagnetic materials with a non-linear behavior of χ_m^{-1} in the vicinity of T_c .^[Moh]

Similarly, and contrary to the predictions of the Zener pair reorientation model, the Zener relaxation strength in many materials follows a Curie–Weiss type law:

$$\Delta = \frac{C}{T - T_c}. \quad (4.2)$$

Here T_c is the critical temperature of self-induced ordering.^[NB⁸] C shall be referred to as the anelastic Curie–Weiss constant.

The theory presented in the following paragraphs will start off from Le Claire and Lomer’s model^[Le54] for binary concentrated alloys, wherein the internal order parameters are the (like/unlike) bond numbers in different crystal directions, and then extend it by incorporating Li and Nowick’s approach^[Li61] that takes interaction of order parameters into account, thus yielding the observed Curie–Weiss type temperature dependence.

Let us consider a crystalline binary solid solution formed by mixing atoms of species A and B. Disregarding interactions beyond the nearest-neighbor shell

(and neglecting local lattice distortions), the total internal energy of the crystal can be expressed in terms of the numbers of unlike bonds N_{AB} (of type A-B or B-A) and like bonds N_{AA} and N_{BB} , as well as the corresponding bond energies V_{AB} , V_{AA} , V_{BB} :

$$U = N_{AA} V_{AA} + N_{BB} V_{BB} + N_{AB} V_{AB}. \quad (4.3)$$

The average bond energy

$$V = 2 V_{AB} - V_{AA} - V_{BB}$$

reflects the alloy's tendency to exhibit short-range order ($V < 0$), atom segregation ($V > 0$), or form a perfectly random solid solution ($V = 0$).

An external stress will break the assumed symmetry among the nearest neighbors. As the deformation of the crystal stretches the interatomic spacing in some directions and shortens it in others, the bond energies, which vary with bond length, will now depend on the crystallographic direction p , i.e.

$$V^p = 2 V_{AB}^p - V_{AA}^p - V_{BB}^p. \quad (4.4)$$

p runs again from 1 to $\frac{z}{2}$, where z is the coordination number of nearest neighbors.

Each of the crystal's N atoms forms $\frac{z}{2}$ bonds (per atom). The bonds of all N_A A-atoms are either of the A-A or A-B type, while the N_B B-atoms form only B-B or A-B bonds. This can be expressed as:

$$\begin{aligned} N_{AA} + \frac{1}{2} N_{AB} &= \frac{z}{2} N_A, \\ N_{BB} + \frac{1}{2} N_{AB} &= \frac{z}{2} N_B. \end{aligned}$$

Similar relations hold if one distinguishes bonds oriented in different crystallographic directions p . Per atom and p , there is only one of such bonds:

$$\begin{aligned} N_{AA}^p + \frac{1}{2} N_{AB}^p &= N_A, \\ N_{BB}^p + \frac{1}{2} N_{AB}^p &= N_B. \end{aligned} \quad (4.5)$$

It follows that, as long as the particle numbers N_A and N_B (on the right-hand side) are constant, any change in bond numbers — which may reposition any number of atoms — must satisfy:

$$\Delta N_{AA}^p = \Delta N_{BB}^p = -\frac{1}{2} \Delta N_{AB}^p.$$

Particularly, as pointed out in the above discussion of the atom pair reorientation with respect to Vegard's law, any B-B bond that rotates will be replaced by two

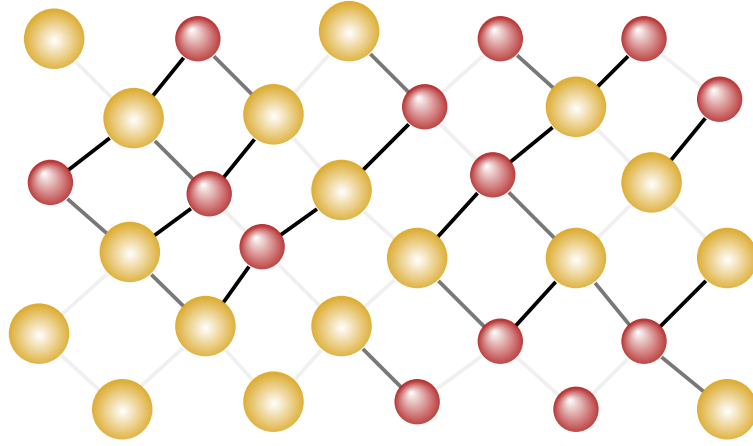


Figure 4.2: Illustration of the count of unlike bonds, N_{AB}^p , along (two) different crystallographic directions p .

A–B bonds in its original direction (while an A–A bond rotates along with it). This dissociation of like bonds resembles a reversible chemical reaction:



To preserve the problem's symmetry with respect to the two atom species A and B, it is best to parametrize in terms of the following order parameter:

$$y^p = \frac{\frac{1}{2}N_{AB}^p}{N} \quad (0 \leq y^p \leq \min\{c_A, c_B\}). \quad (4.7)$$

Its range is limited by the smaller of the two atom fractions, $c_A = \frac{N_A}{N}$ or $c_B = \frac{N_B}{N}$.

Thanks to the bond number restrictions (4.5), the total energy of the crystal, equation (4.3), can now be written as

$$U = N \sum_p (c_A V_{AA}^p + c_B V_{BB}^p + y^p V^p), \quad (4.8)$$

where only the last term, the mixing enthalpy, depends on the order parameters.

As for the free energy, $F = U - TS$, one neglects all but the configurational entropy:

$$S = k \ln \Omega(\{y^p\}),$$

where $\Omega(\{y^p\})$ means the number of possible arrangements of all atoms sharing the specified set of order parameters. A numerical approximation for Ω and minimizing the free energy,

$$\frac{\partial F}{\partial y^p} = 0,$$

leads to the equilibrium condition^[Le54, Li49]

$$\frac{(c_A - y^p)(c_B - y^p)}{(y^p)^2} = \exp\left(\frac{V^p}{kT}\right). \quad (4.9)$$

A formal application of the law of mass action to the bond “reaction” (4.6) would have given the same result.^[Haa] Equation (4.9) is therefore known as the quasi-chemical approach to a solid solution’s equilibrium state of short-range order. For $T \rightarrow \infty$, or if $V^p = 0$ at any temperature, the equilibrium condition yields bond numbers corresponding to a perfectly random distribution of atoms:

$$\frac{N_{AA}^p}{N} = c_A^2, \quad \frac{N_{AB}^p}{N} = 2 c_A c_B, \quad \frac{N_{BB}^p}{N} = c_B^2. \quad (4.10)$$

At zero stress, and as long as there is no long-range order, equilibrium order parameter and bond energy must be independent of p :

$$y^p|_{\sigma=0} = y_0 \quad \text{and} \quad V^p|_{\sigma=0} = V_0.$$

Expanding the left-hand (l.h.s.) and right-hand side (r.h.s.) of the equilibrium condition (4.9) into Taylor series around their respective equilibrium values, and equating the two linear terms,

$$\frac{d}{dy^p} (\text{l.h.s.}) \Big|_{y_0} \Delta y^p = \frac{d}{dV^p} (\text{r.h.s.}) \Big|_{V_0} \Delta V^p,$$

yields a relation between Δy^p and ΔV^p , the first-order stress-induced deviations from equilibrium. One finds:

$$\Delta y^p = -g(y_0) c_A^2 c_B^2 \frac{\Delta V^p}{kT}, \quad (4.11)$$

where

$$g(y_0) = \frac{(c_A - y_0) y_0 (c_B - y_0)}{c_A^2 c_B^2 (2c_A c_B - y_0)} \quad (4.12)$$

is a function depending only on the initial state of order y_0 . It is plotted in figure 4.3.

We have yet to find an equilibrium condition at finite stress, i.e. an expression that fixes either ΔV^p or Δy^p . To that end, consider first the effect on the total strain at constant temperature:

$$\epsilon = \epsilon_{\text{el}} + \epsilon_{\text{an}} = J_u \sigma + \sum_p \lambda_p \Delta y^p. \quad (4.13)$$

Here the anelastic strain is expressed in terms of coefficients

$$\lambda_p = \frac{\partial \epsilon}{\partial y^p} \Big|_{T, \sigma, y^q \neq p} \quad (4.14)$$

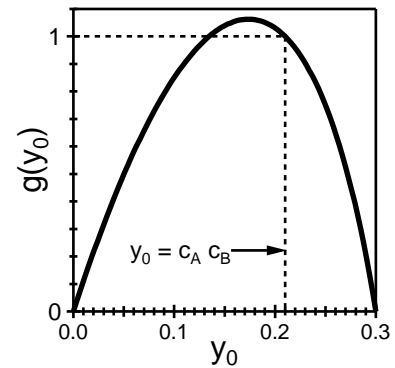


Figure 4.3: Plot of the function $g(y_0)$, equation (4.12), for $c_A = 0.3$ (or $c_B = 0.3$).

that relate the changes in short-range order to the strain relaxation that ensues. They hail from atomistic properties such as the different bonds' compressibilities. Note that for single crystals, due to their anisotropy, the effective strain relaxation and thus λ^p depend on the mode of deformation and the crystal's orientation. In this treatment the coefficients will be taken as parameters.

On the other hand, learning from expression (4.8) of the internal energy that y^p and V^p are conjugate thermodynamic variables, we can write down the differential of the Gibbs free enthalpy, $G = U - TS - V\sigma\epsilon$ (where V denotes the undeformed crystal's volume), at constant temperature ($dT = 0$) for the state under stress:

$$dG = N \sum_p V^p dy^p - V \epsilon d\sigma.$$

From the reciprocity relation

$$N \left. \frac{\partial V^p}{\partial \sigma} \right|_{T, y^p} = -V \left. \frac{\partial \epsilon}{\partial y^p} \right|_{T, \sigma, y^q \neq p}$$

we find, using (4.13), that

$$\left. \frac{\partial V^p}{\partial \sigma} \right|_{T, y^p} = -v \lambda_p,$$

where $v = \frac{V}{N}$. This means that V^p varies linearly with σ . For the finite-stress equilibrium one can therefore make the reasonable ansatz:^[Li61]

$$\Delta V^p = -v \lambda_p \sigma - \sum_q b_{pq} \Delta y^q. \quad (4.15)$$

The first term accounts for the direct stress-induced variation of the bond energies, the second for repercussions of the ensuing change in the state of order.

The interaction coefficients b_{pq} complicate the solution of the problem as they couple ΔV^p and Δy^q corresponding to different bond orientations p and q . We will therefore disregard all non-diagonal terms. All diagonal terms must be equal for symmetry reasons, as they refer to equivalent crystallographic directions. Thus: $b_{pq} = b \delta_{pq}$. Physically, the one remaining parameter b describes the *average* additional gain in bond energy due to the stress-induced change in local order. As such, the decoupling of the interaction terms corresponds to a mean-field approximation. Note, again, that for single crystals b is anisotropic.

Using (4.11) in (4.15), we can now solve for the stress-induced deviations of the bond energies:

$$\Delta V^p = -v \lambda_p \sigma \frac{T}{T - T_c}. \quad (4.16)$$

The critical temperature of self-induced ordering turns out to be:

$$k T_c = b g(y_0) c_A^2 c_B^2. \quad (4.17)$$

The relaxation strength, defined in (2.9) as the ratio of anelastic and elastic strain, can now be calculated for the Zener relaxation. Starting from equation (4.13) and using (4.11), then (4.16), one finds:

$$\Delta = \frac{c_A^2 c_B^2}{k(T - T_c)} v M_u \sum_p g(y_0) \lambda_p^2, \quad (4.18)$$

where $M_u = J_u^{-1}$ denotes the unrelaxed elastic modulus corresponding to the applied mode of deformation (the shear modulus for a polycrystalline sample measured in a torsion pendulum). The relaxation strength exhibits a temperature dependence of the Curie–Weiss type, equation (4.2). The anelastic Curie–Weiss constant

$$C = c_A^2 c_B^2 \frac{v}{k} M_u \sum_p g(y_0) \lambda_p^2 \quad (4.19)$$

is symmetric in the concentrations of constituents A and B.

The singularities at T_c , that both the bond energies ΔV^p as well as the relaxation strength Δ present, should be interpreted in view of the equilibrium condition provided by the quasi-chemical approach, equation (4.9): V^p approaching plus or minus infinity means that y^p takes on one of its extreme values, i.e. either 0 or $\min\{c_A, c_B\}$ depending on p and the sign of ΔV^p . This maximization of short-range order can be understood as the formation of a long-range ordered structure (particularly at $c_A = c_B = \frac{1}{2}$, where it is the only possibility). Thus, at T_c , the alloy would spontaneously order, even at infinitesimally small stresses.

In practice, the singularity at T_c is never reached. It is always preceded by atomic ordering, at $T_o > T_c$. The model, as described above, does not account for this experimental fact since it only deals with short-range order in the a priori disordered phase. However, no proof was provided that the thermal equilibrium of the quasi-chemical approach, which was the starting point of the derivation, is actually stable. The model prediction that at T_c , at least for stoichiometric compositions, the spontaneous ordering leads to a final state of *zero* configurational entropy, is a strong indicator that at this temperature the disordered phase had been unstable to begin with, and thus $T_o > T_c$.

Conversely, if the ordered phase is in fact stable, then the zero-stress equilibrium values become p -dependent, $y_0 \rightarrow y_0^p$, and so does the function g from equation (4.12) which depends on y_0^p . As typeset with foresight in (4.18), $g(y_0^p)$ must then remain under the sum sign (over p) in that equation.

In a random solid solution, where $y_0 = c_A c_B$ according to (4.10), $g(y_0)$ yields the value 1. In a long-range ordered structure such as AuCu I, however, it is zero for all p : see figure 1.6 on page 10 for illustration and note that y_0^p is either 0 (only like bonds) or $\frac{1}{2}$ (only unlike bonds) depending on p , and that the function g , plotted in figure 4.3, is zero in both cases.

For the more complicated structure of AuCu II, the result should be virtually the same. While the anti-phase boundaries introduce a certain amount of disorder^[Bo99], they are not expected to contribute measurably to stress-induced relaxation since that would involve a collective motion of atoms, not just isolated jumps.

In conclusion, the model presented here predicts a Zener peak of relaxation strength given by equation (4.18) that, while in the disordered solid solution, shows an increase of the Curie–Weiss type (4.2) towards a critical temperature T_c . Upon atomic ordering below T_o , the peak disappears or, at off-stoichiometric compositions, decreases markedly. The relaxation strength depends like $c_A^2 c_B^2$ on the compositions of the constituents.

4.2 Zener peak in Au–Cu

In a first step, we have investigated the Zener relaxation in the binary Au–Cu. The gold–copper system is a classic example for atomic ordering in alloys and a popular testing ground for theories predicting alloy phase stability.^[Oz98]

In an effort to also obtain kinematic data (relaxation times) of the ordered phase, an off-stoichiometric composition was chosen with Au_{57%}Cu_{43%} so that, thanks to configurational disorder, a measurable Zener peak would remain even in the long-range ordered state. According to the experimental phase diagram^[AuCu], Au_{57%}Cu_{43%} should undergo the $\alpha \rightarrow$ AuCu II disorder–order phase transformation at $T_o = 634$ K.

Mechanical spectroscopy was performed in the forced, low-frequency, inverted torsion pendulum described in chapter 2. Measurements were carried out under a helium atmosphere (7 mbar) on a polycrystalline, cylindrical specimen (22 mm in length and 2.5 mm in diameter). The specimen was produced from 5N-pure gold and copper, melted together and cast in a graphite crucible inside the same induction furnace used for the growth of single crystals and described in section 2.5, though in this case the crucible was cooled quickly and as a whole in an effort to obtain a multi-grained microstructure.

Figure 4.4 shows isothermal frequency spectra of the mechanical loss tangent at selected temperatures around the atomic order–disorder transition. From one frequency scan to the next, the temperature was increased (figure 4.4a) or decreased (figure 4.4b) in steps of 5 K.

Initially, i.e. at 610 K in figure 4.4a, the alloy is ordered — a result from a previous thermal treatment. Nevertheless, a small Zener relaxation peak appears in the spectrum. This indicates that the state of atomic order is not perfect, as intended. In the equiatomic AuCu this peak would be absent, unless the temperature were so close to T_o that thermal disorder becomes significant.

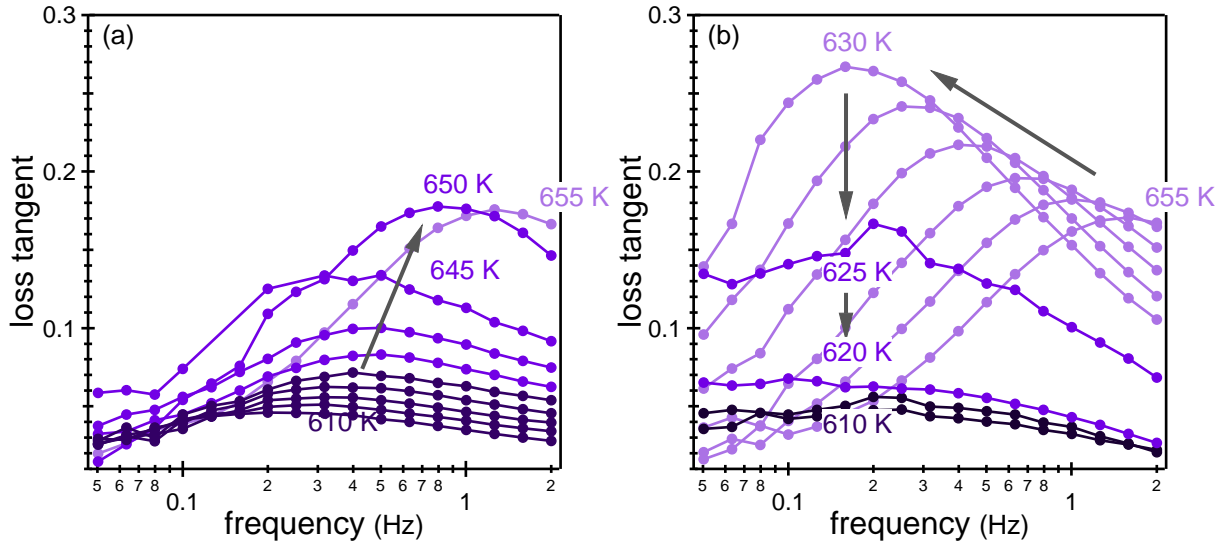


Figure 4.4: Mechanical loss frequency spectra of Au_{57%}Cu_{43%} in isothermal conditions at selected temperatures (steps of 5 K between curves) below and above the order-disorder phase transition. (a) Formation of the Zener relaxation peak with increasing temperature. (b) Critical evolution of the Zener relaxation peak height with decreasing temperature in the disordered α -AuCu phase (light shade), breakdown of the peak during the phase transformation (medium shade) to the ordered AuCu II phase (dark shade).

The relaxation time of stress-induced ordering in the ordered phase, as obtained from the Zener peak's position in all the frequency spectra up to 640 K, is plotted in figure 4.5 as a function of temperature. Fitting of $\tau(T)$ to the Arrhenius equation (2.14) yields a limit relaxation time $\tau_0^{(o)} = 3.6 \cdot 10^{-9}$ s and an activation enthalpy $H_{\text{act}}^{(o)} = 1.00$ eV for AuCu II.

Due to the decrease of the relaxation time with increasing temperature, the Zener peak shifts to the right in figure 4.4a. At the same time, the peak grows in height: slowly at first, reflecting the gradual decline of long-range order due to thermal disorder, then, between 640 K and 650 K, much more rapidly, which marks the transition from the now unstable AuCu II phase to the stable solid solution.

The temperature dependence of the Zener relaxation in the disordered phase is observed in figure 4.4b. The relaxation strength Δ , obtained from the peak height as per equation (2.12), follows, to a good approximation, a Curie-Weiss type law. This can be observed in figure 4.6 and is in agreement with the model prediction, equation (4.18). Extrapolation of the fit to the data points yields a critical temperature of self-induced ordering of $T_c = 596 \pm 5$ K.

As it turns out, the peaks are slightly broadened ($\beta \approx 1$). This detail was overlooked in the evaluation of the relaxation strength for figure 4.6, but would not change the determination of T_c as it only introduces a constant factor.

In the disordered phase, the relaxation time also obeys the Arrhenius equation (2.14), but the activation parameters are different. The curve is plotted on figure 4.5 along with the one for the ordered phase. There is a noticeable change

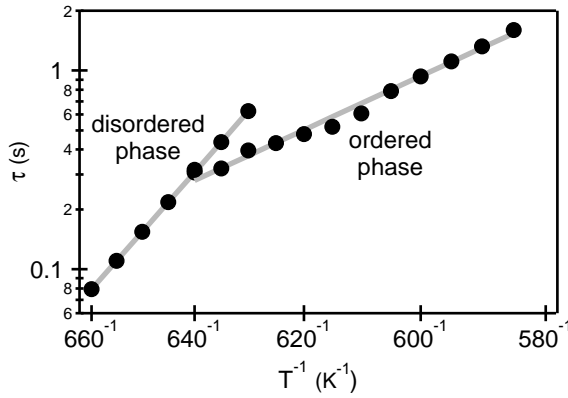


Figure 4.5: Relaxation time of stress-induced diffusion τ vs. inverse temperature in the disordered and ordered phase, along with separate fits to the Arrhenius equation (2.14).

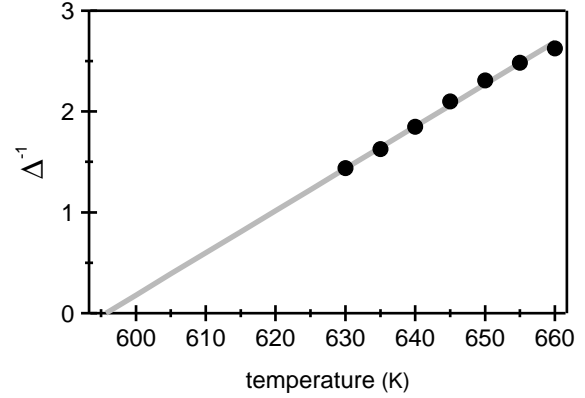


Figure 4.6: Curie-Weiss type behavior of the relaxation strength of stress-induced ordering, $\Delta^{-1} \propto T - T_c$, as obtained from the evolution the Zener peak's height in the disordered phase.

in slope at the phase transition. It means that diffusion in the ordered phase is actually faster than the trend of the disordered phase would let expect. For limit relaxation time and activation enthalpy in the disordered phase one finds $\tau_0^{(d)} = 1.2 \cdot 10^{-20}$ s and $H_{\text{act}}^{(d)} = 2.47$ eV. This activation enthalpy is two and a half times higher than in the ordered phase, while $\tau_0^{(d)}$ is suspiciously small. No definitive explanation can be offered at this point. It seems likely though, that the fluctuations in short-range order near the critical point play an important role. Also, as pointed out in the discussion of equation (2.15) in section 2.1 (page 25), the entropy difference involved in thermal activation may not always be neglected, even less so in the vicinity of a first-order phase transition where the equilibrium-state entropy incurs a discontinuous jump while the entire structure evolves. Note that the thermodynamical description of the activated state^[Go98] is rather complicated, since this state is per se out of equilibrium.

Upon cooling below 630 K (again in figure 4.4b), the Zener relaxation peak breaks down. This marks the onset of atomic ordering, which hinders stress-induced ordering except for the contribution due to substitutional disorder in the ordered phase. Contrary to earlier mechanical spectroscopy studies, the isothermal measurements presented in figure 4.4 are the first direct observation of the Zener peak's breakdown during atomic ordering.

Obviously, the disordered α -phase is unstable at 630 K and below, so this temperature represents a lower bound for the equilibrium critical temperatures of atomic ordering, T_o , though both temperatures should be very close. In the following section we will see how to improve this first and simple determination of T_o .

The hysteresis between heating and cooling observed in figure 4.4 clearly indicates that the phase transformation is of first order: the initial phase first becomes metastable and additional overheating or undercooling is required to render it thermodynamically unstable. After that, the transformation proceeds

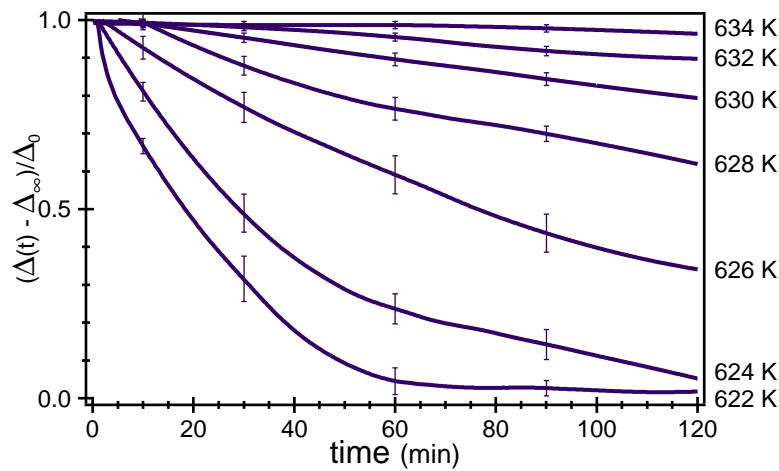


Figure 4.7: Kinetics of the disorder–order transformation as obtained from (normalized) mechanical loss measurements over time, at 1 Hz, after quick cooling of the disordered specimen to temperatures below T_0 .

much more rapidly, only limited by the energy barrier of atomic diffusion. This conclusion, that the AuCu II \rightarrow α phase transition is of first order, agrees with calorimetry studies showing that the transformation is associated with a latent heat. ^[Fe99, Ba01]

4.3 Kinetics of atomic ordering

The kinetics of the ordering processes in Au–Cu have been studied by several authors, using indicators such as the elastic modulus ^[Si40] and the electrical resistivity ^[Di51, Ku55], or observing the evolution of the X-ray diffraction patterns ^[OB59, Fe99] as a function of annealing time and annealing temperature. Furthermore, in-situ temperature observations per transmission electron microscopy have shown that AuCu II grows in the α -phase starting from needle-shaped nuclei. ^[Bo99]

The gradual breakdown of the Zener peak below the transition temperature can, too, be used to study the kinetics of the ordering process (figure 4.7). To that end, the specimen was first annealed in the disordered state at 680 K for one hour, then quickly cooled below the order–disorder transition temperature T_0 . After reaching the target temperature, the mechanical loss was monitored over time at a fixed frequency. The evolution of the state of long-range order is reflected in the mechanical loss dropping from an initial value, due to stress-induced diffusion in the still disordered phase, down to the infinite-time value corresponding to maximum atomic order, i.e. the state corresponding to the *equilibrium* long-range order parameter at that temperature. (For temperatures where ordering is slow, the final value was obtained after establishing order at a lower temperature and subsequent reheating.) We will assume that there is a correspondence between this *relative* relaxation strength and the volume fraction of the disordered phase. The assumption implies that the ordered phase nucleates and grows within the disordered phase.

In figure 4.7, the relative relaxation strength is reported as a function of annealing time. It should be noted that the curves were smoothed to improve the presentation. The scatter in the data during the phase transformation, indicated by error bars in figure 4.7 and also noticeable in the frequency spectra (figure 4.4), is caused by a shape memory effect that happens to occur in this particular alloy^[Oh98], hampering precision measurements.

In figure 4.7 one observes that the stronger the undercooling, the faster the ordering process. This presents further evidence that the phase transition is first order in nature. At 634 K, on the other hand, ordering slows down drastically and one readily estimates an equilibrium transition temperature of $T_o = 635 \pm 1$ K.

This result can be corroborated by modeling the kinetics of the ordering process. For the present alloy, Šíma's model for equiatomic AuCu seems promising, as it has proven to agree very well with experimental data, such as differential calorimetry, X-ray diffraction and resistivity measurements.^[Si02]

It was noted by that author that the ordering in AuCu does not proceed according to the classical Avrami equation for nucleation and growth processes. Instead, the volume fraction of ordered domains, f , evolves as a simple exponential: $f \propto 1 - \exp^{-Kt}$. Fits to the drop-off of the relative Zener relaxation strength during disordering, figure 4.7, confirm this observation for the present Au_{57%}Cu_{43%} alloy. Obviously f then obeys a rate equation. We therefore suppose:

$$\dot{f} = -K^{(d)}f + K^{(o)}(1 - f), \quad (4.20)$$

with rate parameters of ordering (o) and disordering (d) given as

$$K^{(o/d)} = \nu_0^{(d/o)} \exp\left(-\frac{H_{\text{act}}^{(d/o)}}{kT}\right) \exp\left(-\frac{F^{(o/d)}}{kT}\right). \quad (4.21)$$

$F^{(o)}$ and $F^{(d)}$ denote the free energy barriers for ordering and disordering, respectively. They reflect the fact that, in order to pass from the meta-stable to the stable phase (or even in the other direction), the alloy must go through atom configurations that are even higher in energy. These energy barriers will be determined from the fitting procedure that follows.

All configurational changes hinge on the diffusional process of atoms switching lattice sites with nearest neighbors. The other exponential factor appearing in expression (4.21) for the rate parameters is therefore nothing but the activation energy of atomic diffusion. In a slight variation of Šíma's approach, we distinguish here diffusion within the ordered and the disordered phase. Note that diffusion within the *ordered* phase enters the rate parameter of *disordering* and vice versa.

An advantage of using the Zener relaxation strength as an indicator for long-range order is that it readily provides diffusion data as well. We can now use the results for $\tau^{(o)}$ and $\tau^{(d)}$ extracted from figure 4.5 to estimate the respective diffusion activation energy $H_{\text{act}}^{(d/o)}$ and the pre-exponential factor $\nu_0^{(d/o)}$ in equation (4.21).

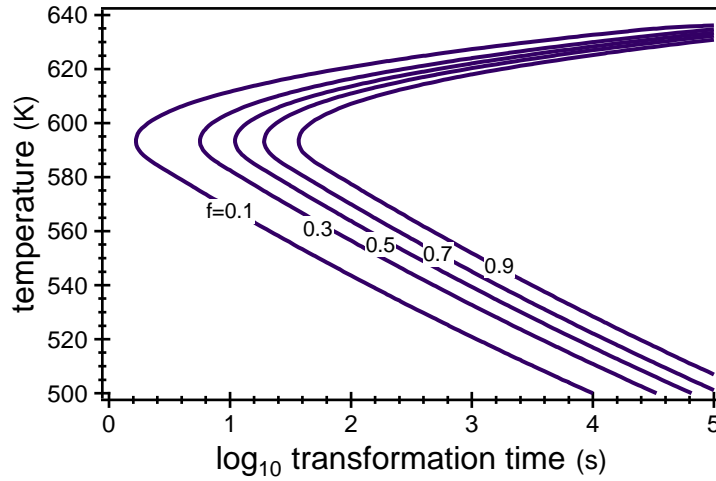


Figure 4.8: Calculated TTT diagram for the ordering process $\alpha \rightarrow \text{AuCu II}$, showing the volume fraction of ordered phase f as a function of temperature and transformation time.

Starting from an expression for the Landau free energy of AuCu — derived from an alloy Hamiltonian that takes the electronic properties of Au and Cu into account^[Ch92] — Šíma^[Si93, Si02] parametrized the potential barriers $F^{(o)}$ and $F^{(d)}$ in the temperature interval from $T_o - \frac{3}{4}\delta$ to $T_o + \frac{1}{4}\delta$ as follows:

$$F^{(o)}(T) = \frac{1}{3} n s \delta \left(1 - 3l(T) + 2l(T)^{\frac{3}{2}} \right)$$

and

$$F^{(d)}(T) = \frac{4}{3} n s \delta l(T)^{\frac{3}{2}}$$

where

$$l(T) = \frac{1}{4} + \frac{T_o - T}{\delta}.$$

Besides the equilibrium transition temperature T_o , the parameters are the width of the thermal hysteresis range δ , the discontinuity of the molar entropy s , and some energy scaling factor n . Outside the hysteresis interval, the energy barrier of the stable phase is set to zero, so that the transformation proceeds as fast as diffusion allows.

Fits to the kinetic data displayed in figure 4.7 yielded: $n = 2470$, $s = 0.31k$ (where k is the Boltzmann constant), $\delta = 67$ K, and, most importantly, a transition temperature of $T_o = 635.3$ K.¹ The latter is in excellent agreement with literature data ($T_o = 634$ K, and of inferior precision).^[AuCu]

Based on the rate equation (4.20), one can now use the full set of parameters to calculate the fraction of ordered domains as a function of (transformation) time

¹The systematic error on temperatures reported in this section is about 1 K. It is due to instabilities of the temperature control and the possible inaccuracy of its calibration.

and temperature:

$$f(t, T) = \frac{K^{(o)}}{K^{(o)} + K^{(d)}} \left(1 - e^{-(K^{(o)} + K^{(d)})t} \right)$$

The result is plotted on the transformation time vs. temperature diagram (TTT diagram for short) in figure 4.8.

The TTT diagram's "nose" indicates that the disorder-to-order transition is fastest at 594 K, where the transformation is nearly complete after a couple of minutes. This detail was impossible to deduce from the kinetics data in figure 4.7 alone. The problem lies in the fact that at temperatures too far below T_o (strong undercooling), the Zener peak shifts out of the observable frequency range and its breakdown goes unnoticed. In calculating the low-temperature part of the TTT diagram, we have exploited the fact that the Zener relaxation time is a measure of atomic diffusion, which in turn is the limiting factor of the disorder-to-order transformation rate at low temperatures.

On a final note, it should be pointed out that, in order to conduct similar measurements for any given alloy, the frequency range (of the torsion pendulum to be used) has to be chosen (or happen to be) such that the Zener relaxation peak appears close to the order-disorder transition temperature.

4.4 Order hardening in yellow gold

Mechanical spectroscopy was performed on polycrystalline, cylindrical samples (50 mm in length, 2 mm in diameter) of five of the 18-carat yellow gold alloys listed in table 1.1 on page 7. Measurements were carried out either in vacuum better than 10^{-5} mbar (alloys Au 118, Au 318, Au 418) and subsequently calibrated in temperature to account for the temperature gradient between temperature sensor and sample, or, in an effort to improve on temperature control, under a helium atmosphere of 7 mbar (Au 218 and Au 518). Generally, all reported temperature values have an uncertainty of up to 10 K.

Figure 4.9 shows the Zener relaxation peak of Au 518 (Au_{51%}Cu_{43%}Ag_{6%}) as measured in isothermal conditions. One remarks immediately that, with varying temperature (changed stepwise from one spectrum to the next), the Zener peak in Au 518 evolves in the same characteristic manner as it does in the binary Au_{57%}Cu_{43%} (compare with figure 4.4). However, though both alloys contain the same amount of copper, the Zener relaxation in Au 518 is considerably weaker, with a peak only little more than half the height (right before it breaks down) compared to Au_{57%}Cu_{43%}.

Figures 4.10 and 4.11 show the Zener peak in alloys Au 118 and Au 418, both in "cooling", i.e. at stepwise decreasing temperatures. The Zener relaxation is stronger by approximately one order of magnitude in Au 418, of higher copper content, compared to Au 118, the silver-richest of the series. Note that in

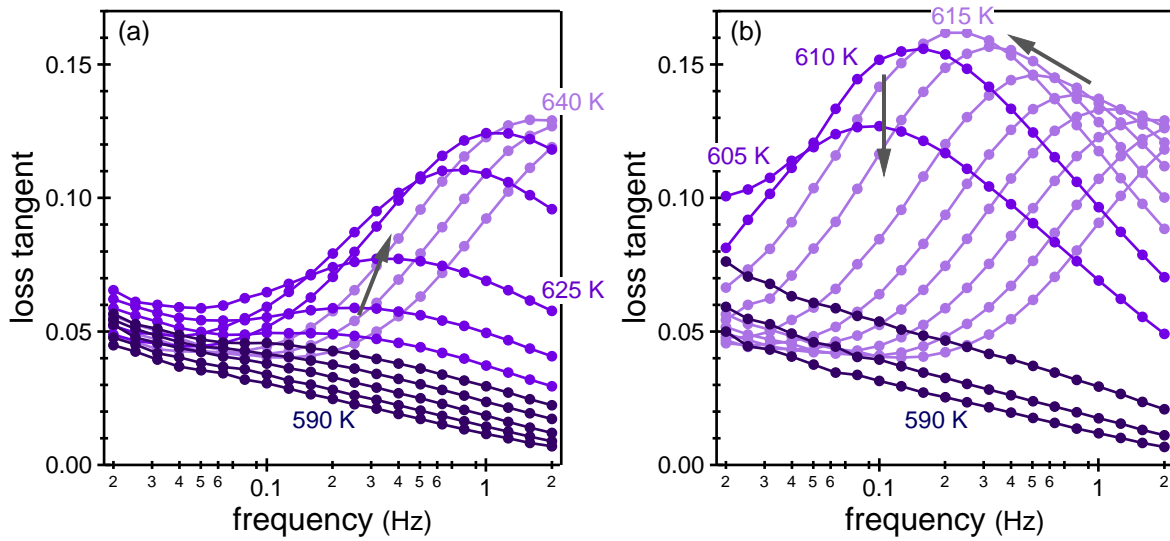


Figure 4.9: Mechanical loss frequency spectra of Au 518 in isothermal conditions at selected temperatures (steps of 5 K between curves) below and above the order-disorder phase transition. (a) Formation of the Zener relaxation peak with increasing temperature. (b) Critical evolution of the Zener relaxation peak height with decreasing temperature in the disordered α -AuCu phase (light shade), breakdown of the peak during the phase transformation (medium shade) to the ordered phase (dark shade).

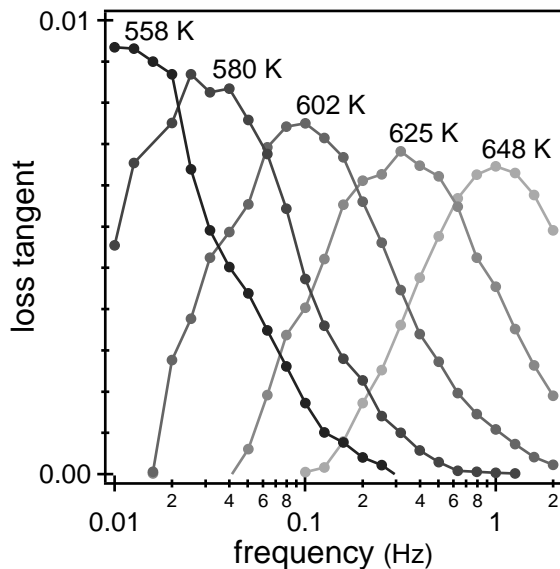


Figure 4.10: Isothermal mechanical loss spectra of Au 118, showing the increase of the Zener relaxation peak with stepwise decreasing temperature.

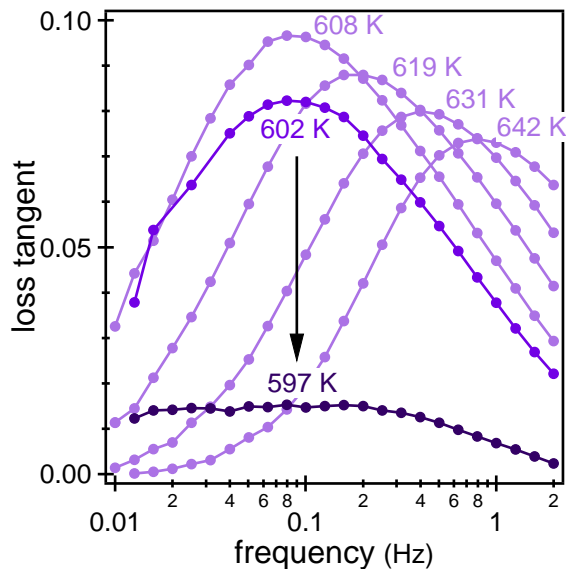


Figure 4.11: Isothermal mechanical loss spectra of Au 418, showing the Zener peak's increase before and its breakdown after the onset of long-range ordering.

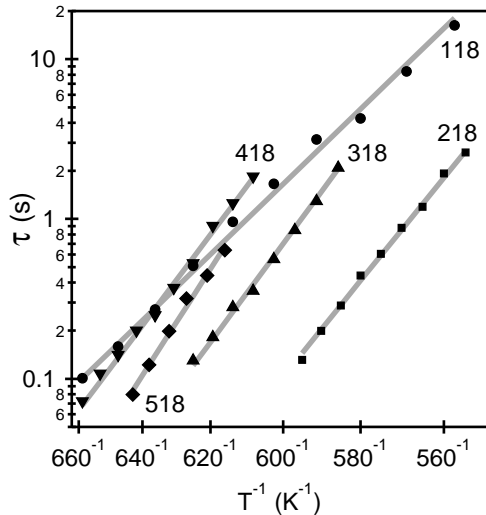


Figure 4.12: Arrhenius plots of the relaxation time τ of yellow gold alloys.

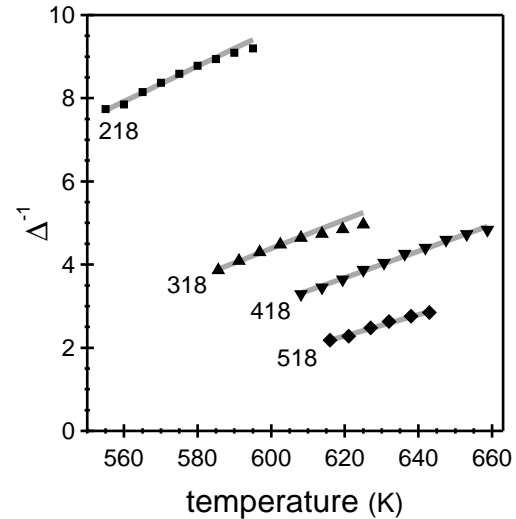


Figure 4.13: Curie-Weiss like temperature dependence of the Zener relaxation strength.

these two figures the background contribution, due to the grain boundary peak situated higher in temperature (lower in frequency), was subtracted in order to obtain the pure Zener peaks. However, as far as the peak heights are concerned, an uncertainty with respect to the background level persists, which is the more important the smaller the peak.

The major difference between Au 118 and Au 418 is that, while in the latter alloy the Zener peak clearly breaks down, no such behavior can be observed in the former alloy's spectra, nor has it been in any other measurement performed. The isothermal spectra of Au 218, 318, 3418 and 5618 (not shown) all exhibit the same characteristic breakdown of the Zener peak. Two of those alloys, Au 3418 and 5618, were excluded from the following analysis due to insufficient data regarding the background, which would introduce too great an uncertainty in the assessment of the peak height. From the sum of these observations it can be concluded that atomic ordering occurs in all yellow gold alloys except Au 118, at least not in the temperature region investigated so far.

As usual, the Zener relaxation's thermal activation manifests itself in the peak's shifting to lower frequencies with decreasing temperature. The corresponding Arrhenius plots are presented in figure 4.12. Fit results to the Arrhenius equation (2.14) are summarized in table 4.1, along with the log-normal distribution parameter β of peak broadening. As a general trend, one observes that the activation enthalpy H_{act} increases with copper content. Again alloy Au 118 stands out in that its peak is not broadened and its activation enthalpy considerably lower. Its limit relaxation time corresponds to an attempt frequency $\nu_0 = \tau_0^{-1}$ for the atomic diffusion process that, contrary to the rest of the alloy series, is reasonable, as it is close to the Debye frequency in copper (roughly 10^{13} Hz^[AM]). Arguably, the diffusion parameters in the other alloys are apparent values, overestimating H_{act} and underestimating τ_0 , due to the proximity to T_o , as we had

alloy	τ_0	H_{act}	β	T_o	T_c	C
118	10^{-14} s	1.6 eV	0	—	355 K	4 K
218	10^{-19} s	2.1 eV	1.61	550 K	380 K	16 K
318	10^{-20} s	2.3 eV	1.95	580 K	460 K	20 K
418	10^{-20} s	2.2 eV	1.61	605 K	502 K	22 K
518	10^{-22} s	2.6 eV	1.47	615 K	531 K	28 K

Table 4.1: Limit relaxation time τ_0 , activation enthalpy H_{act} , and log-normal distribution parameter β of the Zener relaxation peak, as well as transition temperature of long-range atomic order T_o , critical temperature of stress-induced ordering T_c , and anelastic Curie–Weiss constant C for five of the yellow gold alloys.

observed to be the case for $\text{Au}_{57\%}\text{Cu}_{43\%}$.

The relaxation strength Δ was calculated from the Zener peak's height at each temperature step, taking peak broadening into account. In all alloys Δ exhibits a Curie–Weiss type temperature dependence,

$$\Delta^{-1} = \frac{T - T_c}{C},$$

as demonstrated by the plots in figure 4.13. This is also true for Au 118, which, with Δ^{-1} ranging from 50 to 70, is not plotted for the sole reason of maintaining a convincing scale. The trend, however, is already recognizable in figure 4.10. Fits yield the anelastic critical temperatures T_c and anelastic Curie–Weiss constants C , which are reported in table 4.1.

An oft-employed argument in identifying a relaxation mechanism as being of the Zener type is to determine its relaxation strength from the peak's height in a temperature spectrum and proving that it varies with composition like c^2 (for small solute concentrations) or $c_A^2 c_B^2$ (in concentrated alloys). For the purpose of illustration, such a plot for yellow gold was presented in figure 3.5 (page 37 in section 3.1). We now understand why, in proximity to an order–disorder transition, this approach is fundamentally flawed and yields the inexplicable fit result illustrated on that figure. Isothermal studies allow for a more accurate analysis of the Zener peak's concentration dependence if they are based on the anelastic Curie–Weiss constant to eliminate the temperature dependence.

According to equation (4.19) from the theory section, C is given by:

$$C = c_A^2 c_B^2 \frac{v}{k} M_u \sum_p g(y_0) \lambda_p^2.$$

While all dynamic modulus data available from various mechanical spectroscopy measurements suggests that the unrelaxed modulus M_u varies little throughout the alloy series, this does not necessarily hold true for the state of local order y_0 (which might be affected by short-range ordering) nor the coefficients λ_p . However, the influence of the variation of the atomic volume v , albeit small, can be corrected by linearly interpolating the data for the lattice parameter of the solid

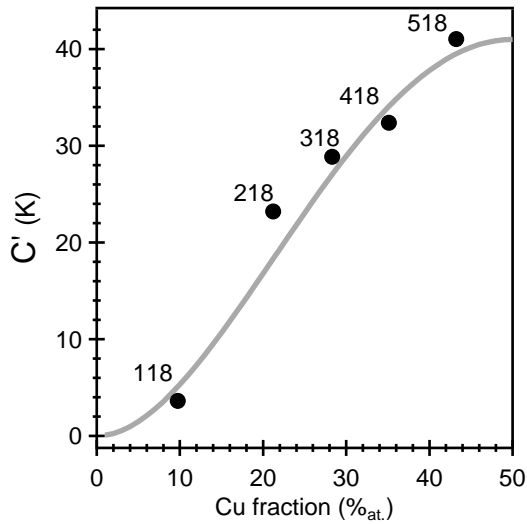


Figure 4.14: Normalized anelastic Curie-Weiss constant $C' = C(c) \bar{v}_0 / v_0(c)$ as a function of the copper concentration c , along with a fit function proportional to $c^2(1 - c)^2$.

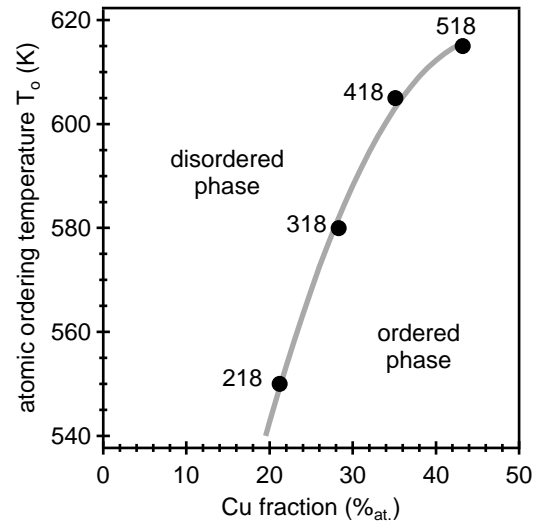


Figure 4.15: Order-disorder phase diagram of the yellow gold series as obtained from the breakdown of the Zener peak, along with a quadratic polynomial fit of the phase boundary.

solution collected in reference [Pr06](#). Figure 4.14 shows $C' = C \bar{v}_0 / v_0$ as a function of the copper concentration.

Arguably, one may conclude from figure 4.14 that the composition dependence of the relaxation strength is rather well described by the theory for concentrated binary alloys. Only Au 218 does not obey the fit of C' to $c_{\text{Cu}}^2(1 - c_{\text{Cu}})^2$ within the precision of the experiment. However, a possible concentration dependence of other factors but the atomic volume was disregarded in the assessment. Hence, it is just as if copper took on the role of one species, and gold or silver that of the other. Nevertheless, this simplified picture is somewhat contradicted by the difference in relaxation strength of Au 518 compared to Au_{57%}Cu_{43%}.

The transition temperature of long-range atomic order, T_o , is also reported in table 4.1 and plotted, like a phase diagram, in figure 4.15. The estimated phase boundary (for arbitrary copper concentration) represents a polynomial fit of the data points. For each alloy the value of T_o was ascertained from the approximate temperature at which the Zener peak (and thus the disordered phase) becomes unstable. In Au 418 for example, the phase transformation sets in at about 605 K, see figure 4.11. As explained in the theory section, the phase transition temperatures are systematically higher than the critical temperatures of self-induced ordering, T_c , see table 4.1.

As for Au 118, where the Zener peak is still observed at a temperatures as low as 558 K in figure 4.10, a T_c of only 355 K indicates a rather low $T_o \gtrsim T_c$. At this temperature, solute diffusion is too slow to promote the ordering transformation. In effect, the Zener relaxation time, which is of the same order of magnitude as the mean time between atomic jumps, is already 20 s at 560 K and further increases exponentially (figure 4.12). One can therefore conclude that atomic

ordering does not occur at this composition, and even if it did, the transformation time would be too long for practical applications.

The transition temperatures reported here agree well with the ternary phase diagram.^[Pr06] It is, however, worth noting that in literature dedicated to the metallurgy of 18-carat yellow gold used for jewelry (references [Mc78](#), [Ra90](#), and most recently [Ro08](#)) the extent of the ordering region is systematically underestimated.

A conspicuous detail in the spectra of Au 518, figure 4.9, is that after the Zener peak's breakdown only the background remains and no residual peak is discernible. This contrasts with the observations made in Au_{57%}Cu_{43%}, figure 4.4, where the residual peak offered the opportunity to obtain diffusion data in the ordered phase.

The absence of the Zener relaxation peak after atomic ordering may be understood as a consequence of phase separation, which in Au 518 should occur even before ordering sets in (see figure 1.9 on page 12). This is not the case for the other alloys. In fact, for an alloy very similar in composition to Au 418, electron micrographs and diffraction patterns indicate a $\alpha \rightarrow \text{AuCu I} + \alpha_2$ phase transition at 593 K^[Na88] (12 K lower than T_0 reported here), i.e. atomic ordering and phase decomposition occur at the same time. While at high temperature stress-induced ordering takes place in the solid solution of all three constituents, with its strength depending mainly on the copper concentration, alloy Au 418 would separate into a disordered silver-rich phase and an ordered copper-rich phase, where, if one is inclined to accept this explanation, the composition of the latter approaches the stoichiometric one for which the Zener peak disappears entirely.

As pointed out at the beginning of the theory section, the gold–silver system also features a Zener relaxation. For a gold atom fraction corresponding to that of Au 418, this Zener peak, produced by the silver-rich disordered phase, should appear in the frequency spectrum at temperatures around 600 K according to reference [Tu60](#). The Au–Ag Zener relaxation is considerably weaker than the one in Au–Cu. It would be further diminished in a two-phase material where the total relaxation strength is given by a lever rule (as is, for example, the case with γ' precipitates forming in Al–Ag^[Q5.5]). Indeed, a small peak can be perceived in the frequency spectrum of Au 418 at 597 K (figures 4.11 and 4.16), and, though the data is sketchy, it seems to be centered at *higher* frequency than the original Zener peak before its breakdown — as opposed to the expected trend. (Unfortunately, for the remaining alloys the data is inconclusive.)

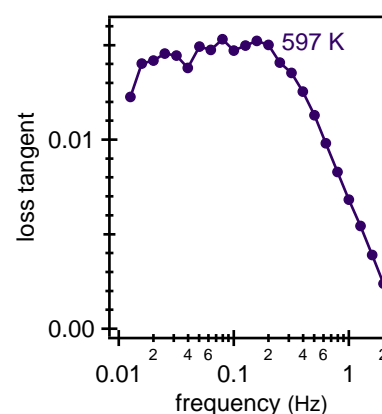


Figure 4.16: Residual peak in Au 418, the same as in figure 4.11 but on a different scale.

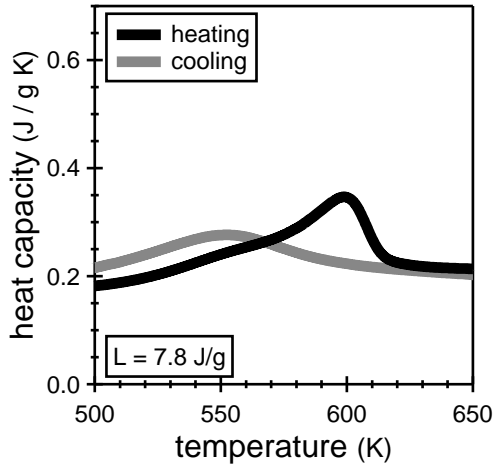


Figure 4.17: Differential scanning calorimetry of Au 418 at 10 K/min heating and cooling rate.

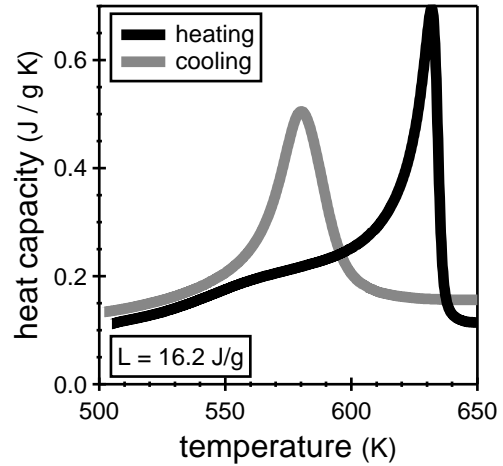


Figure 4.18: Differential scanning calorimetry of Au 518 at 10 K/min heating and cooling rate.

Just like in AuCu, the observed phase transition is of first order, since the same arguments as for Au_{57%}Cu_{43%}, in section 4.2, can be applied to the isothermal mechanical loss spectra of the Zener peak in yellow gold (such as Au 518's in figure 4.9). Differential scanning calorimetry was performed to confirm that the transformation is indeed associated with a latent heat. In calorimetry, the latent heat manifests itself as a sharp peak, particularly during heating, superimposed on the otherwise continuous curve of heat capacity versus temperature. The sharp peak in heating is due to the fact that, for first-order transitions, most of the latent heat is released when the low-temperature ordered phase becomes unstable (it is but metastable at the equilibrium transition temperature), and order parameter, entropy and enthalpy incur a sudden discontinuous change.^[Q5.1] In cooling, the discontinuity is less pronounced as the transformation is kinetically inhibited by slower diffusion and, in most cases, the necessity to first create nuclei of a minimum critical size (which also enlarges the hysteresis).

Results are presented in figures 4.17 and 4.18 for Au 418 and Au 518, and show the expected features in both cases. The peaks in Au 418 are however much broader. The curves generally resemble those reported for AuCu, including the broad hump in the heating curve before the peak (attributed to configurational disordering while the equilibrium order parameter begins to decrease).^[Ba01] However, note that the heating rate used for the measurements presented here is too high to resolve the small bump that would, possibly, signal the AuCu I \rightarrow AuCu II type phase transformation right before disordering.^[Fe99]

By integrating the area under the peak in heating, the latent heat (or rather the enthalpy difference between the fully ordered and the disordered state) was found to be about 8 J/g in Au 418 and roughly twice that, 16 J/g, in Au 518. The most recent evaluation of the latent heat of AuCu (associated with the full AuCu I \rightarrow α order-disorder transition) yielded 21 J/g.^[Ba01] There is considerable error on the values reported here, but the same is true for the various (and greatly

varying) results for AuCu's latent heat reported throughout literature.^[Fe99]

It is virtually certain that during all age-hardening treatments performed in industry (typically at 550 K^[AD318]) a superstructure of AuCu I type, not AuCu II, is formed. This implies that the hardening mechanism of AuCu, reviewed in section 1.3, also governs the age-hardening of the hardenable yellow gold alloys, with the added difference that silver-rich disordered domains form as well.

A AuCu II type ordered phase, should it even exist in a given yellow gold alloy, would only be stable in a very narrow temperature range below the disordered phase that lies most probably entirely within the region covered by the hysteresis (as suggested by the calorimetry data). This is so because the driving force for the nucleation of ordered domains is very low at such little undercooling. To produce a specimen of (possible) AuCu II order, one would rather stabilize the AuCu I phase first, then make a second heat treatment close to the disordering temperature. The attempts made in our lab with Au 518 samples, following the described scheme, were not crowned by success, i.e. these samples never exhibited X-ray diffraction patterns indicating a AuCu II superstructure, in which case AuCu I's 110 peak (see figure 2.8 shown as illustration on page 32) would split into two separate peaks^[Fe99] due to the presence of *periodic* anti-phase boundaries. Of course, the chosen annealing temperature (600 K) or, particularly, the length (two hours) of the applied heat treatment may have been inadequate to produce this change.

4.5 Zener peak in white gold

As pointed out in chapter 3, the temperature spectra of those white golds containing neither indium nor gallium resemble the spectra of yellow gold in that they all feature the same two peaks: the first due to the Zener relaxation, the second due to grain boundary sliding. The Zener peak in white gold is situated higher in temperature, typically at about 700 K at 1 Hz, and often closer to the grain boundary peak.

Figure 4.19 shows isothermal spectra of the Zener peak as measured in Au 5125. It is superimposed on the grain boundary peak, which is larger and broader.

In order to properly subtract the background, the fit illustrated in figure 4.21 was performed. During the fitting procedure, the activation enthalpies were fixed at the values obtained from separate Arrhenius plots for the Zener peak (figure 4.22) and the grain boundary peak (figure 5.6 on page 87 in chapter 5). To correct for the possible inaccuracy of the temperature calibration, τ_0 was allowed to vary (and did so only a little). Besides the grain boundary peak, no other background contribution was considered.

The fit is in excellent agreement with the measured spectrum. The information thus obtained on the background was used to extract the pure Zener peak at each temperature. The result is plotted in figure 4.20. The height of the peak

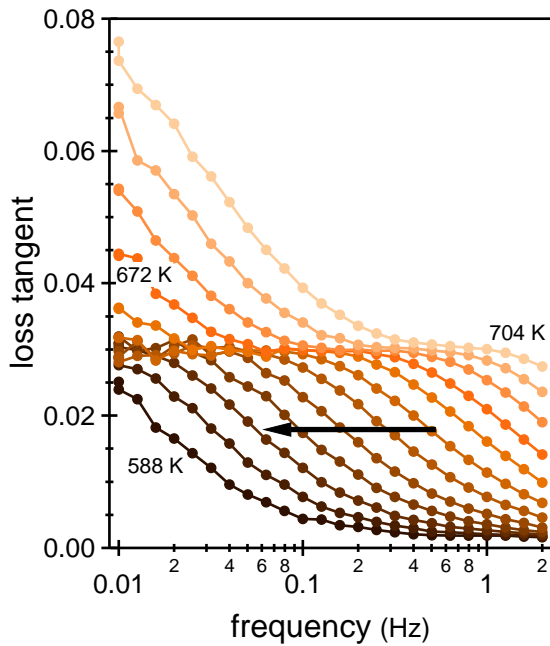


Figure 4.19: Isothermal spectra of the Zener peak in Au 5125 superimposed on the grain boundary peak.

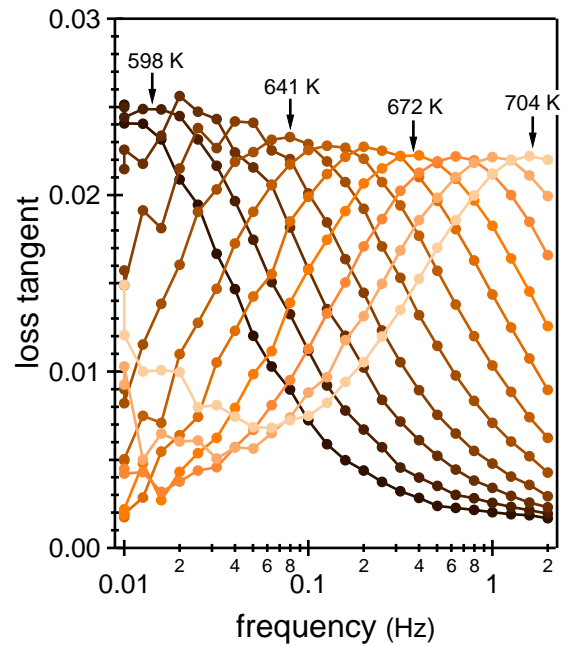


Figure 4.20: Zener peaks in Au 5125 after subtracting the background due to the grain boundary peak.

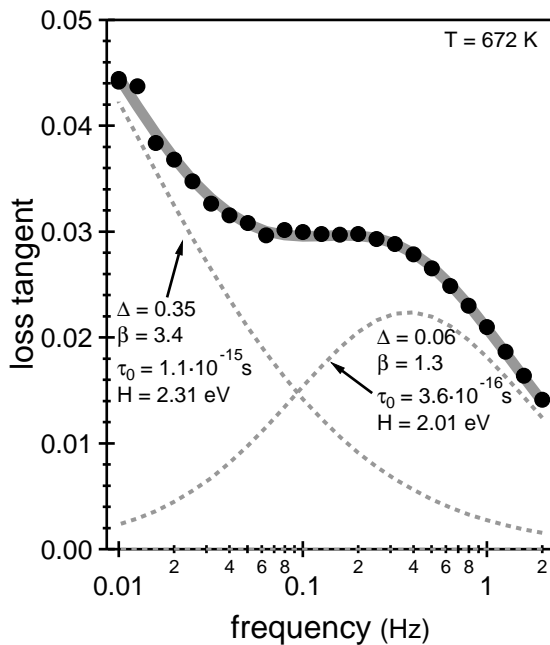


Figure 4.21: Fit of Zener and grain boundary peak in Au 5125 at 672 K to two broadened Debye peaks.

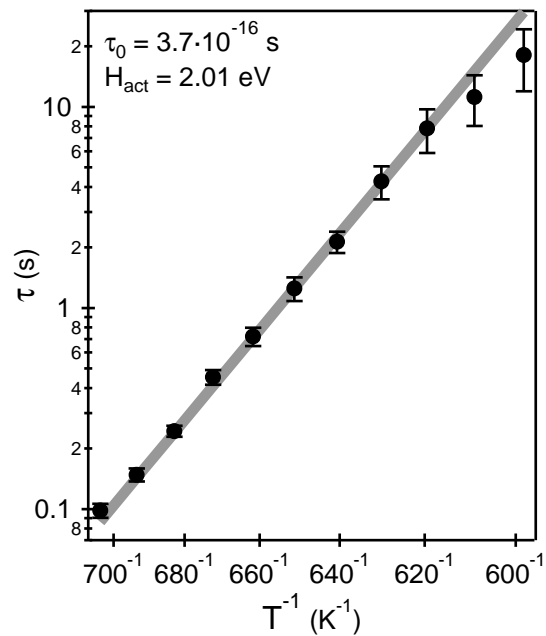


Figure 4.22: Arrhenius plot for the Zener peak in Au 5125.

increases with lowering temperature, a characteristic feature of the Zener relaxation. However, compared to those yellow gold alloys that form an ordered phase, the peak grows little over the observed temperature range and is obviously far from the critical temperature of self-induced ordering. No breakdown of the Zener peak was ever observed in this alloy. Hence, just like for Au 118, one can argue that no atomic ordering occurs in Au 5125 and exclude this phenomenon as a possible candidate for age-hardenability.

The characteristic temperature dependence of the Zener peak is even more pronounced in Au 5130 as figure 4.23 testifies. To test if the peak eventually does break down, a long annealing was performed at about 550 K. The mechanical loss level was monitored over the course of almost three weeks at a frequency as low as 0.001 Hz. Temperature and frequency so chosen should correspond to some point on the Zener peak's right flank (in the frequency spectrum). Any such point would decrease by the same factor as the peak's maximum when the peak breaks down. The result is shown in figure 4.24. Each data point on this graph is actually the average value of mechanical loss measurements during more than 6 hours. This was done to eliminate some of the scatter in the data, which is inevitable at this low a frequency.

Unfortunately, the data is inconclusive. While one observes an obvious trend in figure 4.24, it could never be established that atomic ordering does indeed occur. X-ray diffraction performed in our lab showed no trace of any superstructure whatsoever. Furthermore, the alloy does not harden during thermal treatments such as the one it underwent in this experiment.

In the Au-Pd based alloy Au 5210, the Zener peak is situated about 100 K higher in temperature compared to other white golds. Actually, attributing this peak to a Zener relaxation is somewhat speculative. After all, this alloy does not contain any copper. To the knowledge of the author, pure Au-Pd has never been studied by mechanical spectroscopy. Furthermore, gold-palladium is one of the few alloy systems that actually follow Vegard's law rather well.^[AuPd] Deviations from the law have however been observed, and they are strongest at about 60% gold.^[Ma64] The gold fraction in Au 5210 is 62%. A slight increase of the peak's height from high to low temperature can be observed in the isothermal spectra in figure 4.25, though this effect is small and little convincing. There are no signs of atomic ordering in this alloy either.

The general shift of the Zener peak to higher temperatures compared to the yellow golds can be understood as being due to the involvement of palladium. The fact that palladium additions always increase the alloy's melting point implies that Pd atoms form bonds stronger than the other elements all by themselves. As these bonds must be broken for atomic diffusion to take place, the presence of palladium in the matrix arguably increases the activation enthalpy of self-diffusion for any element. Consistent with this reasoning, the Zener peak's activation enthalpy in Au 5210 is 0.3 eV higher than in Au 5125, see the Arrhenius plot in figure 4.26.

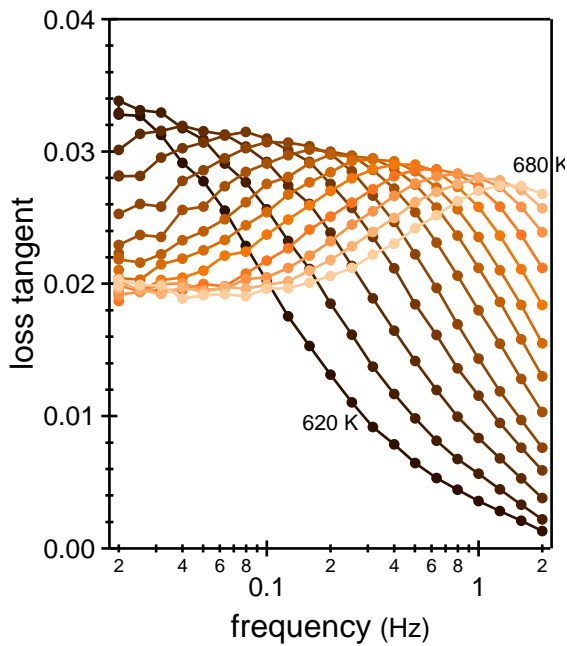


Figure 4.23: Isothermal spectra of the Zener peak in Au 5130 superimposed on the grain boundary peak.

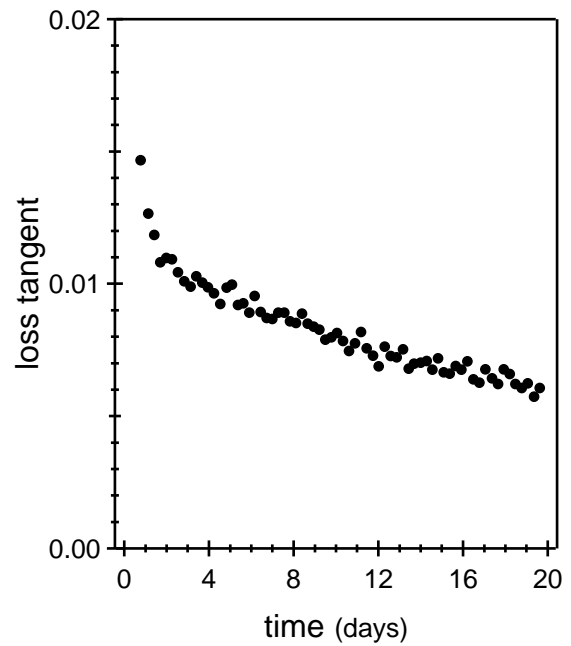


Figure 4.24: Mechanical loss at 0.001 Hz and about 550 K as a function of time during long-term annealing of Au 5130.

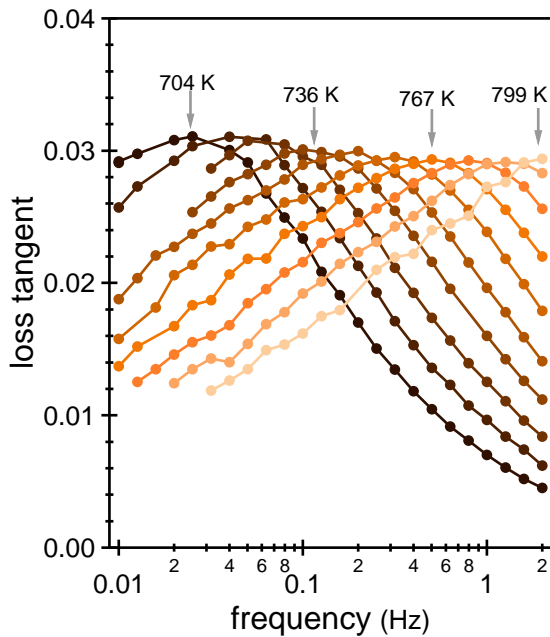


Figure 4.25: Zener peak in isothermal conditions in Au 5210.

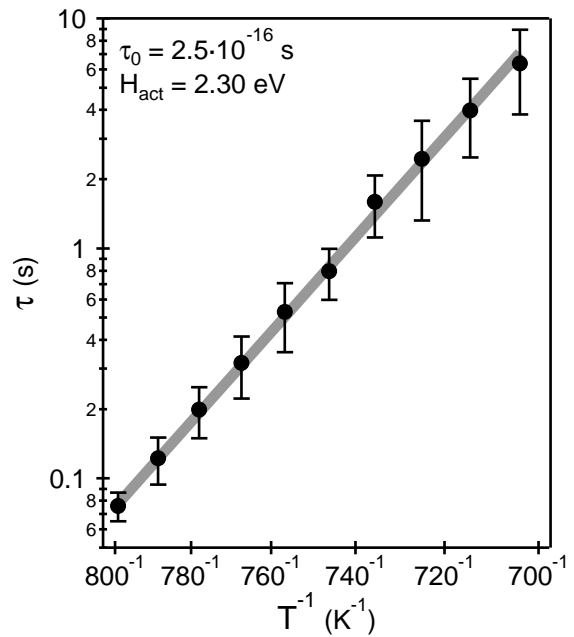


Figure 4.26: Arrhenius plot for Au 5210's Zener peak.

Chapter 5

Grain Boundary Sliding blocked by Precipitates

In chapter 3, based on the observation that the high-temperature peak only appears in the spectrum of polycrystals but not single crystals, we concluded that the corresponding relaxation results from the relative sliding of adjacent grains along their common boundary. The very same argument was first made in 1947 by Ting-Sui Kê, then a post-doctoral scientist in the research group headed by Clarence Zener, in his interpretation of the spectrum of (poly- and monocrystalline) aluminum.^[Ke47] As opposed to the Zener peak discussed in the previous chapter, which was discovered at about the same time, the veracity of Kê's interpretation has been disputed — and even rejected by some^[Be04, Wo81] — over the years. At the small stress amplitudes that are put into play during mechanical spectroscopy, it seemed questionable how, in a metal, the two-dimensional macroscopic defect that is a grain boundary becomes mobile at temperatures only little higher than for (zero-dimensional) point defects, and way before (one-dimensional) dislocations. The debate was still going on as recently as 2004.^[Be04]

In view of this controversy, one objective of this chapter will be to compile as much evidence as possible that the high-temperature peak observed in 18-carat gold is in fact due to grain boundary sliding. In a first step, the experimental data will be confronted with a continuum model of grain boundary sliding, which describes the polycrystal as an assemblage of elastic grains separated by glissile boundaries.

The interpretation of the peak as due to grain boundary sliding will be further substantiated by observations made in those white gold alloys containing indium and gallium. Below a certain temperature, they form a stable phase with some of the alloy's other elements. When the second-phase particles precipitate, they block grain boundaries and prevent them from sliding. This can be directly observed in the spectra, which show the breakdown of the grain boundary peak — a behavior similar to the Zener relaxation at the disorder-to-order transition.

Hardness measurements and mechanical spectroscopy of single crystals will then show that precipitates do not only block grain boundaries, but also pin dislocations inside the grains. This explains the age-hardenability of these alloys.

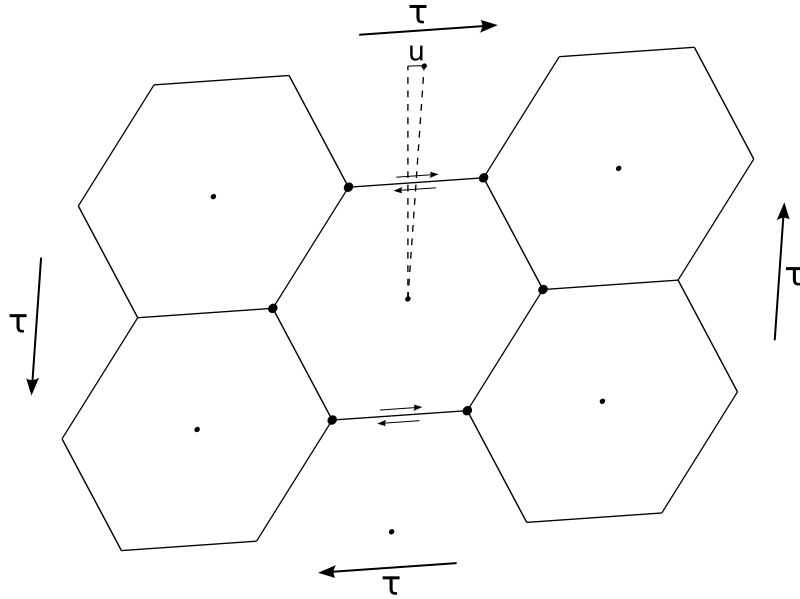


Figure 5.1: Shearing of a honeycomb type grain assemblage, made up of grains shaped like hexagonal prisms.

5.1 Grain boundary sliding in metals

A first model for grain boundary sliding in metals was developed by Zener in 1941.^[Ze41] It was found to be in excellent agreement with Kê's measurements of the grain boundary peak in aluminum six years later.^[Ke47a,Ke47b,NB15] Therefore, the outlines of Zener's model shall be recalled.

Consider the application of a shear stress τ to a periodic grain assemblage, such as the hexagonal prisms forming the honeycomb-like arrangement illustrated in figure 5.1. If the entire polycrystal behaves as a homogeneous (and isotropic) elastic medium, the resulting displacement field is simply $\vec{u}(x, y, z) = (\gamma y, \gamma x, 0)$, i.e. all volume elements are in a state of pure shear, with shear angle $\gamma = \frac{\tau}{G_u}$. As usual, G_u denotes the unrelaxed shear modulus.

We now allow sliding along grain boundaries and consider only the relaxed state, i.e. when all sliding processes have come to a halt. On the relaxed state we impose the condition that grain boundaries shall no longer transmit any shear stress. Similar to a jigsaw puzzle, the remaining rigidity is then due to local stresses accumulating near triple junctions, where boundaries of different orientations meet and sliding is impossible. Obviously, this scenario is an exaggeration, otherwise bicrystals would fall apart at the temperature of grain boundary sliding. In reality, grain boundaries are not perfectly flat, but contain ledges that, besides triple junctions, also form obstacles to slip. This problem was addressed by Raj and Ashby whose model describes grain boundaries with a periodic wavy (or even bumpy) profile.^[Ra71] Nevertheless, flat profiles, as in Zener's model, should yield a lower bound for the relaxed shear modulus.

In the relaxed state, the stress and strain fields are inhomogeneous. The displacement field is even discontinuous at the grain boundary: it incurs a jump in its parallel component. Volume elements next to the boundary are under tensile stress only, as opposed to the grain centers which, for symmetry reasons, remain in a state of pure shear. Grain boundary sliding is thus accommodated by *elastic deformation of the grains*. The relaxed average shear angle is given by the relative displacement of neighboring grain centers.^[Fo95] The relaxed displacement field can be determined by solving the equilibrium equations of elastostatics under the boundary conditions as described.

Without going into the details of this calculation, we can already draw two important conclusions. First, as the strain field is an intensive thermodynamic variable, it remains invariable under a spatial scaling transformation, i.e. $\epsilon(\alpha \vec{r}) = \epsilon(\vec{r})$. Hence, unrelaxed *and* relaxed shear angle are independent of grain size, and therefore also the relaxation strength, given by their ratio. This is even easier to see if one realizes that the average shear angle of the periodic structure is always given by the triangle drawn in figure 5.1, and obviously independent of the figure's scale. It is this symmetry argument that distinguishes sliding accommodated by elastic deformation of the grains from sliding accommodated by diffusion, such as Coble or Nabarro-Herring creep in ceramics. In the latter case, which might occur at rather high temperature (with respect to the material's melting point), matter transported over long distances changes the geometry of the grain structure and thereby redistributes the internal stresses. The restoring force is then no longer proportional to the anelastic strain. It might even vanish entirely, in which case there is no mechanical loss peak but only a continual increase with temperature (steady-state creep).

Second, as the displacement field is extensive, i.e. $\vec{u}(\alpha \vec{r}) = \alpha \vec{u}(\vec{r})$, the distance grain boundary elements have to cover scales with grain size d . The rate of sliding though is controlled by microscopic processes (the *intrinsic* grain boundary viscosity), so it cannot depend on the overall sliding distance. Therefore, the relaxation time should be proportional to grain size, $\tau \propto d$. The small grain size exponent of 1 also distinguishes elastic accommodation from diffusional creep, where it is between 2 (volume-controlled diffusion) and 3 (boundary-controlled).^[Ra71]

Both conclusions hinge on the assumption of perfectly flat grain boundaries. For realistic boundaries containing ledges it is questionable (though not impossible) that the spacing of those steps would scale with d . Conversely, however, an experiment where, for a polycrystal, τ increases with d and Δ varies only little should be seen as an indicator that grain boundary sliding is primarily accommodated by elastic deformation of the grains. As opposed to ceramics, this is the expected behavior for metals.

The solution of the displacement field's boundary value problem is generally difficult. Zener made a significant simplification by assuming all grains were spherical, since for spheres the theory of elasticity is well known. He could thus solve

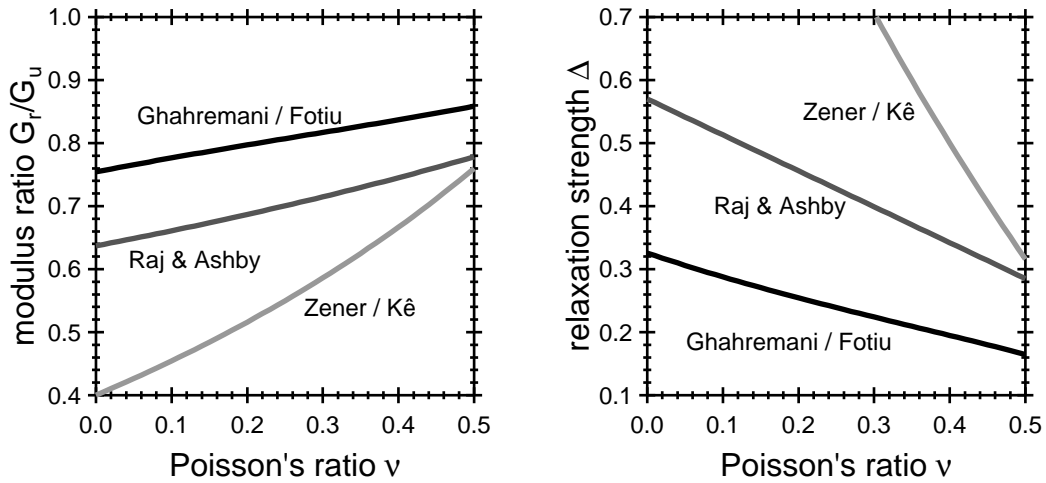


Figure 5.2: Modulus ratio and relaxation strength predicted by the continuum model of elastic grains accommodating the complete shear stress relaxation across flat grain boundaries, according to references Ze₄₁, Ke₄₇^a, Gh₈₀, Fo₉₅ and Ra₇₁.

the problem for a polycrystal under tensile stress. Kê applied the theory to shear-ing and found for the ratio of relaxed to unrelaxed shear modulus: [Ke₄₇^a]

$$\frac{G_r}{G_u} = \frac{27 + 5\nu}{57 - 4\nu}. \quad (5.1)$$

It depends only on the Poisson's ratio ν of the elastic grains. The modulus ratio is related to the relaxation strength Δ , equation (2.9), as follows:

$$\Delta = \frac{G_u}{G_r} - 1. \quad (5.2)$$

For aluminum's $\nu = 0.35$, equation (5.1) yields a modulus ratio of 0.63. This agrees very well with Kê's measurement of 0.67. [Ke₄₇^a] Therefore, in literature reviews of the grain boundary peak, Kê's work is often presented as evidence for Zener's theory.

However, such an assertion overlooks the fact that the approximation made in deriving equation (5.1) is rather crude: it is based on the boundary conditions of spherical grains, which only touch in a few points and do not pack to fill space. Ghahremani^[Gh₈₀] and later Fotiu^[Fo₉₅] each applied different finite element methods (FEM) to solve the problem for the hexagonal prisms of figure 5.1. They both found the same numerical solution, which can be approximated by the formula:

$$\frac{G_r}{G_u} = \frac{1 + \nu}{1 - \nu} \frac{0.86 - 0.83\nu}{1.14 + 0.83\nu}. \quad (5.3)$$

As Fotiu pointed out, this result can be considered the "exact" solution for the honeycomb grain structure since it did not change with mesh refinement.

Figure 5.2 compares both solutions of the continuum model. (Raj and Ashby's result, extrapolated to the case of flat boundaries, is also shown.¹) The Zener/Kê formula yields huge relaxation strengths for small Poisson's ratios. The 2d-FEM prediction is much more conservative. For aluminum's $\nu = 0.35$, it gives a modulus ratio of 0.83. In view of the fact that this represents a lower bound (flat grain boundaries were assumed), one must conclude that, in fact, Kê's findings in aluminum are at variance with Zener's model of elastically accommodated grain boundary sliding. It could be argued that the honeycomb grain structure is asymmetric in its treatment of the third dimension. However, it is generally considered to provide a realistic description of the multi-grain continuum and is commonly applied to model metals^[Ra71] as well as ceramics^[Q4.3].

Assuming that sliding occurs in a viscous manner, i.e. the internal friction force acting along the boundary is proportional to the boundary's average slip velocity \dot{x} , the entire relaxation process can be modeled by a standard anelastic solid. The dashpot's viscosity η (see figure 2.1 on page 23) is then given by the product of grain boundary viscosity η_{gb} and grain size d . Obviously, the grain boundary viscosity would be thermally activated and determine the activation enthalpy of the peak.

Kê's results supported the prediction that τ scales with grain size. Subsequent to Kê's work, grain boundary peaks were identified as such in a number of metals, among them gold, silver and copper.^[NB15] However, these studies also revealed contradictions in the grain-size dependence of the relaxation parameters: the relaxation strength would vary considerably between materials — possibly indicating that the elastic medium's anisotropy, neglected in Zener's model, might play a role —, and often $\tau \propto d^2$ was found.^[NB15] Moreover, in lieu of a single peak, many metals of the highest purity (99.999%) feature a double peak. This (and other observations) prompted some authors to question the existence of a grain boundary peak altogether: the high-temperature double peak in high-purity aluminum was attributed to dislocation damping instead.^[Q3.4, Ri81]

Peters et al.^[Pe64, NB15] studied the grain boundary peak in copper. It appears in the mechanical loss temperature spectrum at around 550 K. Fits to a broadened Debye peak yielded a relaxation strength $\Delta = 0.158$. A direct measurement of the modulus ratio gave 0.875. Using equation (5.2), valid for a standard anelastic solid, this corresponds to $\Delta = 0.143$, leaving a discrepancy of about 10% to the value obtained from the mechanical loss. The modulus ratio is, for once, consistently above the lower bound given by the continuum model of hexagonal grains. With a log-normal distribution parameter β greater than 5, the peak in copper is very broad. It was observed that the peak broadens even further with increasing grain size. While β increased, the peak height decreased, leaving the relaxation strength Δ constant.

¹A flat grain boundary in Raj and Ashby's model has a profile of periodicity d and imitates the outlines of successive hexagonal grains throughout the entire honeycomb structure of figure 5.2 in either the x- or y-direction.

These experimental findings in copper and many other studies^[NB¹⁵] all substantiate the view that grain boundaries in metals slide viscously, i.e. behave like a standard anelastic solid. The mechanical loss is independent of amplitude, no threshold stress need be overcome.

The latter is at variance with modern ab initio (Monte Carlo and density functional theory) simulations of grain boundary sliding^[Mo₉₆] that, for copper^[Ba₀₁^a] and also aluminum^[Mo₉₇], predict a slip-and-stick mechanism. These studies found that a grain boundary's energy increases drastically for very small relative displacements, requiring a critical stress to overcome the energy barrier and slip to the next energy minimum. However, incorporating grain boundary vacancies into the calculation seemed to reduce the energy variations.^[Ba₀₅] More sophisticated studies might therefore reconcile this apparent contradiction. Molecular dynamics simulations for aluminum yielded results in better agreement with experiment, predicting a constant slide velocity at intermediate stresses, but also the absence of sliding at low stress (indicating a threshold) and a non-linear sliding behavior at high stress.^[Qi₀₇]

Assuming $\tau \propto d$ to be true, Peters et al. noted that the distribution of grain sizes, while typically log-normal itself, would only account for a small part of the overall broadening, having a β less than unity.^[Pe₆₄] After all, the grain size distribution would translate to a distribution of $\ln \tau_0$ within the continuum model. Even higher grain-size exponents would not explain the discrepancy.

The remaining broadening must be attributed to a rather wide distribution of activation energies. This is understandable considering the diversity of atomic structures the various grain boundaries formed in a polycrystal possess. Grain boundaries emerge as interfaces during (re-)crystallization of grains. They have five degrees of freedom: three for the relative orientation of the grains, two for the orientation of the boundary plane. If the lattice misorientation is rather small, the grain boundary can be imagined as a regular array of dislocations. This concept loses meaning for high-angle grain boundaries, i.e. for misorientations greater than 20° .^[Q_{4.1}¹] High-angle grain boundaries should exhibit a higher degree of disorder. That is, unless the misorientation is such that there is some symmetry relation between the two lattices (coincidence site lattice, CSL). It is therefore very reasonable to believe that the activation energy of the rate-controlling single-step process producing the sliding motion varies significantly from one boundary to another.

The question, which single-step process that is, has received a lot of attention, but so far no definitive answer. Experiments have shown that in f.c.c. metals the activation energy of atomic diffusion along the core of a grain boundary, H_{gb} , is about half the energy of self-diffusion, H_{sd} , inside the grain.^[Q_{4.1}¹] Diffusion is facilitated by the higher degree of disorder at the interface. In high-purity metals, the activation energy of the grain boundary peak was often, though not always, found near H_{gb} , while for solid solutions the peak's activation energy was mostly higher than or equal to H_{sd} .^[NB¹⁵, Q_{4.2}¹]

A number of models have been proposed that would explain either one or the other value. Diffusion of single atoms from one position inside the boundary's core to another, and thereby inducing a stress relaxation, would be the simplest one. This, however, implies that grain boundaries resemble an amorphous phase, while in metals they are known to have a crystalline structure.^[Q4.1]

Consequently, as Ashby pointed out, sliding at the boundary must involve the motion of boundary dislocations along its surface.^[As72] Such dislocations are a structural feature of most grain boundaries. According to Ashby's model, dislocation glide in the boundary plane is accompanied by diffusion of single atoms across the boundary, i.e. from one grain to the opposite side. Grain boundary sliding is thus coupled with grain boundary migration, and the activation energy is given by H_{gb} .

Lakki and Schaller^[La98] argued differently: as a grain boundary is typically not a glide plane, dislocation motion must involve climbing as well. This necessitates the formation of jogs, and the migration of these jogs over the extent of the dislocation line. Obviously climb, not glide, is the rate-controlling process, and the activation energy is given by the sum of H_{sd} and the activation energy of jog formation.^[Q4.1,La94]

It should be noted that, in terms of dislocations, *elastic* accommodation implies that the dislocation loops merely bow out in response to the applied stress, towards regions of higher local strain such as triple junctions. Once they break away from their pinning points, a component of *plastic* deformation is added, which reduces the restoring force. If that is the case, the relaxation strength becomes, again, grain-size dependent. Such a scenario is incorporated into Lakki and Schaller's model.^[La98]

Most recently, Shi and co-workers studied grain boundary sliding in aluminum bicrystals.^[Sh05, Ji05, Sh06, Ko09] They based their interpretation of the mechanical spectroscopy data on Ngai's coupling model.^[Ng79] The main idea behind this approach is that the single-step processes — whichever they may be — are not independent, but, to some degree, correlated. The universality of this claim was substantiated by the successful application of the coupling model to a variety of relaxation processes. The observable consequence is a retardation of the relaxation response. In terms of mechanical spectroscopy, the effect is twofold: the mechanical loss peak deviates from the Debye shape, becomes asymmetric (on a plot versus $\log \omega$ or $\frac{1}{T}$) and broadens, while the measurement of activation parameters (from an Arrhenius plot) yields only apparent values E^* , τ_0^* , which are related to the true values as per

$$E = (1 - n)E^* \quad \text{and} \quad \tau_0 = t_c^n \tau_0^{*(1-n)}, \quad (5.4)$$

where n ($0 \leq n \leq 1$) denotes the coupling parameter and $t_c \approx 10^{-12}$ s the time of crossover from the Debye regime to the non-Debye regime. The coupling model agrees well with Shi et al.'s experimental data in that the peak was indeed noticeably asymmetric and could be fit to a single non-broadened (non-Debye) peak predicted by the model. When, in an earlier evaluation, the same data was fit

to a regular Debye peak, broadening parameters β ranging from 0.25 to 1 had to be admitted, despite the fact that a bicrystal contains only a single grain boundary.^[J105] The coupling parameter n , obtained from the fits to the non-Debye peak, varied between 0.2 and 0.5, depending on boundary type and misorientation angle. The “decoupling” would thus reduce the measured activation energy to a more reasonable value, below H_{sd} . However, the authors did not specify which atomistic processes they had in mind.

Second-phase particles, when precipitating from the solid solution, tend to segregate at grain boundaries, as these offer preferential nucleation sites due to their intrinsic disorder and faster diffusion paths. Since grain boundaries are very thin objects, no more than a few atoms wide, the particles extend far into the adjacent grains. Just like triple junctions and boundary ledges, they will thus oppose the sliding of the grain boundary: local stresses build up so that the boundary area around the particle no longer contributes to the average boundary displacement, which reduces the overall relaxation strength. This phenomenon has been directly observed in transmission electron microscopy, or rather its reverse effect on the particle itself, which suffers a shear deformation and rotation due to the two grains pushing in opposite directions.^[Mo93] Therefore, in the vicinity of a particle, sliding cannot be accommodated elastically, but only by diffusion of matter.

Mori et al.^[Mo83] have calculated the stress field created by spherical inclusions. They concluded that relaxation strength and time would vary according to:

$$\Delta = \frac{\Delta^{(0)}}{1 + \frac{\pi dp}{4 l^2}} \quad \text{and} \quad \tau = \frac{\tau^{(0)}}{1 + \frac{\pi dp}{4 l^2}},$$

where $\Delta^{(0)}$ and $\tau^{(0)}$ denote the relaxation strength and time for particle-free grain boundaries, d and p the grain and particle size, and l the inter-particle spacing.

It is far more telling to rewrite the expressions given by Mori et al. like this:

$$\Delta = \frac{\Delta^{(0)}}{1 + \frac{\pi f d}{8 p}} \quad \text{and} \quad \tau = \frac{\tau^{(0)}}{1 + \frac{\pi f d}{8 p}}. \quad (5.5)$$

Here, f is the volume fraction of second phase and the following assumptions were made: the particles are distributed randomly throughout the entire grain (no preferential segregation at the boundary); only those particles are counted that are within a distance of $\frac{p}{2}$ from the boundary; the grain is, for the sake of argument, cubic, and the particles are distributed equidistantly over its surface $S = 6d^2$. From these expressions it is immediately clear that the smaller the particles, the lower the relaxation strength and time. Even for little volume fractions of second phase, a drastic decrease of the grain boundary peak is expected, as the ratio $\frac{d}{p}$ is generally huge. Preferential particle growth on boundaries would amplify this effect further.

Peters et al. have studied the grain boundary relaxation in the precipitation-hardenable copper–2 weight-% cobalt alloy, which forms cobalt-rich particles.^[Pe64]

Compared to pure copper, the peak exhibited the same broadening and similar activation energy, but its relaxation strength was smaller by a factor of 60. It had shifted to lower temperatures, which is also in accord with equation (5.5).

Similarly, Cao et al. found that the grain boundary peak in nickel–chromium completely disappeared (within the precision of the experiment) during the precipitation of grain boundary carbides, which were forming due to the presence of carbon impurities. The peak re-emerged after heating above the dissolution temperature of the second phase.^[Ca94]

To sum up, metals generally exhibit a grain boundary relaxation peak in the medium to high temperature range (above, very approximately, half the melting temperature). There is little reason to doubt its existence given the overwhelming experimental evidence, and even less so if one considers the most recent studies on aluminum bicrystals. (The peak was absent in a single crystal cut from the same grown product adjoining the bicrystals.^[Sh05]) Sliding proceeds in a viscous manner (though not necessarily Newtonian viscous), with threshold stresses, if any, so small that the forces put into play during mechanical spectroscopy are sufficient. The process is thermally activated, with an activation energy in the vicinity of the one for diffusion of a single atom. In metallic polycrystals, where grain boundary sliding should be accommodated predominantly by elastic deformation of the grains, the peak is characterized by its large broadening, a height fairly independent of grain size, and its shifting to higher temperatures (lower frequencies) during grain growth. The atomistic mechanism of the sliding process is not well understood as of yet. It is generally difficult to distinguish between competing models by means of mechanical spectroscopy alone, since they only differ in the prediction of just one observable, the activation energy. The relaxation can be impeded by a fine dispersion of second-phase particles on the grain boundary.

5.2 Grain boundary peak in 18-carat gold

Mechanical spectroscopy, by means of the forced, low-frequency, inverted torsion pendulum described in chapter 2, was performed on polycrystalline wire-shaped samples (50 mm in length, 2 mm in diameter) of white golds Au 5125 and Au 5130–1 as well as three alloys of the yellow gold series. Au 5130–1, not mentioned in chapter 1, is a modification of Au 5130 where the components indium and gallium were removed, produced for research purposes only. Measurements were carried out in vacuum better than 10^{-5} mbar.

Furthermore, single crystals of alloys Au 518, Au 5130, Au 5130–1 and Au 5210 were grown in our lab (50 mm in length, 2.5 mm in diameter), using the Bridgman technique. X-ray diffraction patterns confirmed that the specimens were indeed monocrystalline. All these single crystals' spectra showed only an increasing background, but no peaks at high temperature (see chapter 3), as expected for grain boundary related relaxation phenomena.

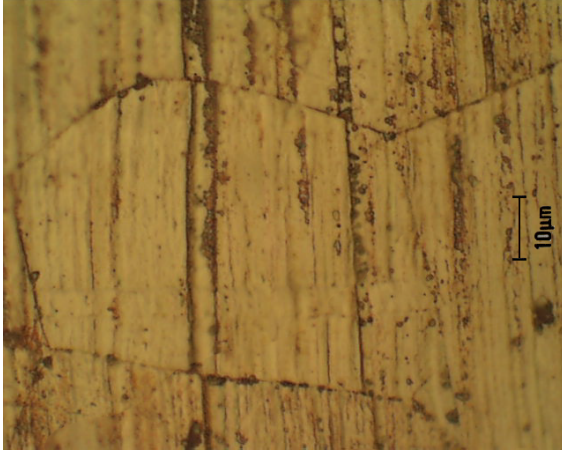


Figure 5.3: Discontinuous polishing scratch across a grain boundary after plastic deformation (twisting) of a Au 318 sample at 650 K.

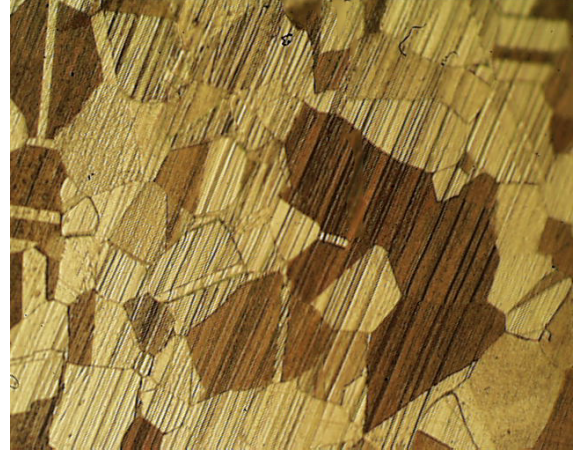


Figure 5.4: Grain structure and polishing scratches of a Au 318 sample after plastic deformation (twisting) at room temperature.

To further substantiate (though not prove) the claim that the high-temperature peak appearing in the gold alloys' mechanical loss spectra is indeed due to grain boundary *sliding*, a scratch mark test was conducted for Au 318. Two specimens were polished to such a degree that an appropriate number of scratches remained visible, then chemically etched to reveal the underlying grain structure. The first specimen was deformed at a temperature high enough to reasonably expect that grain boundary sliding would contribute to the plastic creep behavior. The second specimen was deformed at room temperature. Afterwards, both specimens were examined under an optical microscope. In the first specimen, some of the originally straight scratches now exhibited discontinuities at a grain boundary. An example is shown in figure 5.3. During careful examination of the cold-deformed specimen's scratch marks, figure 5.4, no such observation could be made. Despite the fact that, compared to mechanical spectroscopy, the sliding distances in such an experiment differ by several orders of magnitude, this is considered a direct macroscopic manifestation of grain boundary sliding.^[NB¹⁵]

In order to study the effect of different grain sizes on the grain boundary peak, a specimen of Au 5125 was annealed inside the pendulum at 1130 K. At this high a temperature, the grains grow at the expense of other grains. After one hour of annealing, the temperature spectrum was measured in cooling. This procedure was repeated several times. Figure 5.5 shows the resulting spectra. The grain boundary peak is seen to shift to higher temperatures, while its height and width change very little. The temperature shift implies that all relaxation times contributing to the broadened peak increase with grain size. This is exactly the behavior expected for grain boundary sliding accommodated by elastic deformation of the grains.

The trend was observed in other alloys as well, such as the yellow gold Au 3418 and the white gold Au 5130-1. However, the majority of measurements were made up to temperatures no more than 1000 K in white gold, and no more than

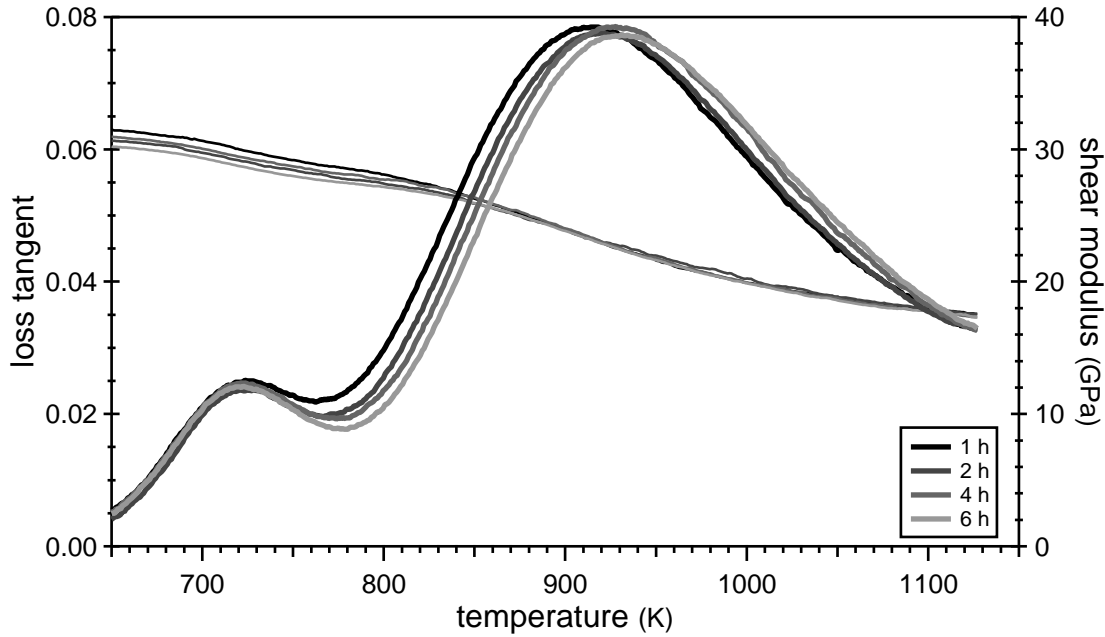


Figure 5.5: Shift of the grain boundary peak in Au 5125 due to grain growth induced by long annealing treatments at 1130 K. The total annealing time is given. While the position of the peak changes, its height does not. The Zener peak, at low temperatures, remains unaffected.

900 K in yellow gold. It can be inferred that below these temperatures grain growth is negligible in most cases. Au 3418 appears to be an exception, where a shift of the grain boundary peak occurred already between heating and cooling in the first thermal cycle to 900 K. In principle, a systematic study of the grain boundary peak in a given alloy can provide information on the onset and magnitude of grain growth at various annealing temperatures, which is of practical importance with regard to the alloy's metallurgy.

From the measurements in figure 5.5 alone, the grain size exponent m , defined by $\tau \propto d^m$, cannot be deduced, as the evolution of d with annealing time is unknown, as well as the final grain size. Mechanical spectroscopy has to be accompanied by a microstructural study that determines d directly. A linear fit of $\frac{1}{T}$, where T is the temperature of the peak maximum, versus $\ln d$ then yields m , since it can be shown that:

$$\frac{1}{T} = \text{const} - m \frac{k}{H} \ln d.$$

The activation enthalpy H of the grain boundary peak has to be known beforehand, k is the Boltzmann constant. The quality of the result depends sensitively on the accuracy of the temperature measurement, which may easily incur a systematic error when the specimen is mounted in the pendulum.² Unfortunately,

²For example, if one changes, albeit slightly, the position of sample or temperature sensor. It is generally tricky to measure the precise sample temperature during mechanical spectroscopy in vacuum since the specimen is moving and any direct contact that might cause non-internal friction has to be avoided. As opposed to isothermal conditions, corrections for temperature spectra are further complicated by the non-stationary temperature field inside the instrument.

but apparently for that reason, a (very limited) study conducted in our lab on a Au5130–1 specimen grown to three different grain sizes (30 μm , 100 μm and 200 μm) gave inconclusive results: the peak shifted first with $m = 1$, consistent with elastic accommodation, but the second shift indicated m larger than 2.

The grain boundary peak is fairly broad, in agreement with findings for other metals and alloys reviewed in the previous section. The broadening can be readily observed in the isothermal spectra, figure 5.6 for Au 5125 and figure 5.7 for Au 5130–1, where the peak obviously spans more decades than a pure Debye peak would.

Arrhenius plots yield the activation parameters, displayed on the same respective figures. In white gold, the activation enthalpy is generally higher than the one of the Zener relaxation: in Au 5125, for instance, the difference is 0.3 eV (compare with figure 4.22 on page 72). In yellow gold, however, 2.4 eV (Au 318), 2.2 eV (Au 3418, Au 418) and 2.1 eV (Au 518) were measured, with limit relaxation times all near 10^{-17} s. These energies are close to or, in the case of Au 518, below the ones for the Zener relaxation (see table 4.1, page 67). However, it was noted that the proximity of the order–disorder transition seems to lead to an apparent increase of the values measured for the Zener peak in yellow gold.

In order to perform fits of the grain boundary peak, the high-temperature background, which appears in all spectra, must first be taken into consideration. As will be argued in section 5.4, it is due to dislocation relaxations. Schoeck^[Sc64] has derived the following expression for such a mechanism:

$$F_{\text{bg}}(\omega, T) = \frac{K}{\omega^n} \exp\left(-n \frac{H_{\text{bg}}}{kT}\right). \quad (5.6)$$

H_{bg} is the activation energy of the rate-controlling process that governs the motion of dislocations, such as the interaction with point defects, K and n are essentially constant over limited ranges of temperature. For temperature spectra measured in a forced torsion pendulum, ω is constant and expression 5.6 boils down to the very common exponential background. This was generally observed to be a good approximation of the high-temperature mechanical loss in all gold alloys (as it is in many other materials too^[Q3.5]). It also proved convincing in fits to frequency spectra, though, sometimes, when due to the limited frequency range little information on the (low-frequency) background was available, a constant background level was used instead. In these rare cases, the frequency-independent offset was taken to be equal to the exponential background level at the same temperature as observed in the temperature spectrum of the sample.

Using the activation energy from the Arrhenius plots, the grain boundary peaks in the temperature mechanical loss spectrum of several alloys were fitted to a broadened Debye peak. During the fitting procedure, the limit relaxation time τ_0 was allowed to deviate slightly from the Arrhenius plot's result to accommodate inaccuracies of the temperature reference on the one hand, and changes in grain size (or differences, in cases where another specimen was used) on the other. Results are shown in figures 5.8 and 5.9 for the white golds Au 5125 and Au 5130–1,

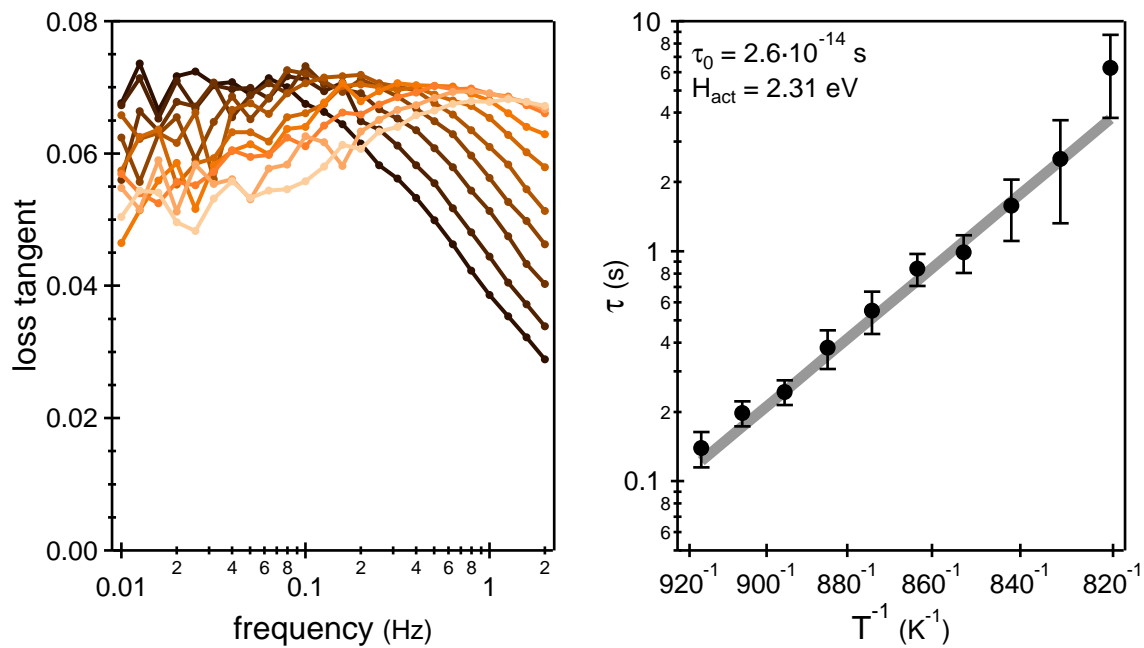


Figure 5.6: Grain boundary peak in isothermal conditions and corresponding Arrhenius plot for Au 5125.

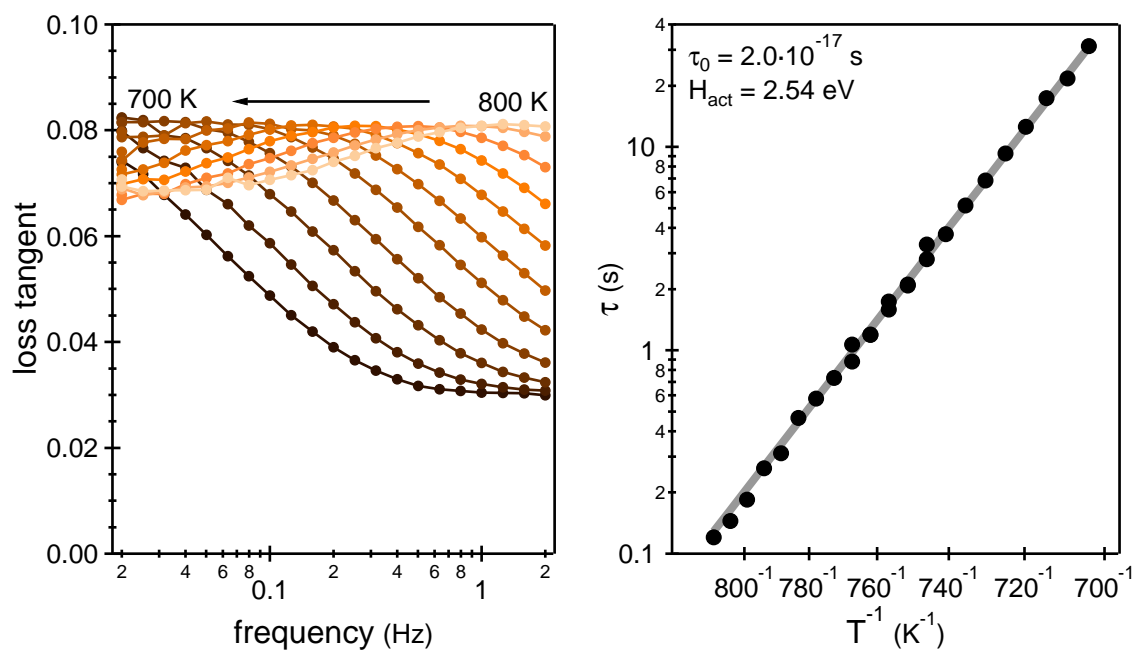


Figure 5.7: Grain boundary peak in isothermal conditions and corresponding Arrhenius plot for Au 5130-1. (To establish the Arrhenius plot, some curves not depicted on the left graph were used.)

as well as in figures 5.10 and 5.11 for the yellow golds Au 318 and Au 518. Furthermore, figures 5.12 and 5.13 show fits to the peak in isothermal conditions for alloys Au 3418 and Au 518.

It can be said without exaggeration that the quality of the fits is excellent. Minor deviations only occur in Au 5130–1 (figure 5.9) where the background is fairly high, as well as in Au 518 (figure 5.11) where the Zener peak, that had to be included in every case in order to accurately fit the low-temperature flank of the grain boundary peak, was assumed to have a regular broadened Debye shape, despite the fact that it is cut off by the order–disorder transition.

Thanks to these fits, the broadening can now be quantified. The log-normal distribution parameter of relaxation times, β , was never found below 3 and reached values as high as 5, depending on the alloy and, arguably, the actual grain structure of the specimen. There is some inconsistency in the determination of β between the temperature and frequency spectra: for the sample of Au 518 (which was never heated to more than 800 K, so the effect on grain structure is expected to be minimal), the two fits gave values that differ by 0.3, compare figures 5.11 and 5.13. In general, the range of β agrees with values reported in literature for grain boundary peaks of various other metals.

The peak appears at different temperatures in each spectrum, from as low as 700 K in Au 518, to 800 K in Au 5130–1 and even more than 900 K in Au 5125. The latter specimen was the one subject to grain growth for the measurements presented earlier, in figure 5.5. This explains the higher peak position compared to the Au 5130–1 spectrum, where an as-received specimen of finer grain structure ($d \approx 30 \mu\text{m}$) was used. Generally, like the Zener peak, the grain boundary peak in white gold tends to be higher in temperature than in the yellow gold series. As argued at the end of chapter 4, this should be attributed to the presence of palladium in the matrix, which not only increases the alloys' melting point but generally slows diffusion. The trend is a little less pronounced in the case of the grain boundary peak, which is therefore closer to the Zener peak in fine-grained specimen such as the Au 5130–1 sample of figure 5.9. However, in terms of height and shape, the peaks resemble each other a great deal in all gold alloys studied. This is even true for gold-rich Au–Cu, which is shown as an illustrative example in figure 5.14.

There may be a correlation between broadening and peak temperature: larger β values were found whenever the peak was lower in temperature. For white gold this can be seen by comparing the fit results of the temperature spectra in figures 5.8 and 5.9, for yellow gold by comparing the fits to the frequency spectra of figures 5.12 and 5.13. Further proof for the existence of such a trend is provided by the spectra recorded over the course of the grain growth treatments in Au 5125 (figure 5.5). The broadening parameter β was determined for the individual curves and is reported in figure 5.15 as a function of the (shifting) peak temperature (due to increasing grain sizes). Error bars indicate the standard deviation of β as estimated from the quality of the least-squares fit. Clearly, β decreases with peak temperature, i.e. the peak becomes narrower while the

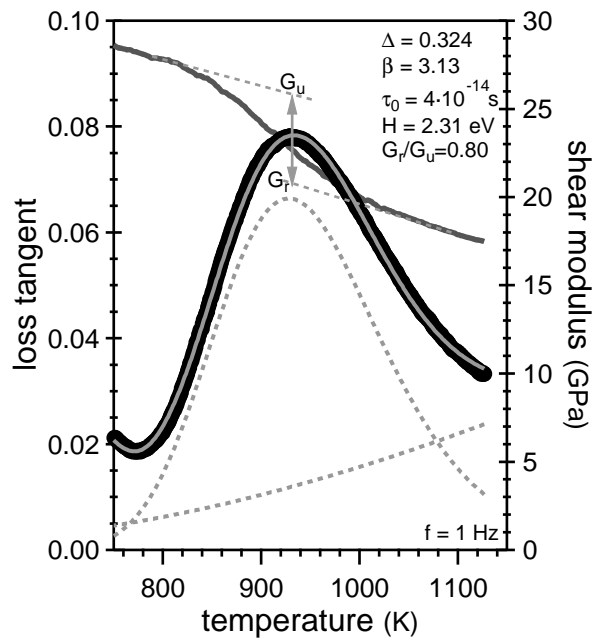


Figure 5.8: Fit of Au 5125's grain boundary peak in the mechanical loss temperature spectrum.

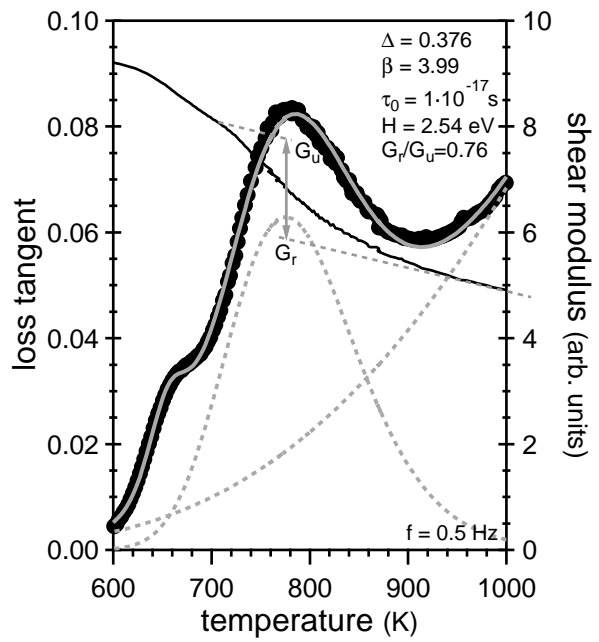


Figure 5.9: Fit of Au 5130-1's grain boundary peak in the mechanical loss temperature spectrum.

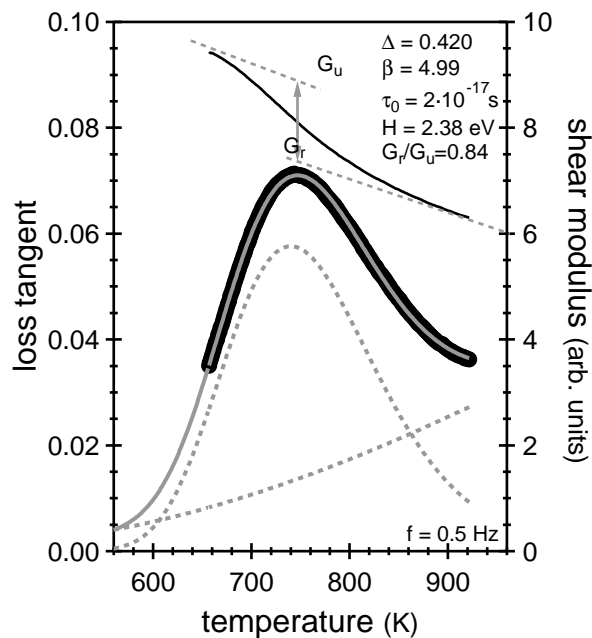


Figure 5.10: Fit of Au 318's grain boundary peak in the mechanical loss temperature spectrum.

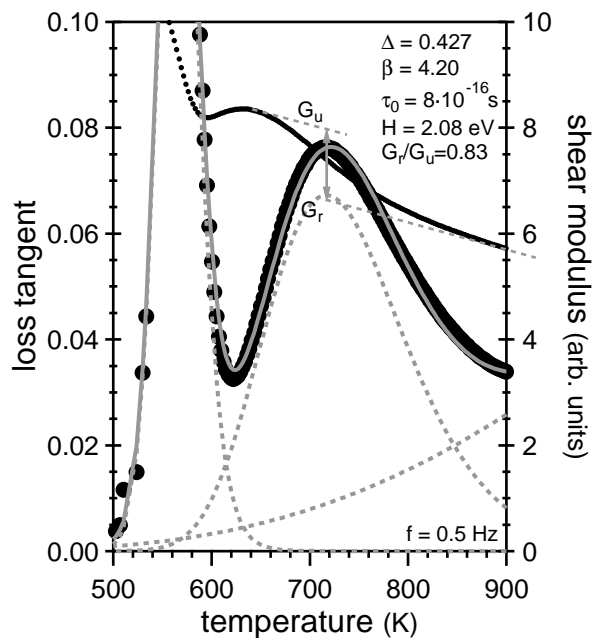


Figure 5.11: Fit of Au 518's grain boundary peak in the mechanical loss temperature spectrum.

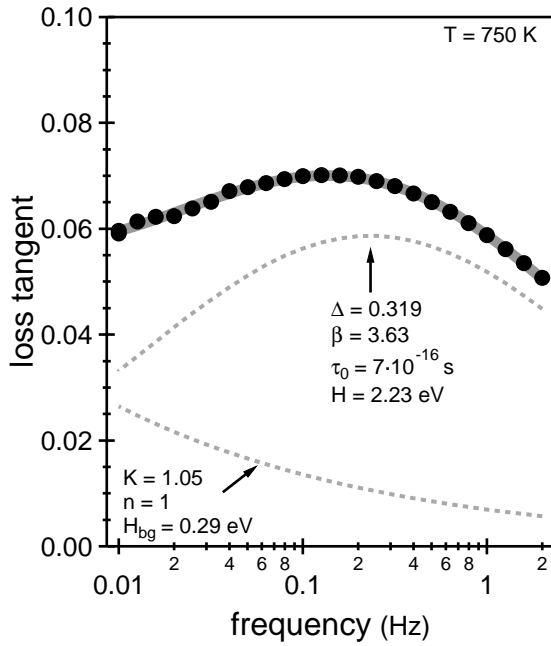


Figure 5.12: Fit of Au 3418's grain boundary peak in the mechanical loss frequency spectrum to a broadened Debye peak on a high-temperature background.

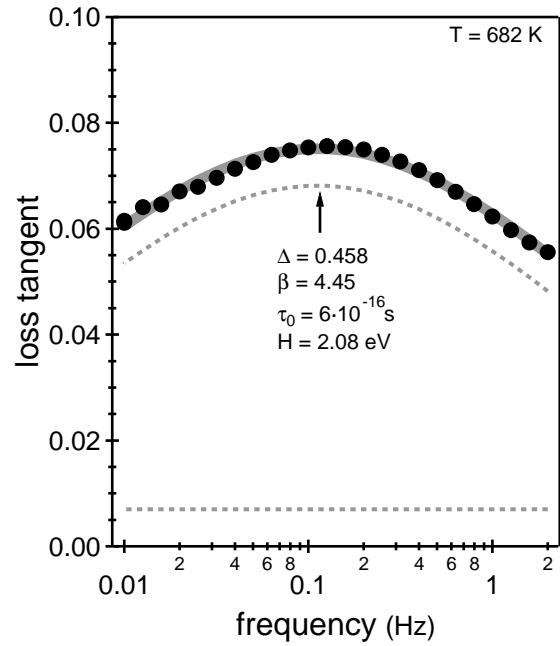


Figure 5.13: Fit of Au 518's grain boundary peak in the mechanical loss frequency spectrum to a broadened Debye peak on a constant background.

grains grow. If the trend observed on figure 5.15 were extrapolated linearly, β would vary by, roughly, 0.8 over 100 K. A variation of this magnitude would explain the different broadening parameters among the various gold alloys.

It shall not be overlooked that β has a temperature dependence by virtue of its definition. Consider the fraction of β that stems from the distribution of activation enthalpies involved in the relaxation process, i.e the fraction that is not accounted for by the grain size distribution. Using $\Delta\tau = 2\beta$ as a measure of the relaxation times' width of log-normal distribution³, one has $\Delta H = 2kT\beta$ due to the Arrhenius equation (2.14). If the contributing activation enthalpies do not change, then ΔH is constant and β would decrease with temperature like $\frac{1}{T}$. However, this effect is far too small to account for figure 5.15.

Therefore it stands to reason that, as the grains grow, the distribution of activation energies narrows. This makes sense if one recalls that, during grain growth, the most mobile grain boundaries migrate and consume neighboring grains. It is therefore conceivable that the process eliminates certain types of boundaries and selects others that, consequently, resemble one another in structure and thus require similar energies to activate sliding. (A caveat to this interpretation may be the possible existence of coupling effects, discussed at the end of this section.)

Another fitting parameter that correlates with β is the relaxation strength, Δ . It is smallest in Au 5125, about 0.32 for the relatively narrow peak of $\beta \approx 3$ (fig-

³See equation (2.16) on page 25: $\text{erf}(1) = 84\%$ of all τ are within $\pm\beta$ of τ_m .

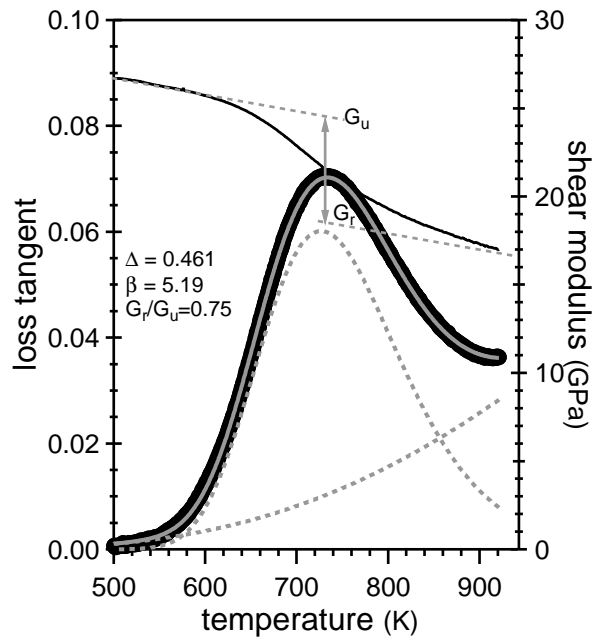


Figure 5.14: Fit of the grain boundary peak in $\text{Au}_{92\%}\text{Cu}_{8\%}$ to a broadened Debye peak superimposed on an exponential background.

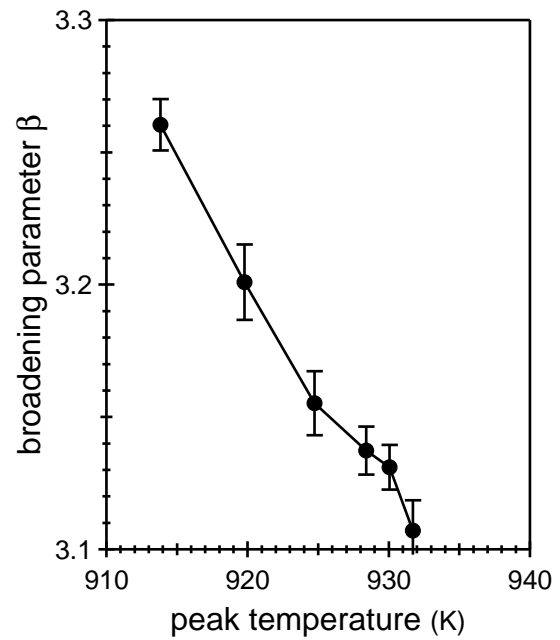


Figure 5.15: Broadening parameter β of the grain boundary peak as a function of the shifting peak temperature during grain growth in Au 5125. The β values were obtained from fits to the spectra in figure 5.5.

ure 5.8), and reaches values of 0.42 or even more for some of the peaks with $\beta > 4$. The correlation as such is not surprising at all: it is a simple consequence of the easily observable fact that the grain boundary peak is of similar height in all 18-carat gold alloys — between 0.06 and 0.07 if the background estimation is correct. Indeed, as a Debye peak broadens, its height decreases (see equation (2.17), page 26). Conversely, if two peaks of the same height differ in width, then the broader peak must be due to a stronger relaxation (the “pure” Debye peak) to begin with.

The real question that arises is this: How can one explain the magnitude of the relaxation strength, as well as the fact that it varies by as much as 30% and more from alloy to alloy?

We first note that a relaxation strength of 0.4 is much higher than predicted by the continuum model of elastically accommodated grain boundary sliding, see Ghahremani/Fotiu’s result plotted in figure 5.2. As for the alloys’ Poisson’s ratio (at peak temperature), $\nu = 0.4$ should be a good enough estimate, based on the room-temperature Poisson’s ratios of gold (0.44), palladium (0.39), silver (0.37) and copper (0.34). Equation (5.3) then yields a modulus ratio of $\frac{G_r}{G_u} = 0.837$ which, as per equation (5.2), corresponds to a relaxation strength of $\Delta = 0.195$ — less than half of some of the values observed.

Mechanical spectroscopy provides a second, direct measurement of the modulus ratio from the relative drop-off of the dynamic modulus curve before and after the relaxation. This is indicated on all temperature spectra on page 89 (figures 5.8

to 5.11). It requires an extrapolation of the modulus's decline with temperature that is unrelated to the relaxation (due, chiefly, to thermal dilatation), which introduces some error (even more so when the Zener peak is close). The directly measured values of the modulus ratio are all in the vicinity of 0.8 and vary by no more than 10% from alloy to alloy. They are thus much closer to the model prediction than the relaxation strength, particularly for the two yellow golds Au 318 and Au 518 (figures 5.10 and 5.11).

One is therefore led to question the validity of the approach chosen here: to model the grain boundary relaxation process as a standard anelastic solid. After all, the directly measured modulus ratio is an undeniable experimental fact. An overestimation of β would then explain the excessive values obtained for the relaxation strength. This lends credence to the findings of Shi et al. in aluminum bicrystals, where a single non-Debye relaxation would well describe the otherwise broadened peak. As these authors pointed out, the coupling analysis cannot be simply applied to polycrystals.^[Sh06,Ko09] In polycrystals, two effects would overlap: the variation of activation energy among grain boundaries, as well as that of the coupling parameter n . It is not clear how n is distributed and if and how the two distributions are correlated. For example, the decrease of β with temperature, discussed further above, could also be a result of differences in coupling.

In conclusion, the high-temperature peak found in 18-carat gold alloys has the characteristics of a relaxation due to grain boundary sliding that is primarily accommodated by elastic deformation of the grains. It is associated with activation energies that are generally higher than for self-diffusion in the bulk material.

5.3 Precipitates blocking grain boundary sliding

Three of the commercially used white gold alloys investigated in this study — Au 5130, Au 8150 and Au 5210 — contain indium and gallium additives. Instead of the single grain boundary peak, these alloys exhibit what appears to be a double peak at high temperature. For Au 5130, the high-temperature part of the mechanical loss spectrum is shown in figure 5.16 at various heating/cooling rates \dot{T} .

The spectra measured in cooling can be understood in the following way: At high temperature, all alloy constituents form a solid solution. Initially, during cooling, the grain boundary peak manifests itself in the spectrum. Then, below some critical temperature, a second phase becomes thermodynamically stable. The alloy undergoes a phase transformation (a phase separation) as particles precipitate from the matrix. Some of the particles happen to grow across grain boundaries (or may even do so preferentially), which reduces the relaxation strength of grain boundary sliding. Evidently, the particles are dispersed fine enough to make the grain boundary peak vanish entirely, leaving only the background (within the precision of this experiment).

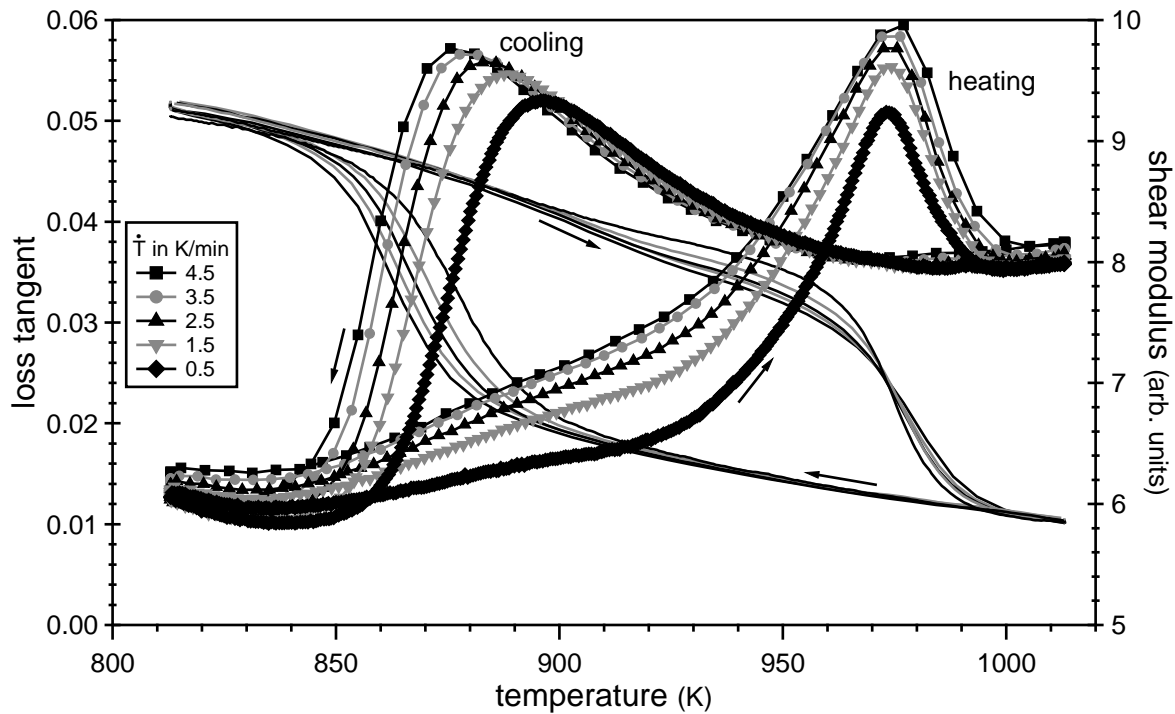


Figure 5.16: High-temperature part of Au 5130's mechanical loss spectrum at various heating/cooling rates: the grain boundary peak disappears/reappears during precipitation/dissolution of grain boundary particles.

The lower the cooling rate, the higher is the temperature at which the peak disappears. This is only logical because cooling at a slow rate leaves the particles more time to grow, so that the blocking of grain boundaries sets in at a higher temperature despite the driving force for precipitation being relatively low. If one cools quickly, the grain boundary peak is retraced further in temperature before enough particles have formed to effectively block sliding. Parallel to the peak's breakdown, the modulus increases to the unrelaxed value corresponding to nearly rigid grain boundaries.

Thus far, the interpretation of the high-temperature hysteresis in white gold is identical to the one originally provided by Cao et al. to explain the spectrum of Ni-Cr.^[Ca94] Indeed, the similarities are manifold. As an example, compare the temperature spectra of Ni-Cr in figure 5.17 and Au 5210 in 5.18, both measured at varying excitation frequencies. The effect one observes is this: The higher the frequency, the further the grain boundary peak shifts up in temperature, which means that a smaller part of the peak is cut off due to precipitation. Consequently, the peak appears larger, though its true height does not change.

Differences with respect to Ni-Cr are found in the heating curves of figure 5.16 for Au 5130. During heating, above the critical temperature, the grain boundary peak re-appears as more and more particles go back into solution. However, as opposed to cooling, the process is superimposed by a transient loss which produces an additional, more complicated temperature dependence of the spectrum. The transient component of the mechanical loss must be due to changes in the microstructure, induced by the rise in temperature, that couple to the applied

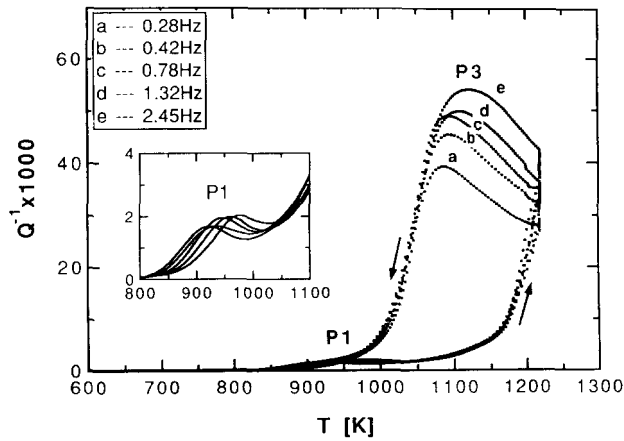


Figure 5.17: Effect of the frequency on the grain boundary peaked blocked by carbides in $\text{Ni}_{80}\text{Cr}_{20}\%$, reproduced from reference Ca94.

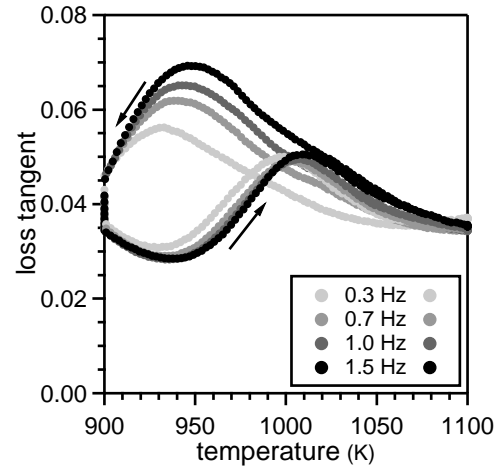


Figure 5.18: Effect of the frequency on the grain boundary peak blocked by precipitates in Au 5210.

stress. It therefore increases with the heating rate \dot{T} (figure 5.16), but decreases with excitation frequency (figure 5.18), i.e. for shorter stress cycles.

In fact, if there was no transient damping, the sequence of the curves for different heating rates should be reversed. Instead, the mechanical loss at the lowest heating rate (when the material evolves closer to equilibrium) trails all other curves. The transient component is obviously responsible for the “overshoot” of the mechanical loss with respect to the grain boundary peak: after each heating, this part does not appear in the subsequent cooling curve.

The overall modulus defect is the same for all heating rates since, eventually, the transient component fades out, leaving only the relaxed value of the grain boundary peak. All modulus curves intersect at about 975 K: the lowest heating rate corresponds to the most abrupt change. This, too, should be a consequence of the transient damping: it produces a “temporary” modulus defect at fast rates which, after the intersection, is compensated by a lower fraction of dissolved precipitates (similar to the retardation in cooling), i.e. less grain boundary sliding.

Since the blocking of grain boundary sliding occurs only in alloys containing indium and gallium, the second phase or phases must contain one or both of these elements. The quantity of indium and gallium contained in the alloys, atom fractions of at least 1% each, explains easily the complete breakdown of the grain boundary peak, as discussed in connection with equation (5.5) (page 82). The volume fraction of second phase might be even much higher, depending on its composition.

In an effort to elucidate the influence of composition on the observed phenomenon, modifications of Au 5130 and Au 5210 were produced (see section 3.2). For the alloy designated Au 5130-1, none of the two additives were added to the melt. Au 5130-2 and Au 5210-2 only contain the indium part, Au 5130-3 only gallium.

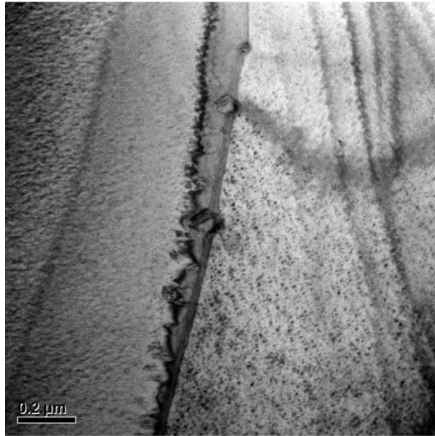


Figure 5.19: TEM micrograph of grain boundary precipitates in a polycrystalline Au 5130 sample.

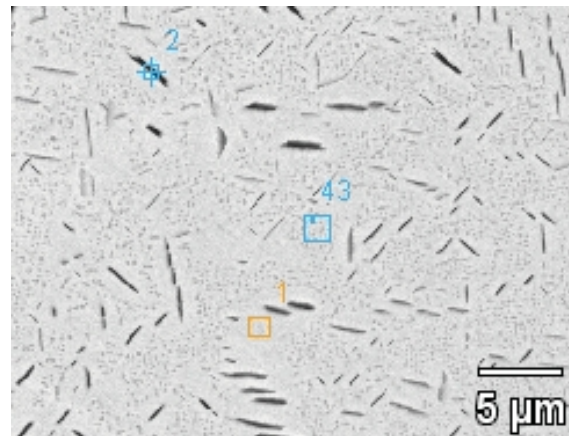


Figure 5.20: SEM micrograph of large precipitates in a Au 5130 single crystal; markers indicate target regions of EDX chemical analysis.

As expected, no second phase formed in Au 5130–1, leaving the grain boundary peak perfectly intact (see figure 3.13 on page 44). Au 5130–1 was therefore included in the investigation of the previous section. The spectra of the other two Au 5130 modifications showed the same characteristic feature as Au 5130, indicating blocked grain boundaries (figure 3.14, page 45). Therefore, indium or gallium may each individually stabilize a second phase in the Au–Cu–Pd based alloy Au 5130.

In the Au–Pd based Au 5210–2 (figure 3.15, page 45), indium alone did not produce the desired effect: the mechanical loss spectrum shows the large grain boundary peak, without any hysteresis between heating and cooling. The alloy would not harden during aging. Apparently, indium requires copper to be present in the matrix to form a stable second phase. However, it shall be noted that, only in this alloy, the shape of the grain boundary peak deviates markedly from a (broadened) Debye peak, as fits like those performed in the previous section clearly revealed.

Subsequent to the findings obtained by mechanical spectroscopy, electron microscopy (SEM and TEM) in connection with EDX chemical analysis (performed by co-workers) confirmed the presence of second-phase particles inside the grains and on grain boundaries of Au 5130, see micrographs in figures 5.19 and 5.20.^[Tk09] Palladium concentrations correlated with gallium, indicating (with considerable error) a phase composition near the stoichiometry Pd₂Ga. In the Au 5130 single crystal, higher concentrations of the gallium-rich precipitates were found in proximity of the free surface, as opposed to the bulk. Indium-rich precipitates have not been identified (so far).

The precipitation/dissolution transition was studied in isothermal conditions as well: once more in alloy Au 5130, figure 5.21, and in Au 5130–2, figure 5.22.

Figure 5.21a shows the frequency spectra of Au 5130 recorded at stepwise low-

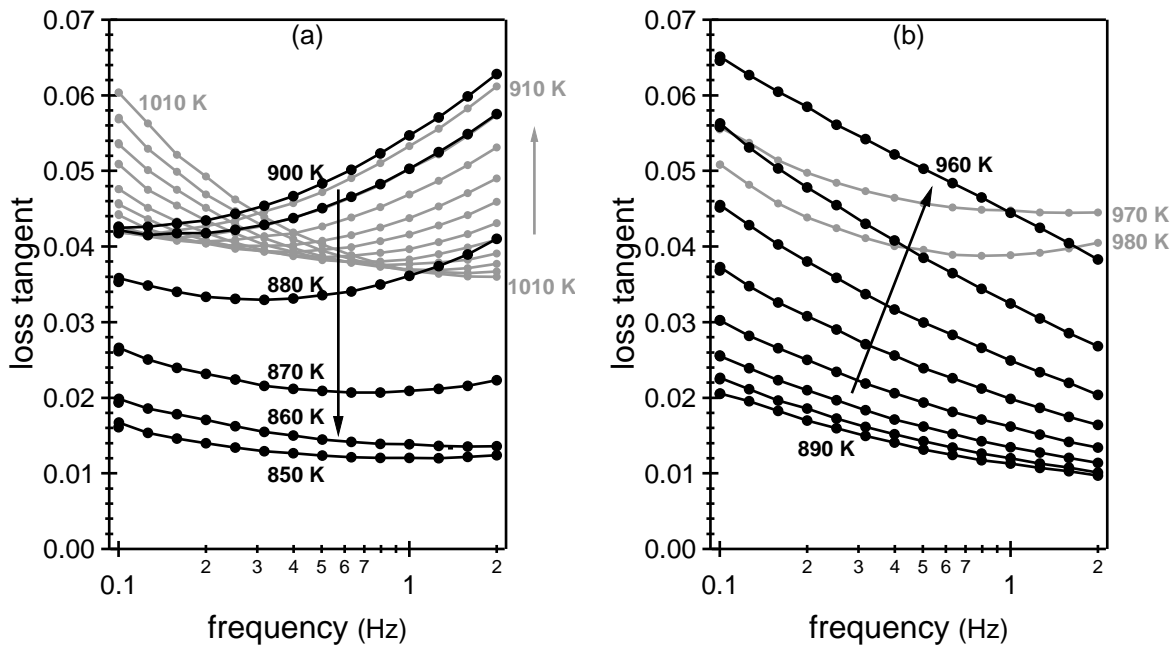


Figure 5.21: Mechanical loss frequency spectra of Au 5130 in isothermal conditions at selected temperatures (steps of 10 K between curves) near the precipitation/dissolution temperature of the second phase: (a) stepwise decreasing temperature (cooling); (b) stepwise increasing temperature (heating).

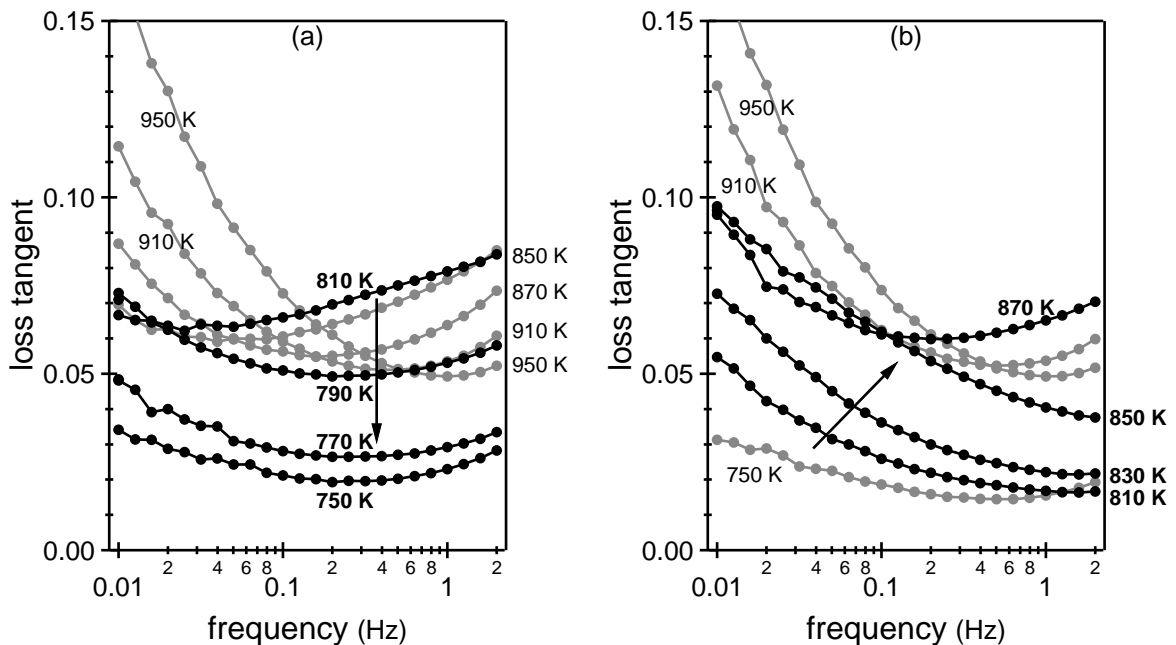


Figure 5.22: Mechanical loss frequency spectra of Au 5130-2 in isothermal conditions at selected temperatures near the precipitation/dissolution temperature of the second phase: (a) decreasing temperature steps (cooling); (b) increasing temperature steps (heating).

ered temperatures. Consider first the spectrum at 1010 K. It is entirely due to the high-temperature background which, so far, we have mostly observed in the temperature spectra as the exponential increase towards the melting point. The background is obviously thermally activated: as the temperature is lowered, it progressively disappears at the low-frequency end.

On the opposite side, the grain boundary peak advances into the frequency window. Below 900 K, the peak becomes unstable and gradually breaks down as more and more second-phase particles precipitate and pin grain boundaries. Actually, the decrease in peak height is not as obvious as the figure suggests. Rather, the peak is seen to shift *back* to high frequency — contrary to the trend imposed by thermal activation. Such a shift is proof that the relaxation time decreases, in agreement with the model by Mori et al., see equation (5.5). The height must shrink as well to explain the observed breakdown in the temperature spectrum, since a shorter relaxation time (higher peak frequency) corresponds to a lower peak temperature.

In figure 5.21b, measured in stepwise heating, the mechanical loss is seen to increase drastically above about 900 K. This temperature is thus critical for the phase transition, i.e. the precipitation/dissolution of particles. Even in isothermal conditions the transient damping affects the mechanical loss spectra. The time delay (of only 10 minutes), imposed during this experiment after each heating step to the next temperature, was obviously not sufficient to equilibrate the microstructure. The “overshoot” registered in the temperature spectra is recognizable in the frequency spectrum at 960 K. After that, the mechanical loss settles at values corresponding to the equilibrated structure: at 980 K, one clearly distinguishes part of the grain boundary peak, superimposed on the low-frequency/high-temperature background.

The isothermal spectra of the gallium-free Au 5130–2 in figure 5.22 show the same characteristic features, with only the following two differences: the precipitation temperature is about 90 K lower, and the effect of the transient damping is less pronounced. The same observations were made in Au 5130–2’s temperature spectrum (at $f = 0.5$ Hz): the grain boundary peak reaches almost its full height before it breaks down, while the transient overshoot occurs much more discreetly. Note, however, that *partly* the differences in transient mechanical loss between the isothermal spectra of the two alloys are due to the smaller frequency range chosen for the Au 5130 experiment. Those spectra could therefore be measured only 54 minutes apart, as opposed to 115 minutes (including a 20-minute delay) for Au 5130–2. All isothermal frequency sweeps ran from high to low frequency.

Regarding the low-frequency background, one could easily jump to the conclusion that its level decreases along with the breakdown of the grain boundary peak. This, however, would be premature. Its progressive decline or rise in the respective series of frequency spectra, as important as each may appear, is rather well accounted for by the background’s exponential temperature de-

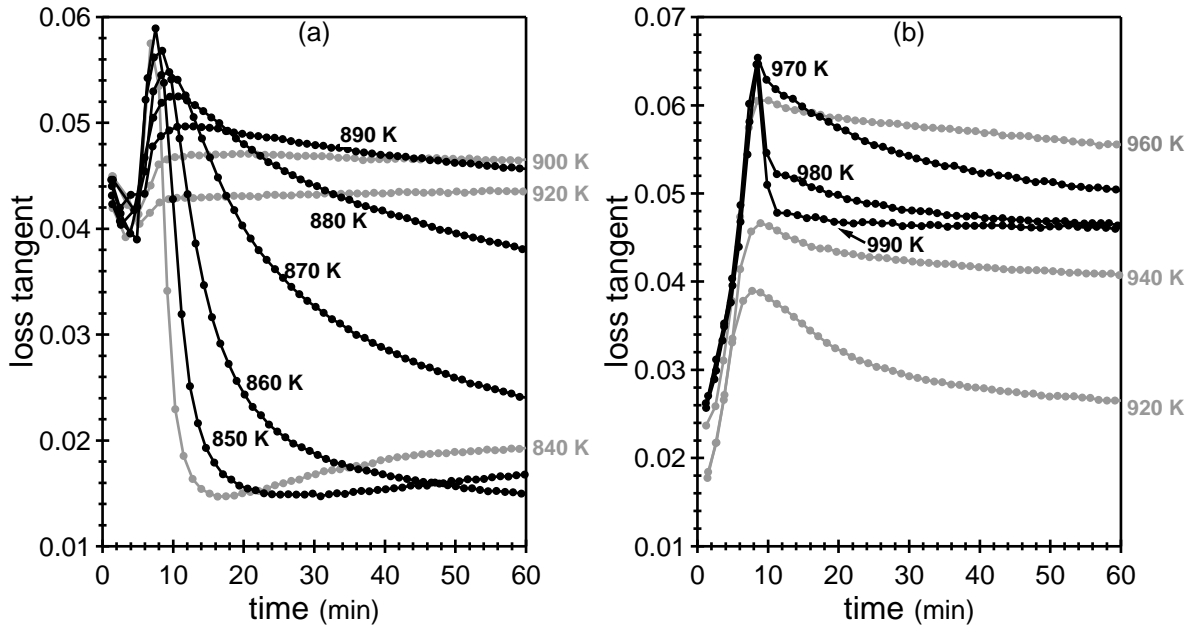


Figure 5.23: Evolution of the mechanical loss (at 0.5 Hz) with time in Au 5130: (a) after quick cooling from the solid solution; (b) after quick heating from below the second phase's dissolution temperature.

pendence. On the other hand, due to the limited frequency range, a change of background damping can also not be excluded.

Figure 5.23 provides insight into the kinetics of the phase transformation. In figure 5.23a, a Au 5130 specimen was quickly cooled from the solid solution to temperatures below the critical temperature of phase stability (which is about 900 K). The mechanical loss decreases, following the breakdown of the grain boundary peak as sliding is gradually blocked by particles precipitating at grain boundaries. At 840 K, the transformation time was as short as a few minutes. It proved technically impossible to measure the specimen at a cooling rate high enough to observe the precipitation process slow down. Such quick cooling can only be achieved externally, by quenching. Based on the results from mechanical spectroscopy, one can thus not say with certainty where in temperature the “nose” of the phase transformation's TTT diagram is situated.

In figure 5.23b, another Au 5130 sample was heated, as fast as the pendulum's furnace would allow, from 830 K to a target temperature above 900 K. The transient damping dominates all measured curves: apart from the initial ten minutes of quick heating (or its aftereffects), the mechanical loss never increases over time as one would expect during the resurgence of the grain boundary peak. Below 970 K, the loss level would not stabilize over the course of the one-hour experiment. Note in particular the slow but steady decline of the high transient damping at 960 K, which explains the isothermal spectrum of figure 5.21b at the same temperature. Above 970 K, the temporal decline of the transient loss accelerates markedly. At 990 K, the microstructure stabilizes extremely fast.

These observations warrant the hypothesis that the transient damping is cou-

pled to the process of particle dissolution. The following scenario would then explain the observed behavior: Above the critical temperature, of about 900 K, the second phase becomes metastable and particles begin to dissolve. Above 970 K, the second phase becomes unstable, i.e. the energy barrier for the phase transformation goes to zero. The dissolution of particles therefore accelerates and equilibrium is reached quickly. When all particles have disappeared, the transient damping ceases.

It was noted earlier that the magnitude of the transient damping varies from alloy to alloy. It appears to be strongest in Au 5130, which is why it featured so prominently even in the isothermal spectra. As opposed to Au 5130, the mechanical loss's characteristic overshoot in heating does not occur in the temperature spectrum of Au 5210 whenever the heating rate is very low (0.1 K) or the frequency relatively high (see figure 5.18 for that matter), i.e. for low $\frac{\dot{T}}{\omega}$.

The microscopic origin of the transient damping remains unclear. Spectra very similar to the one of figure 5.16 were observed in Al–Ag and the transient loss attributed to a stress-coupled shape change of bulk precipitates during heating and cooling.^[K186] This does not seem to be the case here. Rather, the transient damping appears to originate from the shearing of grain boundary inclusions during dissolution. This assertion is founded on the observation that the spectrum of the Au 5130 single crystal (figure 3.16, page 46) does not exhibit the prominent peak of the transient component in heating. Should the transient loss indeed be caused by grain boundary precipitates, then a higher level among similar alloys, as is the case for Au 5130 compared to the gallium-free Au 5130–2, might indicate a preferential formation of particles at grain boundaries. This is of practical concern as such a microstructure is prone to grain boundary embrittlement.

5.4 Precipitation hardening in white gold

Grain boundary sliding occurs at high temperature, 700 K and more in 18-carat gold alloys. The fact that precipitates block the grain boundaries can therefore not explain the age-hardenability of white gold alloys (that is, of those that form a second phase) since sliding does not contribute to room-temperature plasticity, which is what a hardness test measures.

At room temperature, deformation is mediated by the motion of dislocations through the material, or, more precisely, through the individual grains. If second-phase particles precipitate inside the grains (not just on grain boundaries) and if, by doing so, they decrease the mobility of dislocations (pin them), they would effectively be the cause of the hardening mechanism in these materials.

First of all, hardening does indeed occur inside the grains, as the comparative Vickers hardness tests on mono- and polycrystalline samples summarized in table 5.1 testify. Within the precision of these measurements, one concludes that the boundary-free single crystal hardens as much the multi-grained material

alloy	polycrystal		monocrystal	
	ductile	hardened	ductile	hardened
Au 5130-1 (—)	130	130	145	140
Au 5130-2 (In)	135	205	150	200
Au 5130-3 (Ga)	145	190	165	200
Au 5130 (In+Ga)	160	230	160	210

Table 5.1: Vickers hardness of poly- and monocrystals of the Au 5130 modifications in the ductile, solution-treated state as well as in the age-hardened state.

hardening temperature	micro-hardness (GPa)
400°C	3.08 ± 0.11
450°C	3.37 ± 0.13
500°C	3.45 ± 0.12
750°C	3.04 ± 0.11

Table 5.2: Average micro-hardness and its standard deviation based on 12 micrometer-sized indentations each, placed inside the grain as well as close to grain boundaries in four Au 5130 samples subjected to different age-hardening treatments.

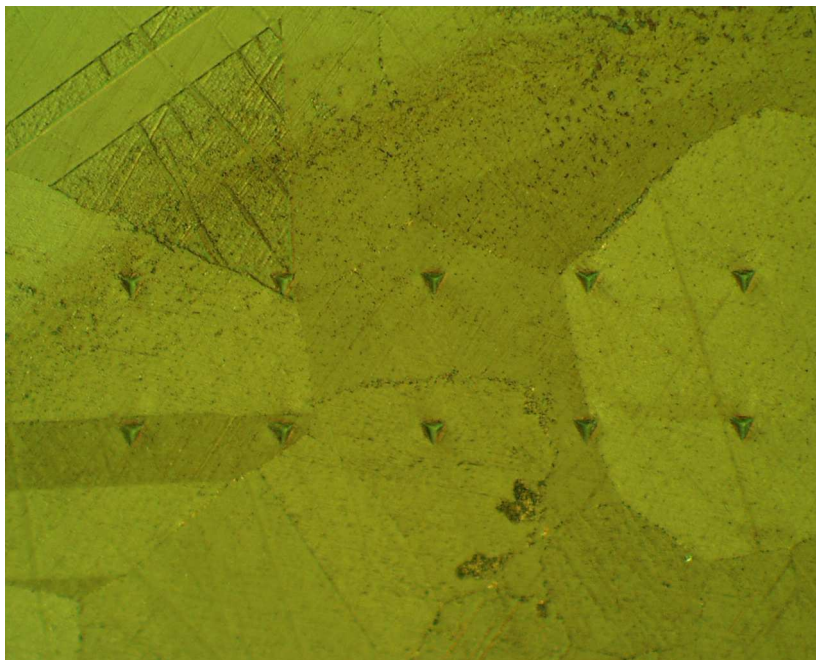


Figure 5.24: Optical micrograph of a series of 12 micrometer-sized indentations on the Au 5130 specimen aged at 500 °C listed in table 5.2.

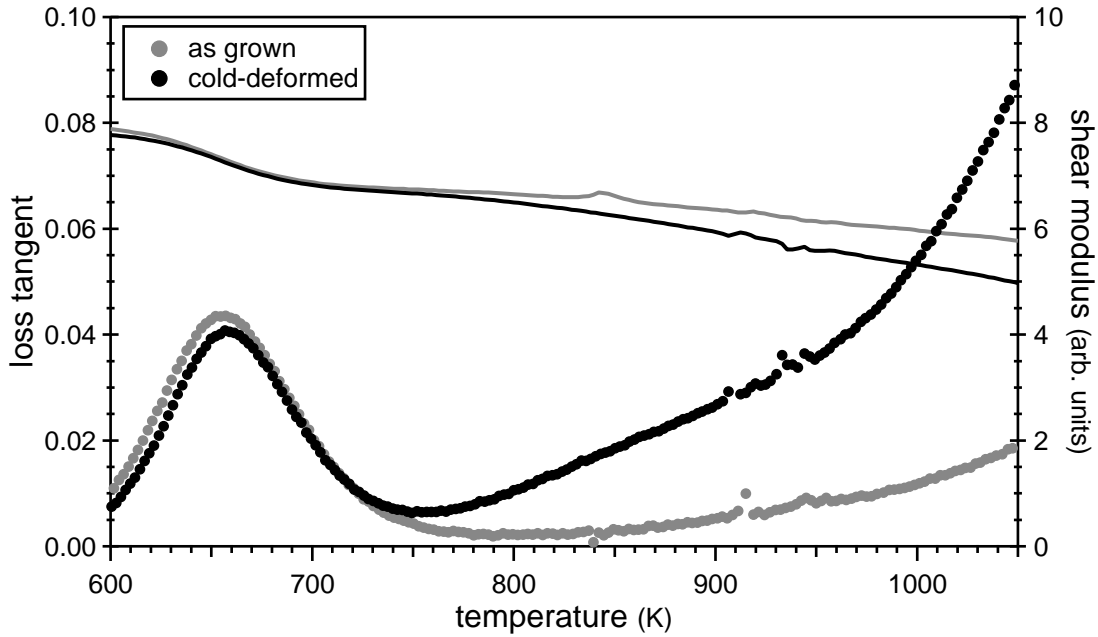


Figure 5.25: Mechanical loss spectrum of a Au 5130-1 monocrystal plastically deformed at room temperature, showing a strong increase of the high-temperature dislocation-related background compared to the undeformed monocrystal (as grown by the Bridgman method).

does. Furthermore, micro-hardness test (with a different apparatus, producing finer indentations) on a Au 5130 polycrystal showed that the alloy hardens homogeneously, regardless of the position of the indentation, whether close to the boundary or well inside the grain — see table 5.2 as well as figure 5.24 for illustration.

For the fits to the mechanical loss spectra near the grain boundary peak, presented in section 5.2, we had used Schoeck’s expression, equation (5.6), for the high-temperature background. It describes the mechanical loss created by dislocation loops vibrating around their average position under an external stress and a restoring force (due to their line tension or internal stresses), assuming their motion is subject to viscous drag created by the interaction with point defects. The background would then be nothing but the low-temperature side of a peak, the maximum of which is never reached as it is too close or even beyond the melting point. In the simplest case, where the restoring force is the same for each dislocation loop, the background mechanical loss is proportional to the dislocation density Λ (total dislocation length per volume) and has a $\frac{1}{\omega}$ frequency dependence. The more general equation (5.6) admits a distribution of restoring forces, which alters the frequency dependence to ω^{-n} with n close to 1.

All fits, those performed for frequency as well as those for temperature spectra, generally showed that equation (5.6) is a good approximation of the high-temperature/low-frequency background. For the frequency exponent n , values between 1 and 1.2 were common. The activation energy governing the viscous drag, H_{bg} from equation (5.6), was best fit with values near 0.3 eV in most cases.

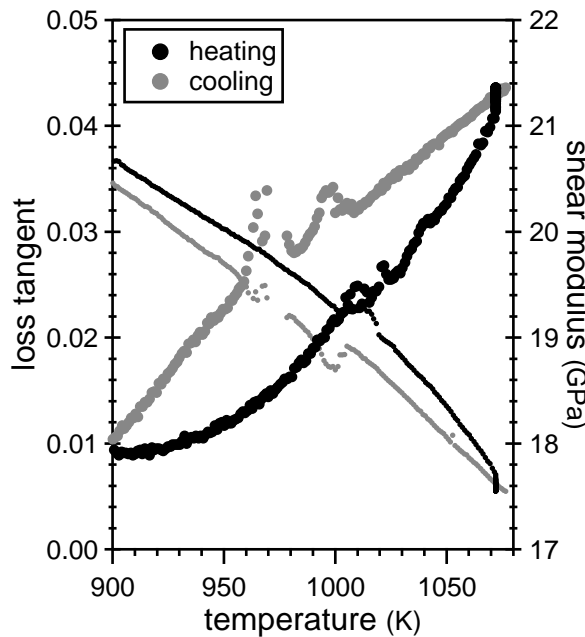


Figure 5.26: Spectrum of the Au 5130 single crystal in heating and cooling (at 0.5 MPa stress amplitude), showing a hysteretic behavior of the high-temperature dislocation-related background.

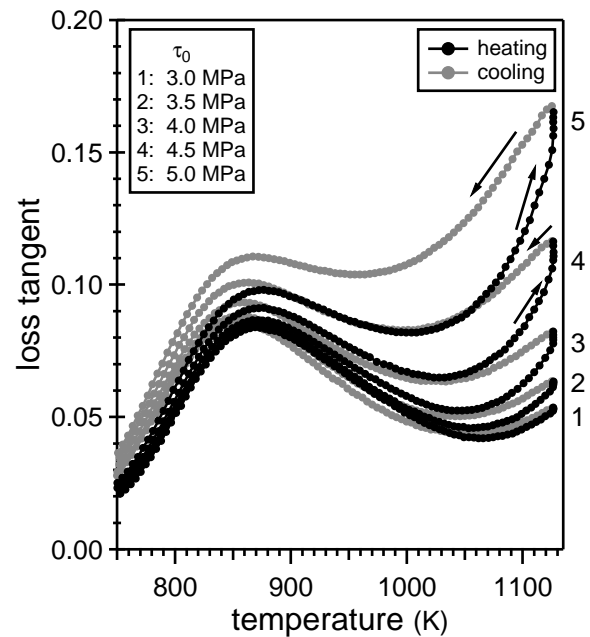


Figure 5.27: Increase of the dislocation-related background at high temperature and high shear stress amplitude in the mechanical loss temperature spectrum of Au 5125 at 0.05 Hz excitation frequency.

It is therefore reasonable to suppose that the high-temperature background observed in all 18-carat gold alloys is created by the relaxation of bulk dislocations. In an effort to substantiate this claim, a monocrystalline specimen of Au 5130-1 was plastically deformed at room temperature. Such a mechanical treatment increases the dislocation density Λ . Afterwards, the mechanical loss spectrum was measured and compared to the non-deformed crystal as grown by the Bridgman method. Both spectra are plotted on figure 5.25. Since the specimen is a single crystal, no grain boundary peak obfuscates the high-temperature background, which can be seen to have increased by a factor of 5.

The spectrum of Au 5130, presented as figure 3.16 in chapter 3 (on page 46) provides direct evidence for the interaction of precipitates and dislocations. The high-temperature region is shown once more in figure 5.26. It features a hysteresis of the background over roughly the same temperature range as the hysteresis due to the particle-blocked grain boundary peak in the polycrystal. The evolution of the background from one level to another can be attributed to precipitates pinning bulk dislocations. This would reduce the density of mobile dislocations and thus the magnitude of background damping, but not change the activation energy which defines the slope of the background contribution in the temperature spectrum. Consistently, no such hysteresis was observed in the single crystal of Au 5130-1 (see figure 3.17, page 46), which does not form a second phase.

Dislocations may even be created as a consequence of deformation by the torsion pendulum itself, during a measurement. This can be seen in figure 5.27 for Au 5125. When the stress amplitude was high enough (more than 3 MPa), dislo-

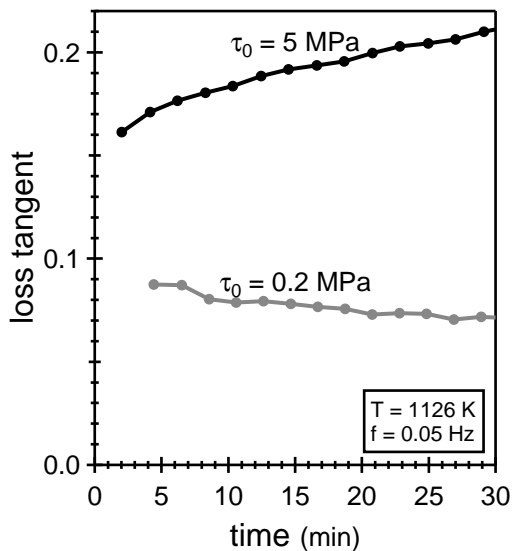


Figure 5.28: Increase and decrease of the high-temperature mechanical loss in Au 5125 over time, at high and low shear stress amplitude, respectively.

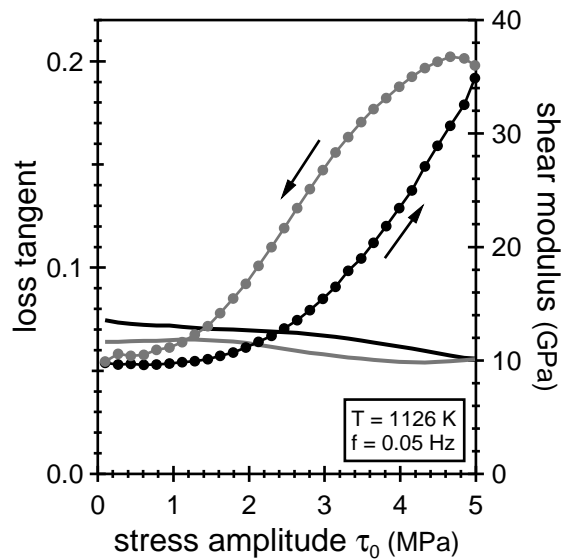


Figure 5.29: Hysteresis of the mechanical loss in Au 5125 in scans as a function of shear stress amplitude at high temperature.

cation sources would be activated at temperatures above 1100 K. This increase of the exponential background is permanent if one cools down immediately afterwards. Note that, as expected, the grain boundary peak remains unaffected by the background change — yet another indicator that this relaxation is not related to bulk dislocations.

If one stays at high temperature, but excites at a moderate or low stress level (below 2 MPa), the opposite effect occurs: the exponential background decreases with time. This general trend was already commented on in the discussion of the white golds' temperature spectra at the end of chapter 3. It can be understood as the mutual annihilation of dislocations of opposite sign during the annealing. The decline of the background damping was observed in virtually all alloys over the course of experiments. After only a few temperature sweeps to 1000 K or more, the background level was often much lower than in the beginning. Its magnitude therefore depends on the thermal history of a given sample. The increase or decline of the background over time, depending on the respective stress amplitude, can be directly observed on figure 5.28.

The combination of the two phenomena — creation and annihilation of bulk dislocations — explains the conspicuous hysteresis the mechanical loss presents during amplitude scans at high temperature. An example is presented in figure 5.29. Note, however, that not all aspects of this hysteretic behavior are fully understood, particularly the fact that it is much less pronounced when the excitation frequency is raised towards 1 Hz. Other experiments suggested a non-trivial amplitude dependence of the background also at much lower temperatures. Therefore, a thorough analysis of the background relaxation at various temperatures, amplitudes and frequencies seems warranted to affirm this interpretation with

due care.

The pinning of bulk dislocations by precipitates also explains the retardation of recrystallization in those white gold alloys that form a second phase. This was noted in section 3.2 and exemplified by figure 3.19 (page 47). Recrystallization occurs after heavy cold-deformation, producing a high dislocation density, and subsequent annealing at elevated temperatures. It begins with the motion of dislocations that arrange themselves to form low-angle subgrain boundaries, which then migrate while eliminating more defects (the driving force of the process) until a high-angle grain boundary emerges. Here, too, precipitates form obstacles to the dislocation movement. The recrystallization process speeds up considerably when the particles dissolve.

From a more general perspective, the analysis of the mechanical loss spectra as well as first results from electron spectroscopy both suggest that two types of particles form in age-hardenable white gold alloys, one rich in gallium, the other rich in indium. The comparison of the Au 5130 modifications (figure 3.14 on page 45) indicated that the indium-rich phase (in Au 5130-2) had a significantly (about 100 K) lower precipitation temperature compared to the gallium-rich phase. In alloys containing both additives, a two-step precipitation process would not be evident in mechanical spectroscopy since the grain-boundary peak's breakdown may only serve as an indicator for the phase formations that is first to occur.

Conclusions

The mechanical loss spectra of 18-carat gold alloys between room temperature and the melting point are characterized by three different anelastic relaxations: the Zener relaxation due to stress-induced directional ordering of different types of atomic bonds at temperatures between 550 K and 700 K (depending on alloy composition); the relaxation due to grain boundary sliding in the polycrystalline material at temperatures above 700 K; and the vibration of bulk dislocations that gives rise to the high-temperature background.

The Zener relaxation decreases drastically in magnitude when the alloy forms regions that exhibit long-range atomic order. This occurs in yellow Au–Cu–Ag alloys of sufficient copper content (above 20 atomic-%) below a critical temperature of 550 K and up to 620 K. The phase transformation shows the same characteristics as the $\alpha \rightarrow \text{AuCu II}$ order-disorder transition in near-stoichiometric AuCu, but develops tetragonal superstructures of the AuCu I type and is accompanied (or closely followed) by the separation of a silver-rich solid solution. Alloys with such microstructure present an increased hardness with respect to the high-temperature solid solution, as differently oriented ordered regions hinder the motion of dislocations through the bulk. The gradual breakdown of the Zener peak follows the progress of the change in microstructure and provides an estimation of the transformation time as a function of ageing temperature. No significant atomic ordering was detected in any of the white gold alloys. Their composition is not suited to allow for this phase transformation of practical convenience.

The age-hardenability of the subgroup of white gold alloys containing gallium or, when combined with copper, indium additives is attributed to second-phase particles forming inside the grains, pinning bulk dislocations. As this process coincides with the blocking of grain boundary sliding by the same precipitates, the gradual breakdown of the grain boundary peak reflects the kinetics of precipitation. However, all experimental evidence suggests that two types of particles are formed: one composed of palladium and gallium, the other of indium and copper. There is no reason to assume that both phases become stable at the same critical temperature, nor that they confer the same mechanical properties, particularly with regard to the detrimental effect of grain boundary embrittlement that, if it occurs, would be more likely caused by the Pd–Ga precipitates. One should therefore seek to optimize the microstructure by varying the type and relative

content of additives, or by exploring more elaborate heat treatments that favor a homogeneous and refined distribution of particles throughout the material.

The two phase transformations that trigger the hardening, atomic ordering in yellow gold and precipitation of a second phase in white gold, both exhibit fast kinetics that, at the optimum temperature, complete in a matter of minutes. For industrial applications, this result underlines the necessity to guarantee a reliably fast quenching process of solution-treated specimens, particularly for ingots of larger sizes, in order to bypass the phase transformation and obtain a homogeneous material of maximum ductility before proceeding with metal forming, such as cold-rolling or extrusion.

Bibliography

The electronic version of this document (a PDF file) includes hyperlinks (highlighted in the text) to electronic resources for those references available on the Internet at print time.

- [Ab₀₄] Jose P. Abriata, David E. Laughlin: *The Third Law of Thermodynamics and low temperature phase stability*, *Progress in Materials Science* 49 (3–4), p. 367 (2004)
- [AD²¹⁸] J. T. Owen (editor): *Gold Alloy Data: 18 carat, Pale Yellow*, *Gold Technology* 10, p. 6 (1993)
- [AD³¹⁸] J. T. Owen (editor): *Gold Alloy Data: Standard 750‰ Yellow Alloy*, *Gold Technology* 1, p. 10 (1990)
- [AD⁴¹⁸] J. T. Owen (editor): *Gold Alloy Data: 18 carat, Pink*, *Gold Technology* 10, p. 11 (1993)
- [AD⁵¹⁸] J. T. Owen (editor): *Gold Alloy Data: 18 carat, Red*, *Gold Technology* 10, p. 14 (1993)
- [AgAu] Bruno Predel: *Ag–Au (Silver–Gold)*, chapter 11 in ref. LB_{5a}^{IV} (1991)
- [AgCu] Bruno Predel: *Ag–Cu (Silver–Copper)*, chapter 23 in ref. LB_{5a}^{IV} (1991)
- [AM] Neil W. Ashcroft, N. David Mermin: *Solid State Physics*, ISBN 0-03-049346-3, Saunders College (1981)
- [AM¹⁵] Neil W. Ashcroft, N. David Mermin: *Band Structure of Selected Metals*, chapter 15 in ref. AM (1981)
- [Ar₆₇] V. S. Arunachalam, R. W. Cahn: *Order-hardening in CuAu*, *Journal of Materials Science* 2 (2), p. 160 (1967)
- [Ar₇₀] V. S. Arunachalam: *Comments on “The Ordering of CuAu”*, *Scripta Metallurgica* 4 (11), p. 859 (1970)
- [As₇₂] M. F. Ashby: *Boundary defects, and atomistic aspects of boundary sliding and diffusional creep*, *Surface Science* 31, p. 498 (1972)
- [AuCu] Bruno Predel: *Au–Cu (Gold–Copper)*, chapter 272 in ref. LB_{5a}^{IV} (1991)
- [AuGa] Bruno Predel: *Au–Ga (Gold–Gallium)*, chapter 277 in ref. LB_{5a}^{IV} (1991)
- [AuIn] Bruno Predel: *Au–In (Gold–Indium)*, chapter 285 in ref. LB_{5a}^{IV} (1991)
- [AuPd] Bruno Predel: *Au–Pd (Gold–Palladium)*, chapter 305 in ref. LB_{5a}^{IV} (1991)
- [Ba₀₁^a] P. Ballo, V. Slugeň: *Atomic simulation of grain-boundary sliding and migration in copper*, *Physical Review B* 65 (1), p. 012107 (2001)

- [Ba₀₁^b] L. Battezzati, M. Belotti, V. Brunella: *Calorimetry of ordering and disordering in AuCu alloys*, *Scripta Materialia* 44 (12), p. 2759 (2001)
- [Ba₀₅] P. Ballo, J. Degmová, V. Slugeň: *Grain boundary sliding and migration in copper: Vacancy effect*, *Physical Review B* 72 (6), p. 064118 (2005)
- [Be₀₄] W. Benoit: *High-temperature relaxations*, *Materials Science and Engineering A* 370 (1-2), p. 12 (2004)
- [Bo₂₈] G. Borelius, C. H. Johansson, J. O. Linde: *Die Gitterstrukturumwandlungen in metallischen Mischkristallen*, *Annalen der Physik* 391 (10), p. 291 (1928)
- [Bo₇₂] C. Bonjour, W. Benoit: *Étude par frottement intérieur de la transformation ordre-désordre dans les alliages Au-Cu*, *Helvetica Physica Acta* 45 (1), p. 23 (1972)
- [Bo₉₉] J. Bonneaux, M. Guymont: *Study of the order-disorder transition series in AuCu by in-situ temperature electron microscopy*, *Intermetallics* 7 (7), p. 797 (1999)
- [Bo₀₆] Nataliya Bochvar, Yurii Liberov: *Gold-Copper-Palladium*, chapter 20 in ref. LB₁₁^{IV} (2006)
- [Br₇₁] Franz R. Brotzen, Rex B. McLellan: *Ordering in CuAu*, *Scripta Metallurgica* 5 (3), p. 241 (1971)
- [Ca₆₃] B. Caroli: *Absorption infra-rouge dans les alliages dilués Au Ni*, *Zeitschrift für Physik B: Condensed Matter* 1 (4), p. 346 (1963)
- [Ca₉₄] B. Cao, R. Schaller, W. Benoit, F. Cosandey: *Internal friction associated with grain boundaries in Ni-Cr alloys*, *Journal of Alloys and Compounds* 211-212, p. 118 (1994)
- [Ca₉₈] Robert W. Cahn: *A precious stone that isn't*, *Nature* 396 (6711), p. 523 (1998)
- [CH] Robert W. Cahn, Peter Haasen (editors): *Physical Metallurgy*, ISBN 0-444-89875-1, North Holland (1996)
- [Ch₇₀] T. Chandra, B. Ramaswami: *Ordering in CuAu*, *Scripta Metallurgica* 4 (3), p. 175 (1970)
- [Ch₉₂] Bulbul Chakraborty, Zhigang Xi: *Atomistic Landau theory of ordering and modulated phases in Cu-Au alloys*, *Physical Review Letters* 68 (13), p. 2039 (1992)
- [Co₇₄] F. Cosandey, C. Bonjour, M. Mondino: *Étude par frottement intérieur de la transformation ordre-désordre dans les alliages Au-Cu*, *Helvetica Physica Acta* 47 (4), p. 399 (1974)
- [Co₀₁] Christopher W. Corti: *Strong 24 carat golds: The metallurgy of microalloying*, *Gold Technology* 33, p. 27 (2001)
- [Cr₉₉] Cristian Cretu, Elma van der Lingen: *Coloured Gold Alloys*, *Gold Bulletin* 32 (4), p. 115 (1999)
- [Di₅₁] G. J. Dienes: *Kinetics of Ordering in the Alloy AuCu*, *Journal of Applied*

- Physics 22 (8), p. 1020 (1951)
- [Dr₉₂] E. Drost, J. Hausselt: *Uses of Gold in Jewelry*, *Interdisciplinary Science Reviews* 17 (3), p. 271 (1992)
- [Fe₉₉] Y. Feutelais, B. Legendre, M. Guymont: *New enthalpies determination and in situ X-ray diffraction observations of order/disorder transitions in Au_{0.5}Cu_{0.5}*, *Acta Materialia* 47 (8), p. 2539 (1999)
- [Fi₀₂] Jan Fikar: *Al–Cu–Fe quasicrystalline coatings and composites studied by mechanical spectroscopy*, PhD thesis, École Polytechnique Fédérale de Lausanne (2002)
- [Fo₉₅] P. A. Fotiu, R. Heuer, F. Ziegler: *BEM analysis of grain boundary sliding in polycrystals*, *Engineering Analysis with Boundary Elements* 15 (4), p. 349 (1995)
- [Fr₅₈] J. Friedel: *Sur la structure électronique des métaux et alliages de transition et des métaux lourds*, *Journal de Physique et le Radium* 19 (6), p. 573 (1958)
- [Fr₀₀] A. I. Frenkel, V. Sh. Machavariani, A. Rubshtein, Yu. Rosenberg, A. Voronel, E. A. Stern: *Local structure of disordered Au–Cu and Au–Ag alloys*, *Physical Review B* 62 (14), p. 9364 (2000)
- [GD₀₈] World Gold Council: *Gold Demand Trends – Full year and fourth quarter 2008*, technical report (2009)
A report published quarterly by the World Gold Council, a marketing organization funded by most of the largest gold mining companies, based on data provided by GFMS Limited, a precious metals consultancy specializing in gold market research.
- [Gh₈₀] F. Ghahremani: *Effect of grain boundary sliding on anelasticity of polycrystals*, *International Journal of Solids and Structures* 16 (9), p. 825 (1980)
- [Go₉₈] G. Gottstein, L. S. Shvindlerman: *The Compensation Effect in Thermally Activated Interface Processes*, *Interface Science* 6 (4), p. 267 (1998)
- [Haa] Peter Haasen: *Physical Metallurgy*, ISBN 0-521-32489-0, Cambridge University Press (1986)
- [Hi₆₂] M. Hirabayashi, S. Weissmann: *Study of CuAu I by transmission electron microscopy*, *Acta Metallurgica* 10 (1), p. 25 (1962)
- [Iw₈₂] Y. Iwasaki, K. Fujimoto: *Intrinsic internal friction in solids measured by torsion pendulums*, *Journal of Physics D: Applied Physics* 15 (8), p. 1349 (1982)
- [Ji₀₅] W. B. Jiang, P. Cui, Q. P. Kong, Y. Shi, M. Winning: *Internal friction peak in pure Al bicrystals with <100> tilt boundaries*, *Physical Review B* 72 (17), p. 174118 (2005)
- [Ke₄₇^a] T'ing-Sui Kê: *Experimental Evidence of the Viscous Behavior of Grain Boundaries in Metals*, *Physical Review* 71 (8), p. 533 (1947)
- [Ke₄₇^b] T'ing-Sui Kê: *Stress Relaxation across Grain Boundaries in Metals*,

- Physical Review 72 (1), p. 41 (1947)
- [Ki₈₆] S. Kiss, R. Schaller, W. Benoit: *Anelastic effects due to precipitation and dissolution in AlAg alloys*, *Acta Metallurgica* 34 (11), p. 2151 (1986)
- [Ko₀₉] Q. P. Kong, W. B. Jiang, Y. Shi, P. Cui, Q. F. Fang, M. Winning: *Grain boundary internal friction in bicrystals with different misorientations*, *Materials Science and Engineering A* 521-522, p. 128 (2009)
- [Ku₅₅] G. C. Kuczynski, R. F. Hochman, M. Doyama: *Study of the Kinetics of Ordering in the Alloy AuCu*, *Journal of Applied Physics* 26 (7), p. 871 (1955)
- [Ku₅₇] Ryogo Kubo: *Statistical-Mechanical Theory of Irreversible Processes. I. General Theory and Simple Applications to Magnetic and Conduction Problems*, *Journal of the Physical Society of Japan* 12 (6), p. 570 (1957)
- [La₈₇] P. M. Laufer, D. A. Papaconstantopoulos: *Tight-binding coherent-potential-approximation study of the electronic states of palladium—noble-metal alloys*, *Physical Review B* 35 (17), p. 9019 (1987)
- [La₉₄] Angeliki Lakki: *Mechanical spectroscopy of fine-grained zirconia, alumina and silicon nitride*, PhD thesis, École Polytechnique Fédérale de Lausanne (1994)
- [La₉₈] A. Lakki, R. Schaller, C. Carry, W. Benoit: *High temperature anelastic and viscoplastic deformation of fine-grained MgO-doped Al₂O₃*, *Acta Materialia* 46 (2), p. 689 (1998)
- [LB_{5a}^{IV}] O. Madelung (editor): *Phase Equilibria, Crystallographic and Thermodynamic Data of Binary Alloys · Ac-Au — Au-Zr*, volume 5a of *Landolt-Börnstein Group IV Physical Chemistry*, ISBN 978-3-540-15516-4, Springer-Verlag (1991)
- [LB₁₁^{IV}] G. Effenberg, S. Ilyenko (editors): *Ternary Alloy Systems: Phase Diagrams, Crystallographic and Thermodynamic Data critically evaluated by MSIT · Noble Metal Systems, Selected Systems from Ag-Al-Zn to Rh-Ru-Sc*, volume 11B of *Landolt-Börnstein Group IV Physical Chemistry*, ISBN 978-3-540-25772-1, Springer-Verlag (2006)
- [Le₄₉] Josef Leuser: *Über die Besonderheiten der Edelmetallegierungen im Schmuckgewerbe*, *Metall* 3 (7/8), p. 105 (1949)
- [Le₅₄] A. D. Le Claire, W. M. Lomer: *Relaxation effects in solid solutions arising from changes in local order II: Theory of the relaxation strength*, *Acta Metallurgica* 2 (6), p. 731 (1954)
- [Li₄₉] Yin-Yuan Li: *Quasi-Chemical Method in the Statistical Theory of Regular Mixtures*, *Physical Review* 76 (7), p. 972 (1949)
- [Li₆₁] C. Y. Li, A. S. Nowick: *Magnitude of the Zener Relaxation Effect II: Temperature Dependence of the Relaxation Strength in α Ag-Zn*, *Acta Metallurgica* 9 (1), p. 49 (1961)
- [Lu₅₆] J. Lulay, G. Wert: *Internal friction in alloys of Mg and Cd*, *Acta Metallurgica* 4 (6), p. 627 (1956)

- [Ma₆₄] Arnulf Maeland, Ted B. Flanagan: *Lattice spacings of gold–palladium alloys*, *Canadian Journal of Physics* 42 (11), p. 2364 (1964)
- [Ma₆₉] S. L. Mannan, V. S. Arunachalam: *Low temperature ordering in CuAu*, *Scripta Metallurgica* 3 (8), p. 597 (1969)
- [Mc₇₈] Allen S. McDonald, George H. Sistare: *The Metallurgy of Some Carat Gold Jewellery Alloys I: Coloured Gold Alloys*, *Gold Bulletin* 11 (3), p. 66 (1978)
- [Mi₈₃] K. Miura, Manfred Wuttig, T. Yokoyama: *Nonlinear resonances in Cu₃Au*, *Scripta Metallurgica* 17 (4), p. 427 (1983)
- [Mo₆₇] M. E. de Morton, G. M. Leak: *Zener Relaxations in the Copper–Gold System*, *Metal Science Journal* 1, p. 182 (1967)
- [Mo₈₃] T. Mori, M. Koda, R. Monzen, T. Mura: *Particle blocking in grain boundary sliding and associated internal friction*, *Acta Metallurgica* 31 (2), p. 275 (1983)
- [Mo₉₃] R. Monzen, M. Futakuchi, K. Kitagawa, T. Mori: *Measurement of grain boundary sliding of [011] twist boundaries in copper by electron microscopy*, *Acta Metallurgica et Materialia* 41 (6), p. 1643 (1993)
- [Mo₉₆] C. Molteni, G. P. Francis, M. C. Payne, V. Heine: *First Principles Simulation of Grain Boundary Sliding*, *Physical Review Letters* 76 (8), p. 1284 (1996)
- [Mo₉₇] C. Molteni, Nicola Marzari, M. C. Payne, V. Heine: *Sliding Mechanisms in Aluminum Grain Boundaries*, *Physical Review Letters* 79 (5), p. 869 (1997)
- [Moh] Peter Mohn: *Magnetism in the Solid State*, ISBN 978-3-540-30981-9, Springer Berlin Heidelberg (2006)
- [Na₈₈] Masaharu Nakagawa, Katsuhiko Yasuda: *A coherent phase diagram of the Au_x(Ag_{0.24}Cu_{0.76})_{1-x} section of the Au–Cu–Ag ternary system*, *Journal of the Less-Common Metals* 138 (1), p. 95 (1988)
- [Na₉₈] Tschang-Uh Nahm, Ranju Jung, Jae-Young Kim et al.: *Electronic structure of disordered Au-Pd alloys studied by electron spectroscopies*, *Physical Review B* 58 (15), p. 9817 (1998)
- [NB] A. S. Nowick, B. S. Berry: *Anelastic Relaxation in Crystalline Solids*, ISBN 0-12-522650-0, Academic Press (1972)
- [NB³] A. S. Nowick, B. S. Berry: *Mechanical Models and Discrete Spectra*, chapter 3 in ref. NB (1972)
- [NB⁸] A. S. Nowick, B. S. Berry: *Theory of Point-Defect Relaxations*, chapter 8 in ref. NB (1972)
- [NB¹⁰] A. S. Nowick, B. S. Berry: *The Zener Relaxation*, chapter 10 in ref. NB (1972)
- [NB¹⁵] A. S. Nowick, B. S. Berry: *Boundary Relaxation Processes and Internal Friction at High Temperatures*, chapter 15 in ref. NB (1972)

- [Ng79] K. L. Ngai, A. K. Jonscher, C. T. White: *On the origin of the universal dielectric response in condensed matter*, *Nature* 277, p. 185 (1979)
- [No52] A. S. Nowick: *Anelastic Measurements of Atomic Mobility in Substitutional Solid Solutions*, *Physical Review* 88 (4), p. 925 (1952)
- [No63] A. S. Nowick, W. R. Heller: *Anelasticity and stress-induced ordering of point defects in crystals*, *Advances in Physics* 12 (47), p. 251 (1963)
- [No92] Greg Normandeau: *White Golds: A Review of Commercial Material Characteristics & Alloy Design Alternatives*, *Gold Bulletin* 25 (3), p. 94 (1992)
- [No94] Greg Normandeau, Rob Roeterink: *White Golds: A Question of Compromises*, *Gold Bulletin* 27 (3), p. 70 (1994)
- [OB59] J. L. O'Brien, G. C. Kuczynski: *X-ray study of the kinetics of ordering in AuCu*, *Acta Metallurgica* 7 (12), p. 803 (1959)
- [OC78] Grahame P. O'Connor: *Improvement of 18 Carat White Gold Alloys*, *Gold Bulletin* 11 (2), p. 35 (1978)
- [Oh98] M. Ohta, T. Shiraishi, R. Ouchida, M. Nakagawa, S. Matsuya: *Shape restoration effect associated with order-disorder transformation in equiatomic AuCu and AuCu-Ga alloys*, *Journal of Alloys and Compounds* 265 (1-2), p. 240 (1998)
- [Ok83] H. Okamoto, T. Massalski: *The Ag-Au (Silver-Gold) system*, *Journal of Phase Equilibria* 4 (1), p. 30 (1983)
- [Oz98] V. Ozoliņš, C. Wolverton, Alex Zunger: *Cu-Au, Ag-Au, Cu-Ag, and Ni-Au intermetallics: First-principles study of temperature-composition phase diagrams and structures*, *Physical Review B* 57 (11), p. 6427 (1998)
- [Pe64] D. T. Peters, J. C. Bisseliches, J. W. Spretnak: *Some Observations of Grain Boundary Relaxation in Copper and Copper-2% Cobalt*, *Transactions of The Metallurgical Society of AIME* 230, p. 530 (1964)
- [Po83] F. Povolo, A. F. Armas: *Zener Relaxation in Copper-Gold Alloys*, *Acta Metallurgica* 31 (4), p. 643 (1983)
- [Po84] F. Povolo, A. F. Armas: *Anisotropy of the Zener relaxation in Cu₃Au*, *Philosophical Magazine A* 49 (6), p. 865 (1984)
- [Po94] F. Povolo, H. O. Mosca: *Zener Relaxation Strength in bcc and fcc alloys Under Torsional and Longitudinal Excitations*, *Acta Metallurgica et Materialia* 42 (1), p. 109 (1994)
- [Pr06] Alan Prince: *Silver-Gold-Copper*, chapter 2 in ref. LB₁₁^{IV} (2006)
- [Q⁻¹] R. Schaller, G. Fantozzi, G. Gremaud (editors): *Mechanical Spectroscopy Q⁻¹ 2001*, ISBN 0-87849-876-1, Trans Tech Publications, Switzerland (2001)
- [Q_{3,4}⁻¹] M. L. No: *Dislocation damping at medium temperature*, chapter 3.4 in ref. Q⁻¹ (2001)
- [Q_{3,5}⁻¹] A. Rivière: *High temperature damping*, chapter 3.5 in ref. Q⁻¹ (2001)

- [Q_{4.1}⁻¹] W. Benoit: *Grain Boundary: description and dynamics*, chapter 4.1 in ref. Q⁻¹ (2001)
- [Q_{4.2}⁻¹] W. Benoit: *Grain Boundary relaxation in metals*, chapter 4.2 in ref. Q⁻¹ (2001)
- [Q_{4.3}⁻¹] R. Schaller, A. Lakki: *Grain boundary relaxations in ceramics*, chapter 4.3 in ref. Q⁻¹ (2001)
- [Q_{5.1}⁻¹] W. Benoit: *Thermodynamics of 2nd and 1st order phase transformations*, chapter 5.1 in ref. Q⁻¹ (2001)
- [Q_{5.5}⁻¹] R. Schaller: *Precipitation*, chapter 5.5 in ref. Q⁻¹ (2001)
- [Qi₀₇] Yue Qi, Paul E. Krajewski: *Molecular dynamics simulations of grain boundary sliding: The effect of stress and boundary misorientation*, *Acta Materialia* 55 (5), p. 1555 (2007)
- [Ra₇₀] B. Ramaswami: *Reply to Comments on "Ordering in CuAu"*, *Scripta Metallurgica* 4 (11), p. 865 (1970)
- [Ra₇₁] R. Raj, M. Ashby: *On Grain Boundary Sliding and Diffusional Creep*, *Metallurgical and Materials Transactions B* 2 (4), p. 1113 (1971)
- [Ra₇₇] B. D. Razuvayeva, L. A. Gutov, V. I. Syutkina, O. D. Shashkov: *Influence of phase transformations on the mechanical properties of gold-copper-silver alloys*, *The Physics of Metals and Metallography* 44, p. 135 (1977)
- [Ra₉₀] William S. Rapson: *The Metallurgy of the Coloured Carat Gold Alloys*, *Gold Bulletin* 23 (4), p. 125 (1990)
- [Rek] V. Rékatch: *Problèmes de la théorie de l'élasticité*, Mir, Moscow (1980)
- [Ri₈₁] A. Rivière, J. P. Amirault, J. Woïrgard: *High temperature internal friction and dislocation motion in poly and single crystals of f.c.c. metals*, *Journal de Physique: Colloques* 42 (C5), p. 439 (1981)
- [Ro₇₈] Errol F. I. Roberts, Keith M. Clarke: *The Colour Characteristics of Gold Alloys*, *Gold Bulletin* 12 (1), p. 9 (1978)
- [Ro₉₉] Peter Rotheram: *White Golds — Meeting the Demands of International Legislation*, *Gold Technology* 27, p. 34 (1999)
- [Ro₀₈] R. Roberti, G. Cornacchia, M. Faccoli, M. Gelfi: *On the strengthening mechanisms of 18 carat yellow gold and its mechanical behaviour*, *Materials Science & Engineering A* 488 (1-2), p. 50 (2008)
- [Ru₀₀] Roy Rushforth: *Don't let nickel get under your skin — the European experience!*, *Gold Technology* 28, p. 2 (2000)
- [Sa₇₇] K. E. Saeger, J. Rodies: *The Colour of Gold and its Alloys*, *Gold Bulletin* 10 (1), p. 10 (1977)
- [Sc₆₄] G. Schoeck, E. Bisogni, J. Shyne: *The activation energy of high temperature internal friction*, *Acta Metallurgica* 12 (12), p. 1466 (1964)
- [Sh₀₅] Y. Shi, P. Cui, Q. P. Kong, W. B. Jiang, M. Winning: *Internal friction peak in bicrystals with different misorientations*, *Physical Review B* 71 (6),

- p. 060101 (2005)
- [Sh₀₆] Y. Shi, W. B. Jiang, Q. P. Kong, P. Cui, Q. F. Fang, M. Winning: *Basic mechanism of grain-boundary internal friction revealed by a coupling model*, *Physical Review B* 73 (17), p. 174101 (2006)
- [Si₄₀] Sidney Siegel: *On the Kinetics of the Order-Disorder Transformation in Cu₃Au*, *The Journal of Chemical Physics* 8 (11), p. 860 (1940)
- [Si₉₃] V. Šíma: *Specific heat study of the critical behavior of the CuAu alloy*, *Journal de Chimie Physique* 90, p. 451 (1993)
- [Si₀₂] Vladimír Šíma: *Two models of solid-solid transformation kinetics in the CuAu intermetallic compound*, *Materials Science and Engineering A* 324 (1-2), p. 62 (2002)
- [So₆₇] Paul Soven: *Coherent-Potential Model of Substitutional Disordered Alloys*, *Physical Review* 156 (3), p. 809 (1967)
- [Su₈₀] Christian P. Susz, Michel H. Linker: *18 Carat White Gold Jewellery Alloys*, *Gold Bulletin* 13 (1), p. 15 (1980)
- [Sy₆₇] V. I. Syutkina, E. S. Yakovleva: *The Mechanism of Deformation of the Ordered CuAu Alloy*, *physica status solidi (b)* 21 (2), p. 465 (1967)
- [Ta₇₀] D. Tabor: *The hardness of solids*, *Review of Physics in Technology* 1 (3), p. 145 (1970)
- [Tim] S. P. Timoshenko, J. N. Goodier: *Theory of Elasticity*, ISBN 0-07-064720-8, McGraw-Hill (1970)
- [Tk₀₉] Iva Tkalčec, private communication (2009)
- [Tr₀₄] Lucien F. Trueb: *Gold in Watchmaking*, *Gold Bulletin* 33 (1), p. 11 (2004)
- [Tu₆₀] T. J. Turner, G. P. Williams, jr.: *Stress induced ordering in gold-silver alloys*, *Acta Metallurgica* 8 (12), p. 891 (1960)
- [We₆₇] David O. Welch, A. D. Le Claire: *Theory of Mechanical Relaxation due to Changes in Short-range Order in Alloys produced by Stress (Zener Relaxation)*, *Philosophical Magazine* 16 (143), p. 981 (1967)
- [Wi₉₆] H. Wipf, B. Kappesser: *A lattice gas model for the Zener relaxation*, *Journal of Physics: Condensed Matter* 8 (39), p. 7233 (1996)
- [Wo₈₁] J. Woircard, A. Rivière, J. De Fouquet: *Experimental and Theoretical Aspect of the High Temperature Damping of Pure Metals*, *Journal de Physique: Colloques* 42 (C5), p. 407 (1981)
- [Ze₄₁] Clarence Zener: *Theory of the Elasticity of Polycrystals with Viscous Grain Boundaries*, *Physical Review* 60 (12), p. 906 (1941)
- [Ze₄₇] Clarence Zener: *Stress Induced Preferential Orientation of Pairs of Solute Atoms in Metallic Solid Solution*, *Physical Review* 71 (1), p. 34 (1947)
- [Zen] Clarence Zener: *Elasticity and Anelasticity of Metals*, The University of Chicago Press (1948)

Acknowledgements

When I started this work, a little more than four years ago, I did not have the first clue about mechanical spectroscopy, nor did I know much about gold alloys. What sparked my interest was the prospect of studying phase transformations — certainly a somewhat Pavlovian response for a solid-state physicist. In retrospect, I am grateful and happy to see that the eventual outcome is that close to the mark, and I am indebted to many people who have helped in this endeavor.

My thesis director, Robert Schaller, not only proposed the project but also guided me through it every step of the way. He often knew what my data meant before I did. I remember in particular the day I showed him the very first isothermal spectra I measured. There was this peak that would not just shift, as these peaks are wont to do, but suddenly disappear, and I couldn't help but wonder if I made some rookie mistake while operating the pendulum. Even though these results were all new, it took him less than a second to pinpoint atomic ordering as the actual culprit. Thanks to his intuitive understanding of the physics of materials, I never ran dry on ideas on what to explore next.

I am equally grateful to my other supervisor, Daniele Mari. I have profited on many occasions from his open-door policy in order to engage him in ad hoc discussions. Thanks to his broad knowledge of the field, of which he seems to know every nook and cranny, they have always turned out to be fruitful and helped me isolate the most viable ways in which to pursue my research.

I would like to extend my gratitude to Alain Munier, CEO of Varinor, for his continued support of our research collaboration, not just financially and by specimen supply, but also in terms of motivation. Over the course of four years, progress may, at times, appear to be painfully slow, but he was always quick to recall the entire way we had already come. Within this collaboration, I have also worked with and learned a lot from the following people: Nastaca Molnar, Iva Tkalčec, and Emiliano Campitelli.

Little of my experimental equipment would exist if it wasn't for the wizard behind the curtain, Bernard Guisolan. Other technicians as well have provided their expertise in doing things I can't: Guillaume Camarda, Gérald Beney, Antonio Gentile. Looking back, I appreciate the many interesting discussions I have had and the scientific input I have received from colleagues inside and outside the institute. In addition to the aforementioned, these include: Ronan Martin, Fahim Chowdhury, Alessandro Sellerio, Kyumin Lee, Duncan Alexander, Kurt Schenk, and Willy Benoit.

John Hennig, February 2010

Curriculum vitae

John Hennig, born on the 25th of October 1976 in Berlin, Germany

Education

- 1996: high school graduation from Heinrich-Hertz-Gymnasium, Berlin
- 1998–2000: Vor-Diplom in physics from Humboldt-Universität Berlin
- 2000/2001: exchange student at Université Claude Bernard in Lyon, France
- 2001–2005: Diplom (master's degree) in physics from HU Berlin

Publications

- John Hennig, Daniele Mari, Robert Schaller
Order-Disorder Phase Transition and Stress-induced Diffusion in Au-Cu
Physical Review B 79 (14), p. 144116 (2009)
- John Hennig, Daniele Mari, Robert Schaller
Stress-induced and Atomic Ordering in 18-carat Au-Cu-Ag alloys
Materials Science & Engineering A 521-522, p. 47–51 (2009)
- Iva Tkalcec, John Hennig, Daniele Mari, Robert Schaller
Mechanical spectroscopy of 18-carat AuCuPd white gold alloys
Materials Science & Engineering A 521-522, p. 52–54 (2009)
- John Hennig, Iva Tkalcec, Daniele Mari, Robert Schaller
Grain Boundary Relaxation in 18-carat Gold Alloys
To be published (2010)

Teaching assignments

- Assistant in lab course “Introduction à la métrologie” for physics students (winter 2005/2006, winter 2006/2007, fall 2007)
- Assistant in lab course “Travaux pratiques de physique générale” for life science students (summer 2006, summer 2007, spring 2008)
- Assistant for exercise session of “Physique générale” for students of forensic science (fall 2008, spring 2009, fall 2009)